Characterization of a Robot Designed for Hand Rehabilitation

by

Philip H. Tang

B.S.M.E., Northwestern University (2000)

Submitted to the Department of Mechanical Engineering
in partial fulfillment of the requirements for the degree of

Master of Science

at the

MASSACHUSETTS INSTITUTE OF TECHNOLOGY

September 2002

Author . ...
Department of Mechanical Engineering
August 12, 2002

Certified by ....
Neville Hogan
Professor
Thesis Supervisor

Accepted by ....
Ain A. Sonin
Chairman, Department Committee on Graduate Students

Characterization of a Robot Designed for Hand Rehabilitation

by

Philip H. Tang

Submitted to the Department of Mechanical Engineering
on August 12, 2002, in partial fulfillment of the
requirements for the degree of
Master of Science

Abstract

Studies have shown that an interactive robot can be an effective tool in stroke recovery, but only for the joints directly involved in therapy. A robot has recently been designed and prototyped through the Newman Laboratory for Biomechanics and Human Rehabilitation for the purpose of hand and finger rehabilitation. This thesis discusses some flaws in the original design and the characterization of the functional hardware. The investigation examined the static and dynamic response of the important electrical and mechanical components, including the effect of friction in the cable-drive transmission. A simple model is developed from experimental data and used for friction compensation in several controllers. Open-loop control and closed-loop PD control laws are implemented and the results are examined. Suggestions are then presented for use in the next iteration of the robot design.

Thesis Supervisor: Neville Hogan
Title: Professor

Acknowledgments

The work presented in this thesis could not have been possible without the contribution of many people. First, I would like to acknowledge my advisor, Neville Hogan. His extensive knowledge and keen intuition of engineering combined with his curiosity and desire for understanding have pushed me to work beyond my expectations and have made me realize that there are always more layers to the proverbial onion. I am grateful for the opportunity to work with such a skilled and passionate individual.

I would also like to thank the members of the lab, who have all contributed to my work and my well being. Special thanks go to the veteran members — Steve Buerger, Jerry Palazzolo, and Brandon Rohrer. Their experience, advice, and insight have been indispensable. It has really been a joy for me to learn from them and to call them my co-workers and friends. As a fellow Masters student, James Celestino has been with me through all the growing pains of an MIT grad student. It has been a difficult journey, but the burden has been lighter with him around to share it. And I have no doubt that the baseball and apple-ball breaks that broke up our long, tedious days saved my sanity. Igo Krebs has provided support all along the way with his suggestions and advice. I especially appreciate the efforts he made in helping me get my motors functional. I also would like to thank Belle Kuo, Sue Fasoli, and Laura Dipietro for providing more color to the the lab and making it more hospitable. Thanks go out as well to the former members of the lab whom I had the pleasure of working with - Dustin Williams for helping me get acclimated to the lab and Kris Jugenheimer for designing the robot. Although not a member of the lab, I would like to acknowledge Fred Cote from the Edgerton Student Shop. His knowledge and expertise in machining and manufacturing helped me immensely in this project.

The support staff of the lab and the department have made my life so much easier by taking care of all the little things. Lori Humphrey helped me with all the administrative ins and outs of MIT with her good ol' southern hospitality. With no prior experience with the school, Tatiana Koleva jumped right in and filled the needs of the lab immediately. Leslie Regan and her staff have also made life in the department a smoother ride with their efficient paperwork and quick replies to all my questions. And in the short time she's been here, Ilea Mathis has excelled at breaking up the monotony of the day with her bright personality.

I would also like to thank my girlfriend, Charlene. She has been an abundant well of strength, courage, wisdom, hope, and encouragement for the past year and a half. Her empathy and compassion kept me going during times when I've been unmotivated. And her cheerfulness and good nature let me enjoy the happier moments even more. She is a loving and patient companion and is a blessing to me in so many ways.

Finally, I would like to thank my family for what they have done for me throughout my life. My brother, Stephen, has always inspired me to be a good student and a kind-hearted individual. He has been everything that an older brother should be and has been with me through all the struggles of my life. My parents, John and Debbie, have sacrificed so much to give me the opportunities to succeed. They are the biggest influence on who I am today. I know of no better example of honest, hard-working people. They came to this country and fulfilled the American dream and I am a better person because of it. This thesis is dedicated to them, for the love and support they gave and continue to give to me.

Contents

List of Figures

List of Tables

Chapter 1

Introduction

The work presented here is a product of the Newman Laboratory for Biomechanics and Human Rehabilitation at the Massachusetts Institute of Technology. Part of its ongoing research focuses on developing interactive robots as tools for physical rehabilitation. The design of these robots pays particular attention to the needs of stroke victims, as they represent a significant population of patients with physical disability.

1.1 Stroke

A stroke occurs when blood flow to an area of the brain is interrupted, usually a result of a blood clot or the rupturing of a blood vessel. The lack of blood kills brain cells in the immediate area and, if severe enough, can prove fatal.

Stroke is a significant health danger, affecting approximately 750,000 people annually in this country alone [18]. For those who survive a stroke, a common damaging side effect they face is impaired motor control in their limbs, often just on one side of the body. There are currently 4.6 million Americans living with the effects of stroke [3], two-thirds of whom are moderately or severely impaired [18]. With projections showing an almost 80% increase in the elderly (65+) population [26] and because the risk of stroke increases with age, the population of stroke victims is likely to increase.

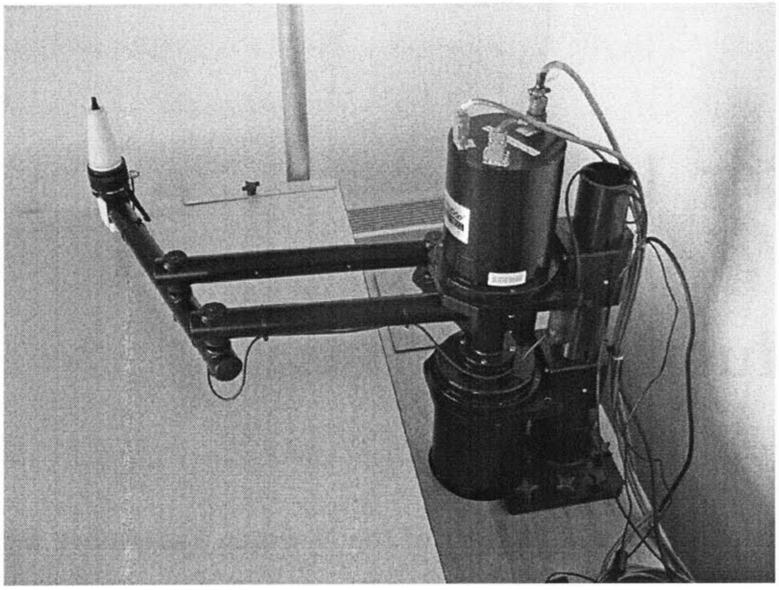

Figure 1-1: A newer prototype of the MIT MANUS therapy robot.

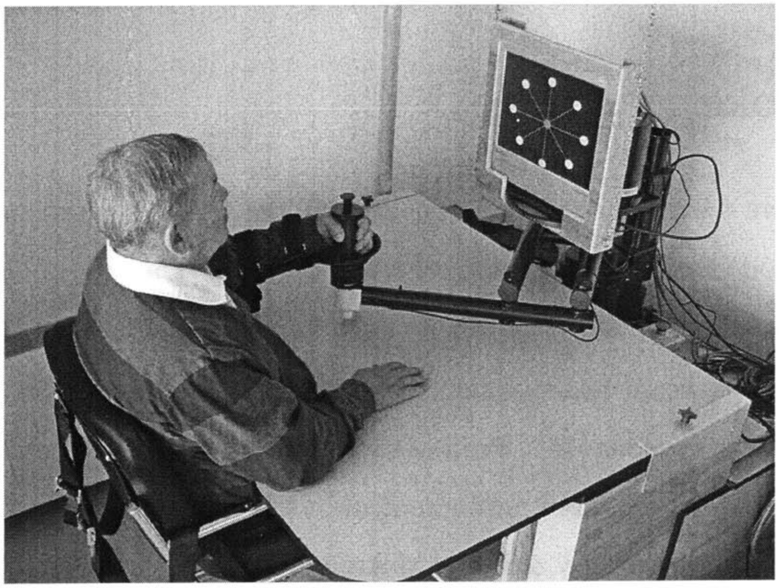

Figure 1-2: A stroke patient working with MANUS in a therapy session.

1.2 Motivation

Conventional rehabilitation for stroke patients involves physical and occupational therapy programs, which require labor-intensive, individualized exercises with a therapist. Not only does the therapist have to move the patient's affected limb repeatedly, but he/she has to gauge the level of impairment, which introduces subjectivity and imprecision. In contrast, an interactive robot can be used to make programmable and highly repeatable movements while serving as a precise measuring instrument. MIT-MANUS, a two degree-of-freedom, planar robot, is one such device (see Figures 1-1 and 1-2).

Recent research with MANUS in clinical studies suggests that robot-aided rehabilitation can reduce impairment [17], even at a better rate than conventional therapy [1]. However, improvement is only seen in limbs directly involved in the robot therapy. MANUS exercises the elbow and shoulder of the patient, but improvement in those joints will not generalize, say, to the wrist or hand [2, 27]. Given this evidence along with the success of MANUS for upper limb therapy, the next step was to design different robots to train other critical joints of the body.

With 27 separate bones and 15 joints, the hand is arguably one of the most important parts of the human body. Its versatility allows us to grasp and hold a variety of objects in a variety of ways. It is the main tool with which we interact with the physical world. The neurological impairment after a stroke can often leave a victim without the ability to grasp or hold objects. An effective rehabilitation device that can restore functional use of an impaired hand can dramatically increase a stroke victim's quality of life.

An initial design for a hand rehabilitation robot was proposed and prototyped. It will be referred to interchangeably as the hand robot or finger robot for the remainder of this thesis. In order to determine the effectiveness of the design, a thorough understanding and analysis of its features was necessary.

1.3 Outline of remaining chapters

The remaining chapters will describe the work done to extract insightful information about the design features of the hand robot.

- Chapter 2 provides a review of the design requirements and features of the robot.
- Chapter 3 presents the mechanical problems and design flaws discovered in the first prototype after manufacture and the temporary solutions used to get the hardware working.
- Chapter 4 discusses the characterization and identification of the electrical components in the system.
- Chapter 5 investigates the behavior of key components of the mechanical transmission, most notably friction in the transmission. A model is then developed to describe these components.
- Chapter 6 compares the model to actual experiments using several controllers. The effect of these controllers is also examined.
- Chapter 7 offers conclusions about the system and gives recommendations for the next iteration in the design of this robot.

Chapter 2

Robot Design

This chapter is devoted to the initial design of the finger robot. It is intended to give the reader only a basic understanding of the requirements presented in the design problem and the features incorporated into the chosen design. A more detailed explanation of the design and design process can be found elsewhere [16].

2.1 Requirements

In the design of any new machine, the functional requirements become the driving force behind the design process. All decisions made are motivated by how well each option fulfills the design requirements. The design for the hand robot was no exception. The key requirements for the robot are described below.

2.1.1 Degrees of freedom

The complexity of the hand adds increased difficulty to the design problem. With four degrees of freedom in each digit, a total of 20 exist in a normal human hand. Since this was just the first iteration of a robot suited for the purpose of hand rehabilitation, a simpler system was sufficient and not all 20 degrees of freedom required actuation.

Since the thumb plays a role in almost all functional tasks of the hand, the robot was to allow actuation of all four degrees of freedom in the thumb. For the fingers,

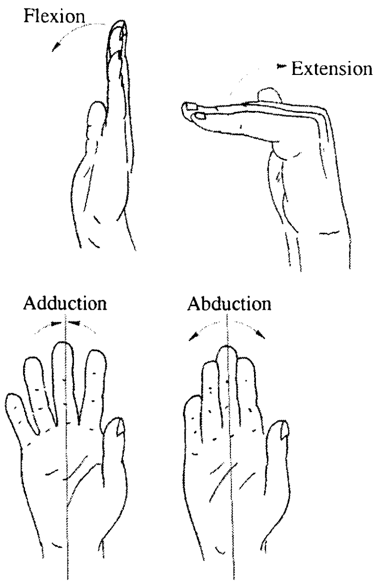

Figure 2-1: Motions of the MCP joint. [19]

however, it was deemed that abduction-adduction was a less important motion. So, the robot needed only to actuate for flexion-extension movement.

Furthermore, since it is impossible to bend the distal interphalangeal (DIP) joints independent of the proximal interphalangeal (PIP) joints, the robot needed only to actuate flexion-extension for the PIP and metacarpophalangeal (MCP) joints.

Since the purpose of the robot was to restore only basic functionality to the hand, delicate grasping with the middle, ring, and little fingers was eliminated as a design requirement. The capability of mass grasping, however, was still necessary.

2.1.2 Low impedance

The advantage of standard industrial robots is that they offer precise and highly repeatable position tracking. This makes them particularly useful for applications such as assembly line production, where the ability to move large loads in quick, defined movements is necessary. A large body of literature and research is devoted to the control of these systems to make them faster and more precise. The drawback, however, is that this gives the robot a very "hard" feel, with almost no compliance.

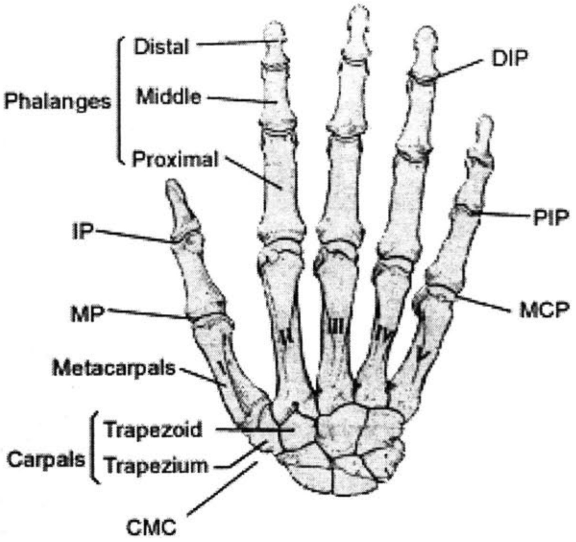

Figure 2-2: Key bones and joints of the human hand (Adapted from Anderson [4]).

Presented with any obstruction, the robot will simply apply more effort to push it out of the way and follow its desired trajectory. This results in one of two options: either the robot breaks or the object breaks. In the field of interactive robotics, the latter is not acceptable since the object is a human patient (not to say that the former is much better). Clearly, a different approach is warranted. One such approach is impedance control [14].

In impedance control with interactive robots, the human is part of the environment and is viewed as an admittance — that is, a physical system that yields a flow (velocity) for a given effort (force). The robot is then viewed as an impedance, yielding an effort for a given flow. With the ability to change the physical characteristics of the robot through software, the impedance of the robot can be specified. The human feels this as varying degrees of stiffness and damping.

The "hard" feel of standard industrial robots, then, corresponds to an extremely high impedance. Many therapeutic devices in the market today are actually high impedance systems as well. Continuous passive motion devices, such as those shown in Figure 2-3, are designed to move joints without the patient's muscles being used. They are often used after joint surgery to aid the patient's recovery. Typically these

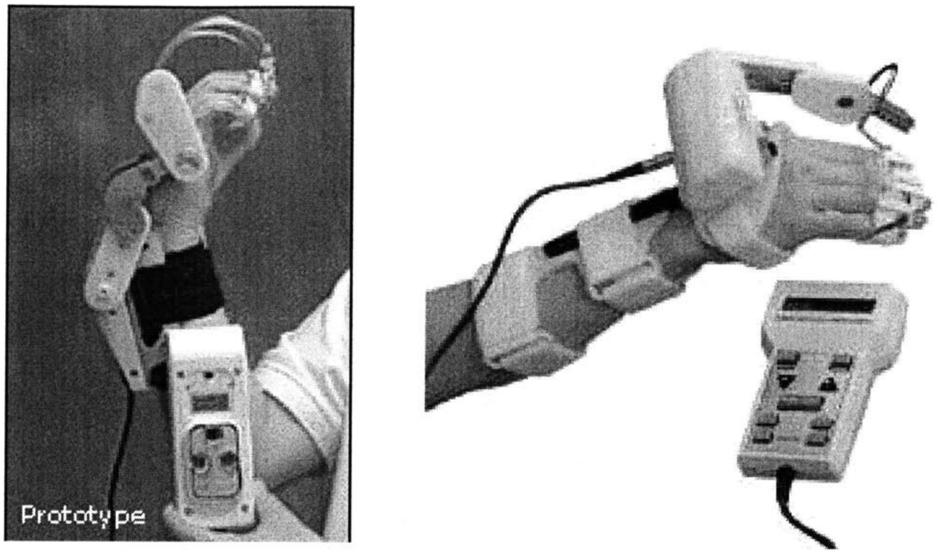

Figure 2-3: Continuous passive motion devices for the hand, made by Kinex Medical Company (left) and Thera Tech Equipment (right).

devices are geared up heavily and as a result are non-back-driveable.

A device such as MANUS, however, is a low impedance, direct-drive system. It can be programmed such that, when a patient opposes the desired trajectory, the robot will yield to that motion and generate only a spring-like resistance, programmable to varying degrees of stiffness. The stroke patient then becomes an active participant and starts down the path to recovery, the theory being that active use of the impaired muscles will help the brain reconstruct the affected neural pathways.

Like MANUS, the finger robot needed to be capable of acting as a low impedance to allow the patient more control in the power flow of the interaction.

2.1.3 Other requirements

Compatibility

Because fingers vary in size between individuals, the design needed to be compatible with different hands. If the joints of the robot were designed for some fixed finger length, a differently shaped hand could constrain the system kinematically. This in turn would subject the robot and the patient to undesirable, and most likely unsafe, loads.

Handedness

The specific impairments caused by a stroke are dependent on which area of the brain the stroke occurs. Motor control of one side of the body takes place in the opposite hemisphere of the brain. There is no tendency for a stroke to attack a particular hemisphere of the brain, so there is about an equal number of stroke patients with impairment in the left side of their body as there are those with impairment in their right. A robot designed for both hands, then, would be ideal.

2.2 Features

Using these key requirements as a guide, the first design of the robot was completed. To make it simpler, the robot was designed for only the left hand. Once it is determined that this design is feasible and effective, a mirror image of the design can be manufactured and used as a robot for the right hand. The following section describes the rest of the other important features included in the design.

2.2.1 Degrees of freedom

To allow for mass grasping with the outer three fingers but without the complexity of delicate grasping, the robot was designed to bind the middle, ring, and little fingers of the patient together in full adduction. The MCP joints of all three fingers then moved together, reducing three degrees of freedom to one. The same is true for the PIP joints.

The robot was also designed to actuate the index finger MCP and PIP joints as well as all four degrees of freedom of the thumb, giving the robot eight total degrees of freedom.

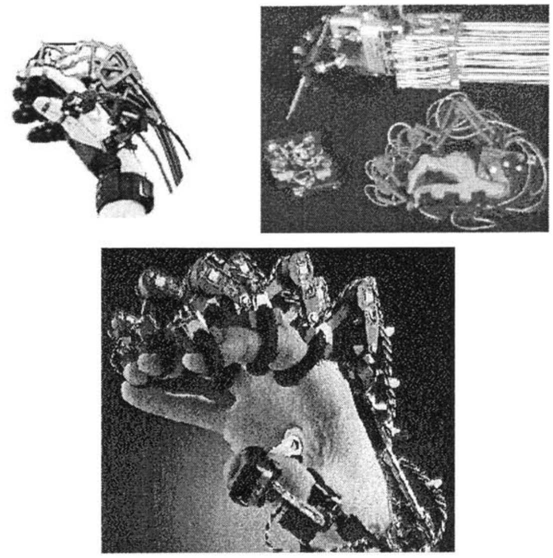

Figure 2-4: The Cybergrasp by Immersion (left), Utah Dextrous Hand Master (right), and Exos Dextrous Hand Master (bottom).

2.2.2 Co-axial joints

For the outer fingers and index finger, the joints of the robot were located on the same axis as the MCP and PIP joints and spatially located on the outer side of the patient's hand (the little finger side). To connect to the patient, small arches were designed to reach over from the joints and strap to the fingers.

Many systems have been designed to provide joint sensing of and force feedback to the fingers. The applications for these devices mostly involve virtual reality haptic feedback for teleoperation. The Cybergrasp by Immersion, the Utah Dextrous Hand Master, and the EXOS Dextrous Hand Master are all haptic feedback tools which employ an exoskeleton design, where the joints are located above the fingers, as shown in Figure 2-4. The Phantom, another popular haptic feedback tool, has a linkage system that connects to the tip of the finger (see Figure 2-5).

One feature that makes this robot different from all other devices intended to interface with the hand is the co-axial joint location.

Figure 2-5: The Phantom haptic device

2.2.3 Cable drive

All machines must employ some form of power transmission. Since the power source is always located some distance away from the endpoint of interaction, there must be some method of transmitting the power to that point. This robot was designed with a cable-drive transmission for its ability to be routed through and around obstacles. Because cables can only support load in one direction (tension), two cables were routed to each joint, allowing actuation in both directions for any given degree of freedom.

Unlike normal cable drives which support the cables through a system of pulleys, the cable supports in this transmission were designed as a series of holes through plates and blocks.

2.2.4 Flexural joints

The joints of the robot were designed as flexures. The kinematic flexibility provided would allow the joints to bend through a range of locations. This would allow patients with various different finger sizes to use the robot without any hardware adjustments.

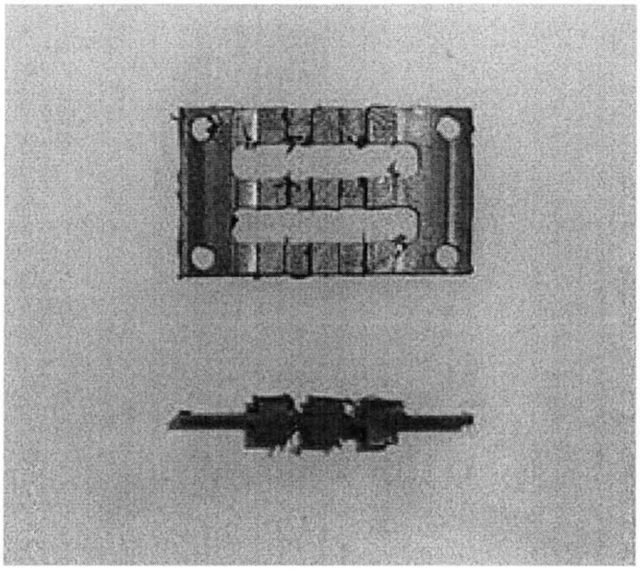

Figure 2-6: Top and side views of the flexural joints used for the finger robot.

The flexures were designed in a beaded pattern to increase torsional stiffness. Slots were inserted as well to allow the cables to cross through. The slots were not utilized in the prototype, however, because of the increased friction caused by the cables exiting the holes at sharp angles. A picture of the flexures is shown in Figure 2-6.

2.2.5 Rotary actuators

Sine wave commutated, brushless DC servo motors were chosen as all the actuators for the system. The particular model chosen has 4 pole pairs (8 total magnet poles) on the rotating component of the motor (rotor). In the stationary component (stator) surrounding the rotor, current is run through three sets of windings to generate the electro-magnetic field. The current running through a particular set of windings is referred to as a phase. The current to each phase changes depending on the position of the rotor to give the most efficient torque output. This process is called commutation and is performed in the servo-amplifier.

Each motor was geared up in one gear stage to create the necessary torque ratio.

A pulley was designed to mount on the driven gear with cables anchored inside and routing out from it. This converts the rotary motion of the motor into linear motion in the cables.

Even with the gear stage, it was decided that the motor was light enough and the gearing was low enough that there would be a sufficiently low natural impedance for the robot.

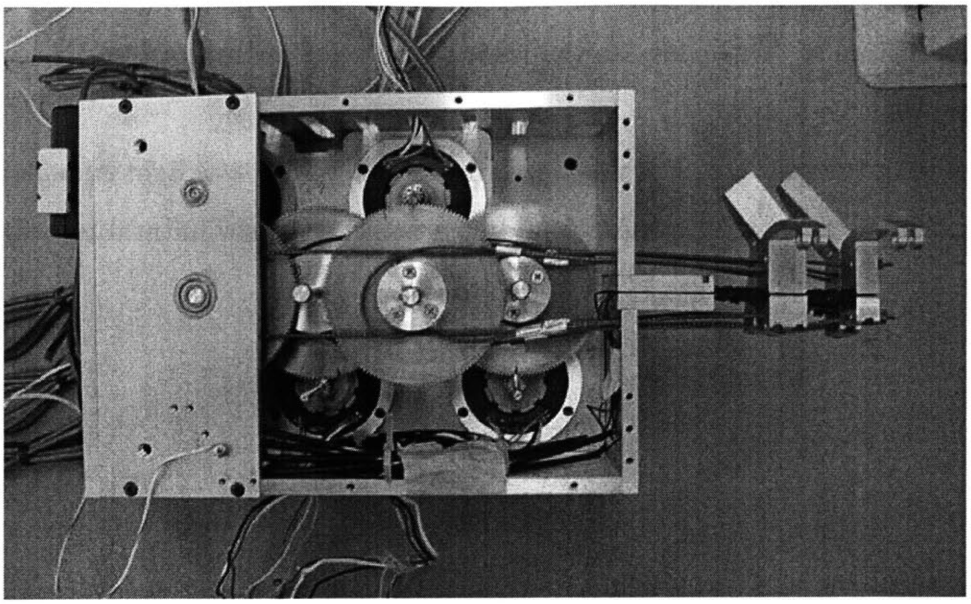

Figure 2-7: Top view of partially assembled finger motors box.

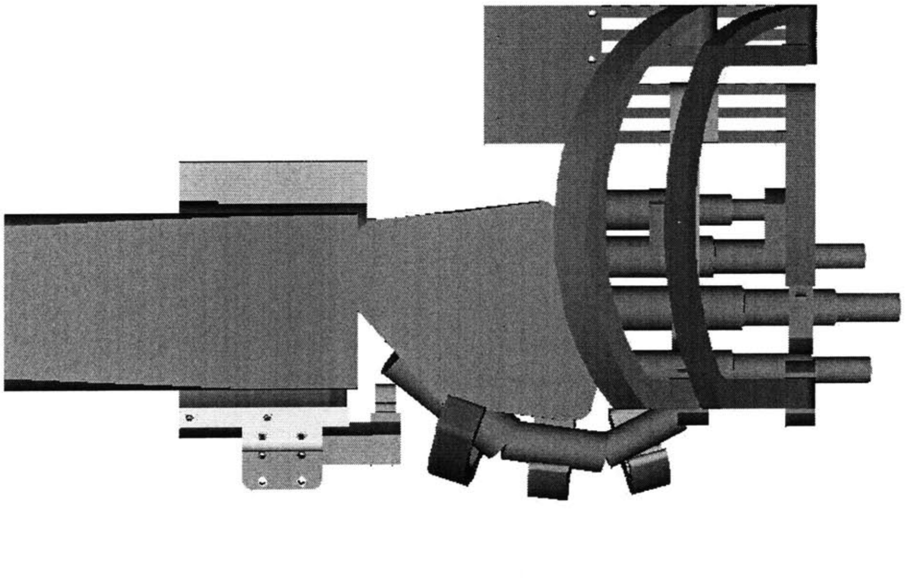

Figure 2-8: Solid model back view of a hand in the robot.

Chapter 3

Prototype Changes

After the design of the robot was complete, a prototype was manufactured for testing purposes. After it had been assembled, some design flaws were discovered that hindered or prevented effective use of the prototype. This chapter describes the mechanical problems encountered, the analysis used to understand these problems, and the changes made to make the prototype functional to a point where tests could be performed.

3.1 Bearing plates

A standard practice in manufacturing is to design parts with a specified tolerance for every dimension. The tolerance establishes a range around the nominal value within which the dimension needs to be. This tells the manufacturer the degree of precision with which he needs to make the part. Some parts, of course, require more precision than others, which normally comes at a higher cost. Once specified, though, the manufacturer does have the responsibility of ensuring each dimension is within tolerance. So, it is up to the engineer to design the part so that it will still function even if all the dimension are at their highest or lowest tolerance values. This proves particularly important for mating parts in assemblies, such as the motor boxes.

Because the servo motors chosen for the robot were frameless, it was necessary for the housing of each motor to be custom designed and manufactured. The eight motors were housed in three separate boxes — one for the four finger motors and two for the thumb, each holding a pair of motors. The base of each motor box was formed out of a block of aluminum, with cavities for the stators and holes for the bottom bearings of the motor and gear shafts. Four $\frac{1}{4}$" aluminum plates were designed to make the sides and a single plate was fastened to the top to complete the box. For the remainder of this thesis, the motors for the index and outer fingers will be referred to by which joint they were meant to actuate — Index MCP/PIP (IMCP/IPIP) and Fingers MCP/PIP (FMCP/FPIP). The motors for the thumb will be referred to by their serial numbers — 691, 692, 693, and 695.

The top bearings for each motor box were all located on their respective top plates. With a gear for each motor, this meant that the finger motor box had a total of eight bearings in its top plate and each thumb motor box had four. Unforunately, some misalignment occurred because the effect of tolerancing was not taken into account in the design of the motor boxes.

The idea of tolerance stacking plays an important role in understanding the reason for this misalignment. Since they were not referenced off the same edge, the position of a bottom bearing relative to its corresponding top bearing depends on some other dimensions, namely the locations of the screw holes fastening the base to the side plates and the side plates to the top plate. In the worst-case scenario, the centerlines of these bearings could be off axis by 0.014" and each part would still be within its specified tolerances.

Although it was unlikely for this to occur for every bearing, it is likely that the eight top bearings in the finger motor box were off from their nominal positions and each probably in a different direction. One would expect that putting on the top plate would be an exceedingly difficult task and indeed it was. When the motor box was assembled, all the shafts probably were bearing some load due to the misalignment of the bearing holes. A simple enough solution was available, however.

The top plate for each of the motor boxes was cut into pieces by a bandsaw so that each piece only held the bearings for one motor shaft and its corresponding gear shaft (see Figure 3-1). The bored holes for the screws provided enough play to correct

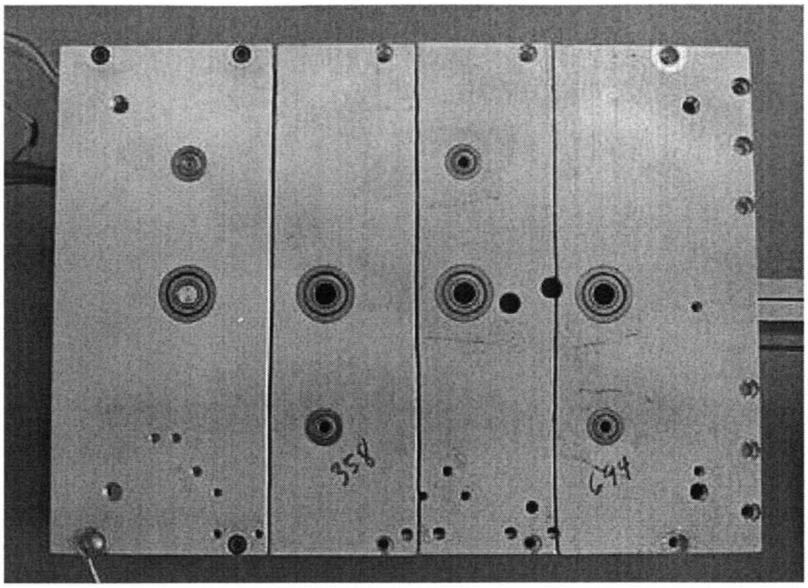

Figure 3-1: Picture of the top bearing plate for the finger motor box after sectioning.

for the magnitude and direction of the bearing misalignment.

3.2 Stator cavity

Once the motor boxes were made easier to assemble, it was discovered that none of the motors could spin freely, either by hand or through actuation from the servoamp. This was due to a design error in the stator cavities that caused each motor shaft to interfere with the base of its motor box.

The base of each motor box was designed so that the stator was clamped down in a large counter-bore. Through this, a smaller bore was made on the same centerline to hold the bottom bearing in a press fit. With the outer diameter of the bearing specified at 0.375", the diameter of the smaller bore was toleranced at 0.3743"-0.3750".

The motor shaft was designed as a series of stepped diameters. The portion of the shaft that went through the motor was designed as a clearance fit to be secured to the rotor with a glue such as loctite. The shaft diameter at this step was toleranced at 0.3735"-0.3745".

From the detailed drawings for these parts, it was evident that the rotor section

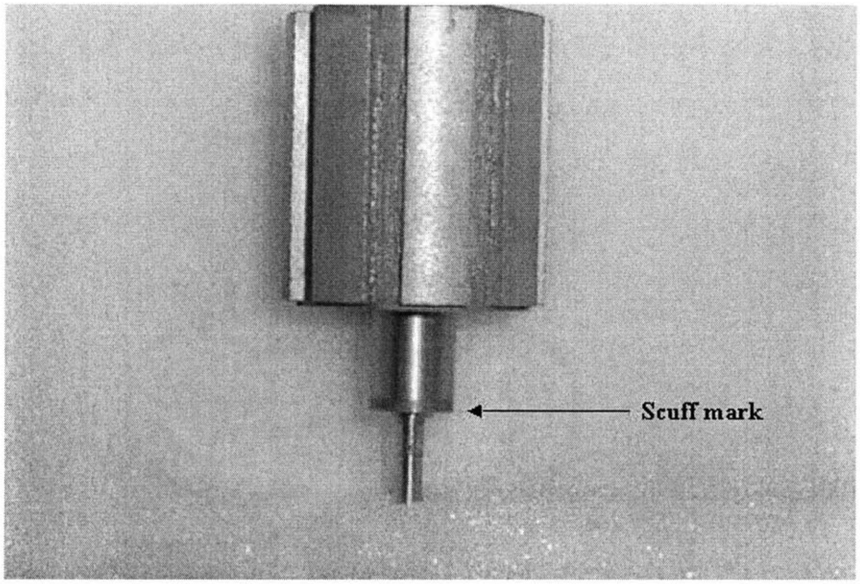

Figure 3-2: A motor shaft from one of the thumb motors after initial assembly. The discoloration at the bottom of the large diameter in the shaft is from the interference with the shaft and the bearing bore.

of each shaft would extend into its bearing bore. Considering the dimensions above, interference was almost guaranteed. According to the national standard, to be a free running fit, there must be 0.0016" of space between the shaft and hole at the maximum material condition [22]. Theory was then confirmed through observation of the hardware. Once removed from the assembly, a portion of each shaft seemed scuffed, as shown in Figure 3-2 — a strong indication that part of the shaft had been stuck in the bore.

Two alternatives were considered to correct this problem. One option was to turn down the sections of interference in the motor shafts. But that involved the risk of damaging the magnets on the rotors during machining. Thus, the option chosen was to counter-bore out the bases of each motor box, since it posed less risk to the hardware.

Using the dimensions and tolerances of the hole and shaft lengths from the drawings, the interference between the shaft and bores was calculated. The cavities for the thumb motors were identical, as were all four shafts at this section. The finger motor

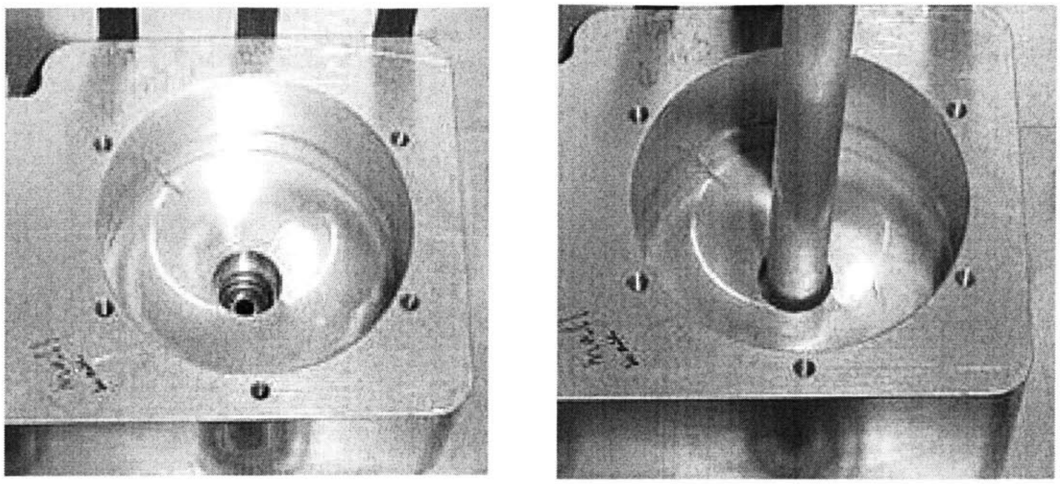

(a) **(b)**

Figure 3-3: **(a)** Typical counter-bore in stator cavity. **(b)** Cavity with $\frac{3}{8}$" shaft stock placed in rotor hole to demonstrate clearance fit.

Motor set	Interference	Counter-bore
fingers	0.269 ± 0.015	0.300
index	0.099 ± 0.015	0.150
thumb	0.039 ± 0.009	0.055

Table 3.1: Depth of interference between the bearing bores and motor shafts calculated from the detailed drawings. The nominal depths of the counter-bores made into the stator cavities are also given. All values in inches.

box had two different sets of dimensions — one for the FMCP and FPIP motors and the other for the IMCP and IPIP motors. The interference dimensions for these sets of motors and the depths of the desired counter-bores are shown in Table 3.1.

After the counter-bores were made in the stator cavities, the interference was eliminated and the motors were no longer immobilized. However, more problems were then encountered.

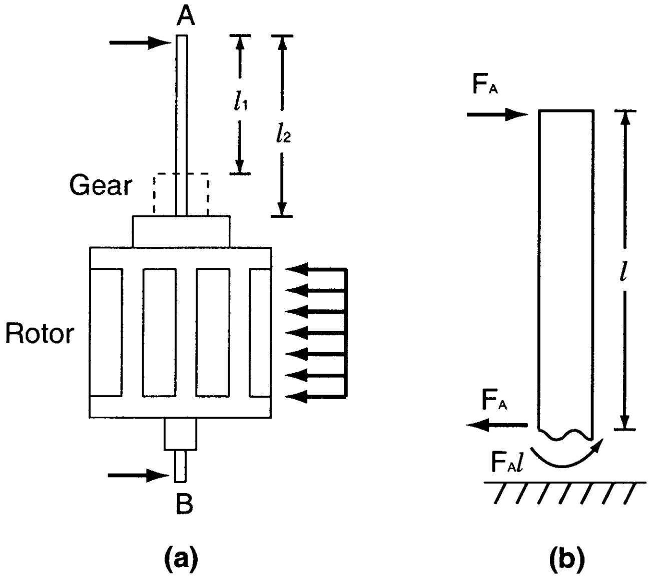

Figure 3-4: (**a**) Free-body diagram of the motor shaft. The load from the top bearing acts at point A. The load from the bottom bearing acts at point B. The load from the magnets being attracted to the coils on the stator is distributed through the length of the rotor. The dotted line shows where the pinion gear is located for most of the shafts, leaving only l_1 exposed. l_2 is the total length of the skinny portion of the shaft. Not to scale. (**b**) Free-body diagram of an arbitrary cut of length l in the top portion of the shaft. The rest of the shaft was assumed to only translate. This allowed the use of the cantilever deflection equation, which simplified the analysis.

3.3 Motor shafts

Without the interference, most of the motors were able to spin freely, but it was observed that many were spinning eccentrically, some so much that that the rotors would brush against the stators. For this particular motor model, the inner diameter of the rotor was specified to have a total runout tolerance from the stator of 0.004". Total runout is the overall variation of the circular and profile surface of a diameter when rotated through 360° and is conventionally given as the total movement of the indicator when properly applied to the surface (total indicator reading) [9]. The interference observed between the rotor and stator was due to a violation of this tolerance, believed to be caused from three possible sources — error in parallelism due to bending in the shafts, manufacturing errors affecting concentricity, and deflection due to side loads from the permanent magnets. Any one of these three modes can cause errors in total runout.

3.3.1 Shaft bending

To fit the pinion gears and the top bearings, a portion of each motor shaft was designed at a $\frac{1}{8}$" diameter. A free-body diagram of the rotor-shaft assembly, as seen in Figure 3-4a, shows that the shaft is loaded similar to a pinned beam in bending. Since the length, l_2, is long and thin relative to the other parts of the shaft, this became the weakest section.

The maximum load the shaft can withstand can be estimated by using elementary static mechanics principles. The intensity of force on an object is called stress and is defined as force per unit area. The equation for the maximum stress in a beam in pure bending is the following [22]:

$$\sigma = \frac{Mc}{I} \tag{3.1}$$

where M is the bending moment, c is the maximum distance from the neutral axis (in this case, half the diameter of the shaft), and I is the moment of inertia. From

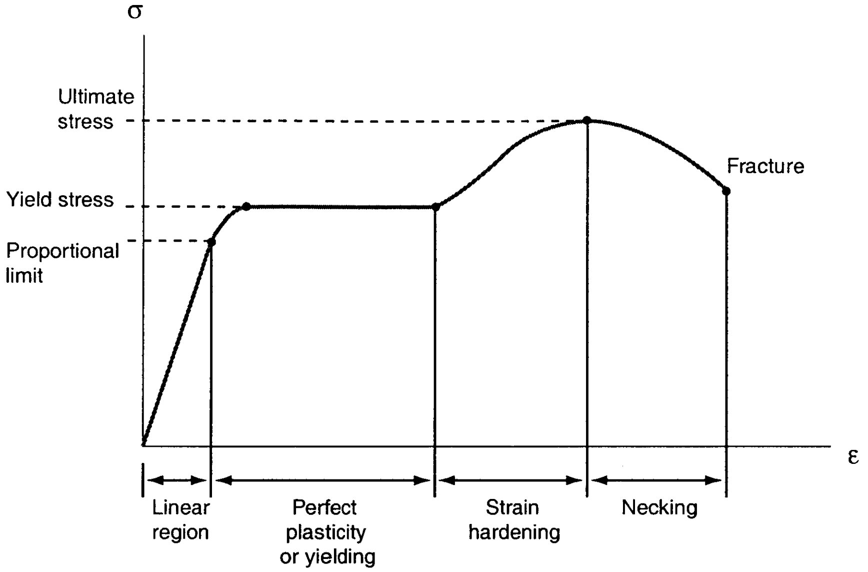

Figure 3-5: Nominal stress versus strain for a typical structural steel in tension.

Figure 3-4b, the bending moment is simply:

$$M = F_a \times l \tag{3.2}$$

And for a cylindrical rod with diameter d, I is:

$$I = \frac{\pi d^4}{64} \tag{3.3}$$

Substituting and rearranging equations 3.2 and 3.3 into equation 3.1, we get:

$$F_a = \frac{\pi d^3 \sigma}{32l} \tag{3.4}$$

The motor shafts were manufactured from 303 stainless steel, which has a yield stress of 35 kpsi [22]. Figure 3-5 shows a typical stress-strain curve for steel, where strain is a unitless term representing elongation per unit length. Typically, the stress-strain relationship is highly linear in what is called the elastic region. For these stresses, the material acts as a spring, following the stress-strain curve during unloading. This is demonstrated by line OA in Figure 3-6a. The yield stress of a

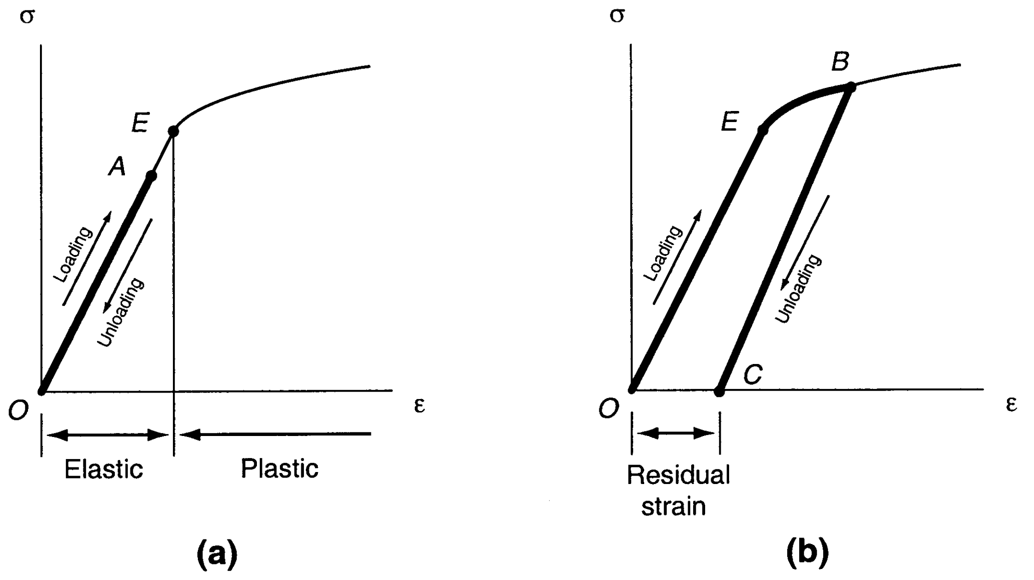

Figure 3-6: **(a)** Loading and unloading in the elastic region of a stress-strain curve. **(b)** Loading and unloading in the plastic region of a stress-strain curve. Point E represents the yield stress.

material is the stress at which plastic deformation occurs, leaving a residual strain after unloading. This is demonstrated by line OBC in Figure 3-6b, where point E represents the yield stress.

Using the yield stress for σ in Equation 3.4, the loads at which plastic deformation would occur in the shafts were calculated and are shown in Table 3.2. The calculations were made using a moment arm of l_1 since the gears were flush with the larger diameter, effectively adding more material to the shaft. The shafts for 692 and 693 were slightly different than the other shafts in that the gear was located further up, not flush with the larger diameter. Those calculations were made using a moment arm of l_2.

From these estimates, it was clear that this section of the shafts was highly susceptible to plastic deformation from bending, which would affect the parallelism of the shaft. A bend at the base of this section would cause the tip to be off axis. Since total runout is measured by the total indicator reading (TIR), the tip needed only to be off by 0.002" to reach the maximum acceptable total runout tolerance of 0.004".

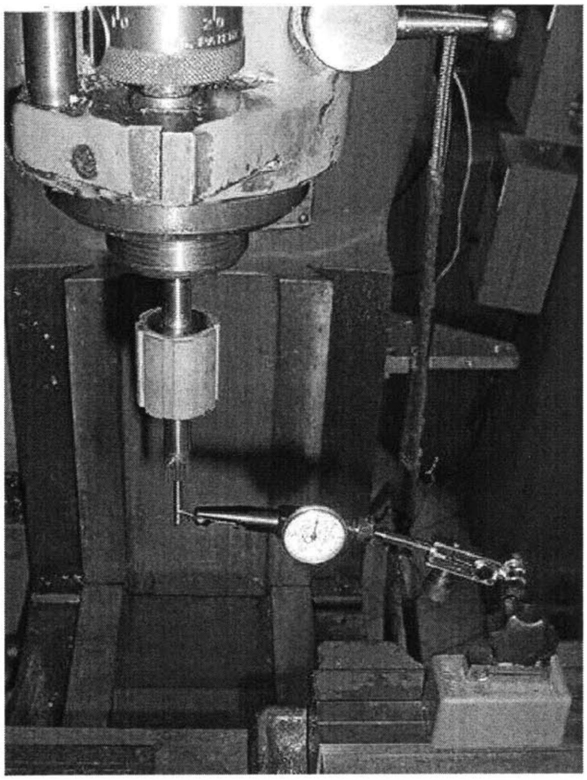

Figure 3-7: Typical setup used to measure shaft parallelism and concentricity.

Motor	Moment arm (in.)	Min end load (lbs.)
FMCP/FPIP	0.875	7.7
IMCP/IPIP	1.87	3.6
691/695	1.655	4.1
692/693	2.155	3.1

Table 3.2: Minimum loads applied by the top bearings before plastic deformation of the motor shafts occurs, as calculated by Equation 3.4. The moment arm used for all shafts was l_1, except for the 692/693 shafts which used l_2, as defined in Figure 3-4.

Motor shaft	Δx	Work?
Fingers PIP	0.000	Yes
Fingers MCP	0.003	No
Index PIP	0.002	Yes
Index MCP	0.003	No
691	0.003	Yes
692	0.000	Yes
693	0.001	No
695	0.002	Yes

Table 3.3: Bend measurements of each motor shaft. Δx is the maximum deflection at the tip, referenced from the centerline of the shaft. The working condition of each shaft is also indicated. A yes means that the rotor and stator did not interfere, although the axis of rotation may have been eccentric. A no means that interference between the rotor and stator were observed regularly. All values in inches.

Thus, the weakness of the shafts was a likely cause of the interference between the rotor and stator.

To confirm the error in parallelism, each shaft was measured in a milling machine. The bottom end of the shaft was secured in a $\frac{1}{8}$" collet which was inserted into the spindle of a milling machine. With the rest of the shaft facing downward, a dial indicator was fastened to the table and positioned to lightly touch the shaft. Because the centerline of the shaft was concentric with that of the spindle, it was perpendicular to the table. Thus, when the spindle was moved up and down, a non-parallel surface on the shaft resulted in movement of the dial indicator. An example of the test setup is shown in Figure 3-7.

It was assumed that there was no bend in the shaft until its weak section. The dial indicator was referenced at the first exposed part of this section. The spindle was then moved down to the tip of the shaft and the displacement of the dial indicator was recorded. Measurements were taken at different spindle positions so the plane of bending and the maximum deflection of the shaft could be determined. Table 3.3 shows these values and the working condition of each motor at the time of measurement. The motors that did not work all created more than 0.004" total runout from the bend in their shafts, except in the case of 693.

A number of causes could be responsible for these apparent bends. These include:

- Normal handling — A small, unsuspecting moment may have been created on the shafts through normal handling. At the time, it may not have been a concern since the weakness of the shafts was unknown.
- Gear assembly — To assemble the pinion gear, a dowel pin was press fit into concentric holes on both the gear and the shaft. The forces required for this press fit may have created enough of a moment to bend the shafts.
- Motor box assembly — As mentioned earlier, it was difficult to fit the top plate on the motor boxes because of all the bearings that had to be aligned. It is likely that the mislocation of the bearings kinematically constrained the shafts and created large enough forces to bend them.

It should be noted that 692 initially did not work. The cause, however, was discovered to be a bearing mislocation (even after the top bearing plate was cut). This was easily solved by allowing more play in the top plate, created by boring out the through holes for the bolts.

As for 693, another source of error was responsible for its non-working condition.

3.3.2 Shaft concentricity

Although the bend in the shaft for 693 was small enough to stay within the tolerance range, the motor still did not spin correctly, which suggested the possibility of another mode of failure. While rotating the spindle with the shaft still secured in the milling machine, it was quite evident that the tip was not on the same centerline as the rest of the shaft. This was due to a manufacturing defect where the centerline of certain diameters of the shaft were not concentric with the others. This can occur if one half of the piece were cut first and then flipped around and reinserted into the lathe to cut the other half. A defect in the chuck or error in fixturing could cause the piece to not be absolutely centered.

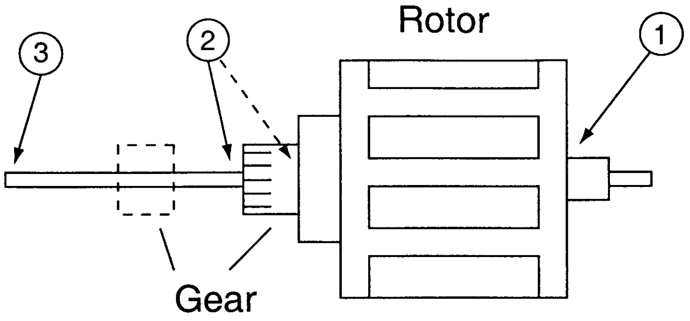

Figure 3-8: Sketch of a motor shaft, labelling where runout measurements were taken. The dotted line represents the gear and measurement locations for motors 692 and 693.

To get an estimate of the concentricity of each shaft, the same test setup as before was used (see Figure 3-7). This time, however, the milling machine was turned on and the spindle was spun at low speeds. Thus the total range that the dial indicator moved measured the runout at that cross-section of the shaft. This only provides an estimate for the error in concentricity, however, because runout measures the overall variation of the shaft, including circularity, cylindricity, and straightness. Measurements were taken at different locations along the shafts to determine the diameter where the error in runout occurred (see Figure 3-8).

Table 3.4 shows the recorded values at these locations. These observations provide some more insight explaining the behavior of the motor shafts:

- The shafts for the FMCP and 693 motors are greatly out of tolerance and it is no surprise that both their motors experience interference between the rotor and stator.
- The tip of the shaft can have a runout of 0.009" and no interference will be observed. Although the total runout tolerance for the rotor is specified at 0.004", exceeding this tolerance does not necessarily mean interference will occur. The tolerance most likely needs to be met for the motor to behave within its given specifications. So although these motors can spin freely, they most likely will not behave ideally.

Motor shaft	Δx	$\Delta\phi_1$	$\Delta\phi_2$	$\Delta\phi_3$	**Work?**
Fingers PIP	0.000	0.000	0.003	**0.005**	Yes
Fingers MCP	0.003	0.002	**0.018**	**0.025**	No
Index PIP	0.002	0.000	0.001	0.003	Yes
Index MCP	0.003	0.000	0.002	0.004	No
691	0.003	0.001	0.001	**0.009**	Yes
692	0.000	0.000	0.002	**0.005**	Yes
693	0.001	0.003	**0.023**	**0.029**	No
695	0.002	0.000	**0.005**	**0.009**	Yes

Table 3.4: Initial runout measurements (TIR) for each motor shaft at locations 1, 2, and 3, as defined in Figure 3-8 . $\Delta\phi$ refers to the runout error at a particular location. Bold-faced entries represent values that were out of tolerance. Data from Table 3.3 is repeated here for comparison. All values in inches.

- The IMCP shaft seems to be within tolerance, yet interference is still observed. Further investigation was needed to explain this phenomenon.

3.3.3 Magnetic load

A permanent magnetic field exists around the rotor because of the magnets attached to its side. The intensity (and brittleness) of these magnets is why one must be careful when handling them. When they come near a ferrous material, a very strong attractive force is generated. This holds true at all times, even when the rotor is assembled with the stator. And because the windings in the stator contain some iron, the rotor is naturally pulled toward the stator in the assembly.

This may not pose a problem if the rotor is perfectly centered within the stator. The symmetry of the rotor and stator will cause all forces to cancel out vectorially. However, it is an unstable system, similar to an inverted pendulum. With a small deflection in any one direction, the forces become unbalanced and increase with time. As the above analysis and measurements show, these motor shafts are far from ideal and are not concentric with the stator. Only the top and bottom bearings are keeping the rotor kinematically constrained from that movement.

However, the bearings can do nothing to prevent deflection in the shafts. Again,

Motor set	Min end load
FMCP/FPIP	2.962
IMCP/IPIP	0.303
691/695	0.438
692/693	0.198

Table 3.5: Minimum loads applied by the top bearings to deflect the motor shafts 0.002", as calculated by Equation 3.6. All values given in pounds.

the long, thin length of the shaft is considered to be the weakest section. From Figure 3-4b, adding a load on the shaft from the magnetic force in the rotor will create shear and moment forces. To roughly estimate the deflection due to these forces, it was assumed that the rest of the shaft only translated. Thus, this portion of the shaft could be analyzed as an end-loaded cantilever, which has the following equation for deflection [22]:

$$\delta = \frac{Fl^3}{3EI} \tag{3.5}$$

where E is Young's Modulus. Rearranging to get a stiffness equation (force/distance) and using Equation 3.3, we get:

$$k = \frac{F}{\delta} = \frac{3\pi E d^4}{64 l^3} \tag{3.6}$$

Using $E = 27.6$ Mpsi as the Young's Modulus for stainless steel, the loads by the top bearings required to deflect each shaft 0.002" were calculated and are shown in Table 3.5. The moment arms used were the same as those used for Table 3.2. Because of the assumptions made, the results probably underestimate the true values, but they at least provide a glimpse as to the order of magnitude involved.

It is clear that only light loads are required to deflect these motor shafts out of tolerance. It is highly likely, then, that once in the assembly, the shafts will be deflected out of tolerance by the magnetic attraction between the rotor and the stator. Again, theory was confirmed through observation when more measurements were taken.

The IMCP shaft was assembled with its driven gear in the motor box without the

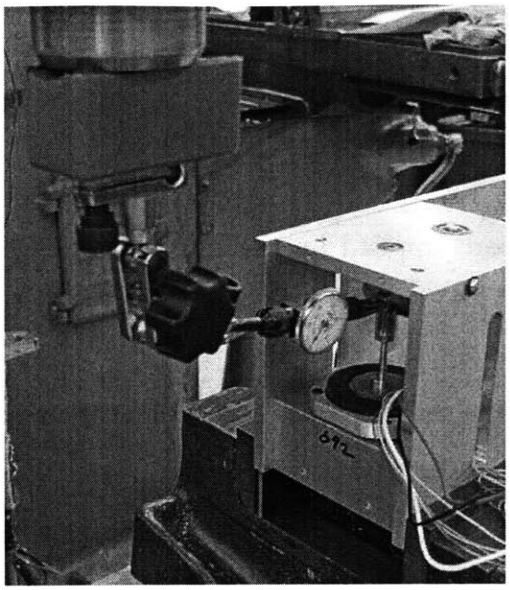

Figure 3-9: Setup for measuring runout of one of the thumb motors in assembly. The setups for other motors were similar.

stator. The box was then clamped to the table of a milling machine, with the base parallel to the table. A dial indicator was then attached to the spindle and moved into a position where it could touch the shaft, similar to the setup shown in Figure 3-9. The driven gear was spun by hand to rotate the shaft. The runout was measured to be $\Delta\phi_2 = 0.005"$. It was not surprising that this value was different than that given in Table 3.4. Since the shaft was being spun by the gear, some side load was introduced, likely enough to deflect the shaft because of its structural weakness. Play in the bearings could also have affected these measurements, although visibly there did not seem to be much.

The IMCP shaft was then assembled with its stator. The runout was measured as before, yielding $\Delta\phi_2 = 0.028"$. Just to ensure that the shaft had not been bent or damaged in between those two tests, the IMCP shaft was measured again by itself, in the same manner as for the initial runout measurements. The result was close to its original value, with $\Delta\phi_2 = 0.001"$. This provided clear evidence that the stator was introducing enough side load to deflect the motor shaft.

It is interesting to note that this deflection was not as prominent in the IPIP shaft

Motor shaft	$\Delta\phi_1$	$\Delta\phi_2$	$\Delta\phi_3$
Fingers MCP	0.002	0.002	0.009
Index MCP	0.000	0.001	0.005
693	0.000	0.002	0.005

Table 3.6: Runout measurements (TIR) for the new motor shafts after assembly to rotors and gears. All values in inches.

even though it is identical to the IMCP shaft. Measurements showed that for the IPIP shaft assembled with the stator, $\Delta\phi_2$ ranged between 0.003"-0.008". The range was due to loading from the driven gear. An accurate value did not seem possible during the measuring process, but at least the order of magnitude was determined.

Because there is so little room for error in these shafts, their weakness might be exaggerated by small defects in material or manufacturing. The difference in behavior between these two shafts might be from a subtle difference in the strength of the stock or slightly different diameters or both. The question seems interesting, but given the scope of the work described here, an in-depth investigation did not seem warranted.

It should be noted that the error in runout was specific to each shaft, not the housing or stator. When assembled into its twin's stator, each rotor showed the same behavior as observed in its own stator.

3.3.4 Replacements

Because of their manufacturing errors, the FMCP and 693 shafts were replaced. The IMCP shaft was also replaced in the hope that the material or manufacturing defect that caused it to deflect so much more than its twin would be corrected. Measurements were taken again after the rotors and gears were inserted and are shown in Table 3.6.

These measures were consistent with the other working motors. Once assembled into the housing, interference between the stator and rotor was not observed. However, there was significant deflection (especially for the IMCP and 693 shafts) because of the side loads from the magnets, and the rotors had visible eccentric rotation. When additional side loads were added, either by hand or the driven gear, interference would occur.

It was decided that the design for the motor housing was unacceptable. By not being able to support very much end load or side load, the shafts compromised the performance of the motors too much. A redesign of the motor box was needed so that the rotors could stay within their total runout tolerance. However, before this was done, it was still possible to gather some useful information about the design features of the robot through the working motors.

To simplify the analysis and because the working condition of many of the motors was impractical, the system was reduced to one degree of freedom. The Fingers PIP joint was chosen since its motor shaft was the least susceptible to bending and because its transmission was relatively simple. The following chapters describe the experiments and analysis performed using this motor.

Chapter 4

Electrical Subsystem Characterization

Before any definitive conclusions about the design features of the robot could be made, the behavior of every component in the system first needed understanding. This chapter begins with a brief overview of the electrical subsystem, then focuses on the characterization of the components, most importantly the servo-amplifier and the actuator.

4.1 Subsystem overview

To present a clearer picture of the signal progression, a schematic of the system is provided in Figure 4-1. The computer acts as the headquarters of the system where signals are received, processed, and sent. The computer itself is controlled by an extensive C++ library, running in the QNX real-time operating system on an 800 MHz Pentium III processor. As a digital device, however, the computer could only operate in discrete time, or samples. The sampling frequency for all tests using the computer was 1000 Hz.

At the start of each sample period, the computer reads in information from multiple sources, sensors in the physical world that convert mechanical information to voltage. Analog voltage input is read from a programmable number of channels in

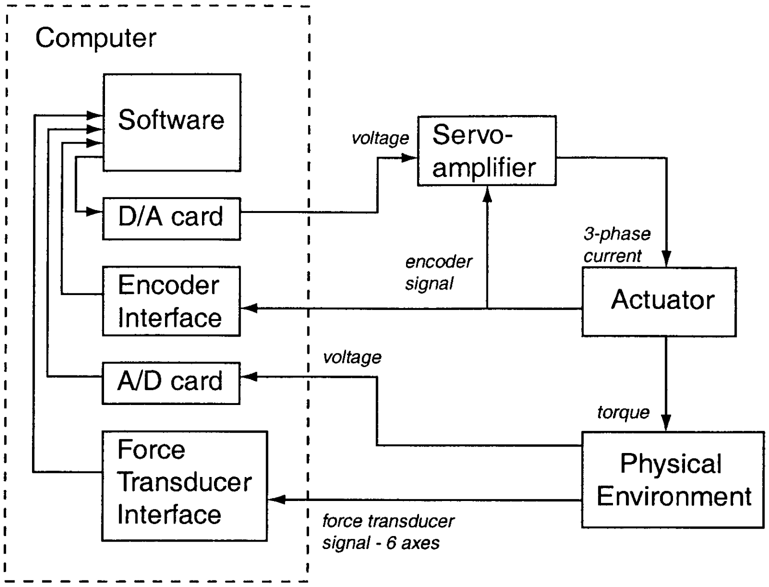

Figure 4-1: Electrical subsystem schematic.

the analog-to-digital (A/D) card. Next, position information from the encoders are read. Finally, if needed, the information from the force transducer is read. The software then processes this information and calculates a control input voltage. This is then sent from the digital-to-analog (D/A) card to the servo-amplifier. Using the encoder signal and an internal commutation table, the servo-amp outputs a current to the motor proportional to its input voltage. The motor then converts the electrical power to mechanical power in the form of torque. This torque is converted to tension in the cables, which then drive the robot joint.

A PD2-MF-16-50/16H UEI multifunction board was used for both the A/D and D/A channels. A PC7266-D US Digital encoder card was used to read the Gurley Precision encoders. A 16-bit, 6-axis ATI model Gamma force transducer and ISA-bus interface card were used for force sensing.

4.2 Current sensor

A custom, three-phase current sensor was built from analog components in order to characterize the servo-amp. The sensor was built to measure the differential voltages

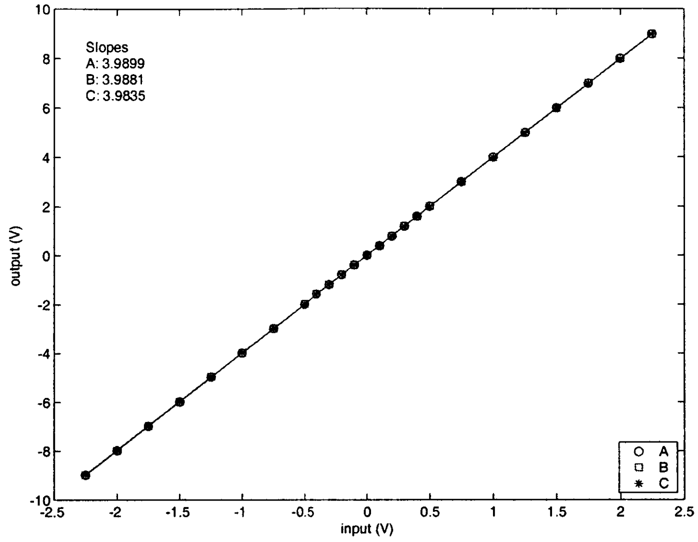

Figure 4-2: Response of the current sensor to DC voltage input. Data from each phase and their linear fits are shown.

across three 0.1Ω resistors placed in the lines between the servo-amp and motor. The output voltage of the sensor was proportional to its input voltage and, thus, input current because of the linear behavior of the resistors ($V = IR$). But before any measurements on the servo-amp could be taken, the sensor's behavior needed to be fully understood.

4.2.1 Static response

The current sensor was built to have a linear input-output relationship. To ensure that this relationship was true, the static response of the sensor was recorded for a range of inputs. Each phase was tested separately by applying a constant voltage to its input wires using a D/A channel from the computer. The output voltage was then measured with a multimeter. Figure 4-2 shows the response of each phase plotted with a linear fit. As was expected, the static response was well-behaved and highly linear, and the response from each phase was almost identical.

The leads of the phases were then connected with the resistors to a screw-terminal panel, making it easier to add and remove the sensor from the motor-servo line.

Phase	+A	-A	Avg
A	0.462	0.460	0.461
B	0.439	0.437	0.438
C	0.434	0.433	0.433

Table 4.1: Current sensor calibration data. All values given in $\frac{\text{Volts}}{\text{Amps}}$.

The little resistance added from the screw terminals, however, affected the readings significantly. To calibrate the sensor, then, each phase was connected in series through the screw-terminal panel and ±1 A of current was sent through the circuit from a BK Precision model 1760 power supply. The output voltage was again measured with a multimeter and the results are shown in Table 4.1. All analysis performed for tests using the current sensor data used the average gain values.

4.2.2 Frequency response

To ensure that dynamics from the current sensor would not affect future tests, a frequency response test was performed. A Leader model LG1301 function generator was used to input voltage sine waves at various frequencies to the leads of the sensor. A Lecroy LT224 digital oscilloscope was then used to measure the output voltage. Each phase was tested and the magnitude and phase data were recorded from the oscilloscope. Figure 4-3 shows the typical response from one of the phases.

An analog low-pass filter was incorporated into each phase of the current sensor. The theoretical cutoff frequency for the 2-pole Butterworth filter was 928.2 Hz. A model of this filter was created and its simulated response was plotted over the data (see Figure 4-4). As expected, the filter accounted for the drop off near 1 kHz and dominated the response of the sensor.

Effect of sampling

Because the oscilloscope had a published bandwidth of 200 MHz, well beyond the range of what was tested, its dynamics were assumed to not have an effect on the

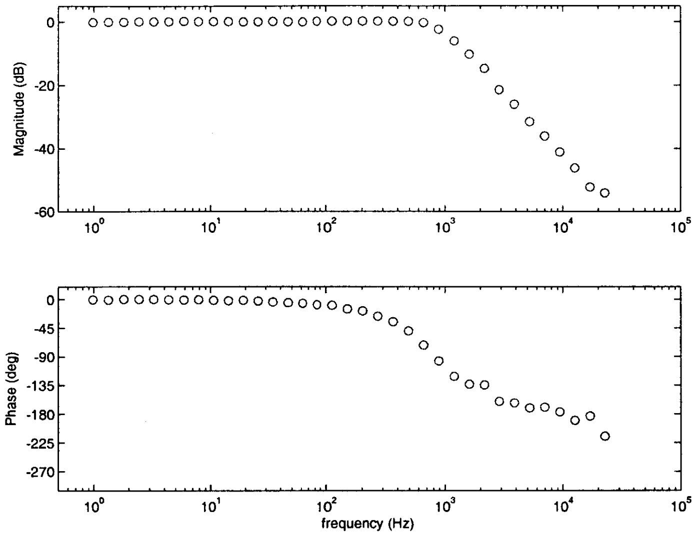

Figure 4-3: Current sensor phase A frequency response. Voltage output/input.

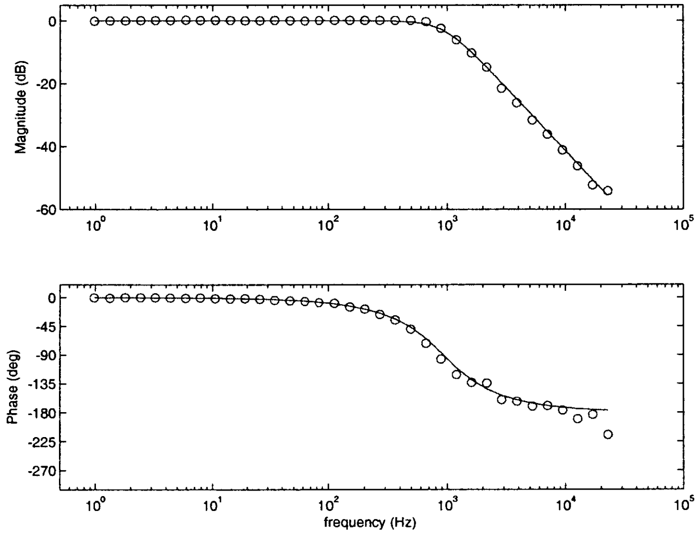

Figure 4-4: Current sensor phase A frequency response plotted with a fitted model.

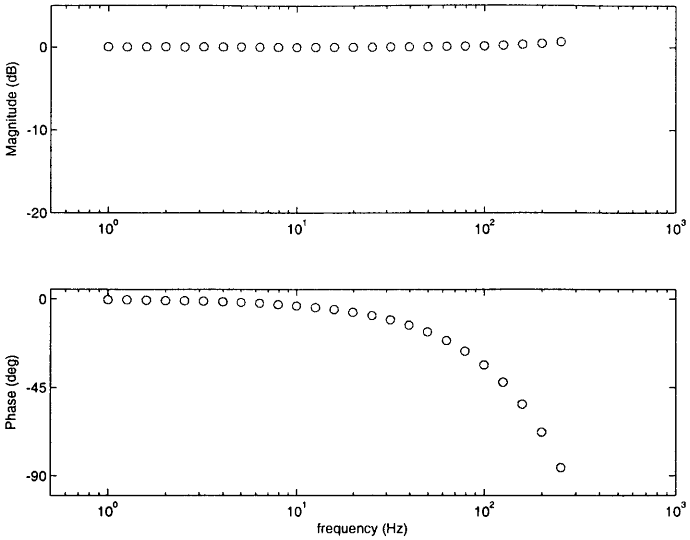

Figure 4-5: Current sensor phase A frequency response from discrete-time test. Voltage output/input.

data. Thus, the results above can be considered to be the behavior of the current sensor in continuous time. When a similar test was performed with the computer, however, a much different result was obtained.

In this test, the input leads of the sensor were connected to a D/A channel from the computer. The output was then connected to three A/D channels. Again, voltage sine waves of varying frequencies were input to the sensor. Because sampled data is only useful up to the Nyquist frequency (half the sampling rate), the maximum frequency tested, 250 Hz, was significantly less than that tested by the function generator. Using the `fminsearch` function in Matlab, the output at each frequency was fit with a sinusoid. Magnitude and phase values were then determined from these fits. Figure 4-5 shows the typical response from one of the phases. The most noticeable difference from Figure 4-3 is in the phase relationship and is due to the effect of discrete sampling.

In each sample period, reading of the A/D comes before writing to the D/A. Once written, the D/A channel maintains its value until the next write is performed. Thus, the effect from the output is not read until the next sample period. Because the timer

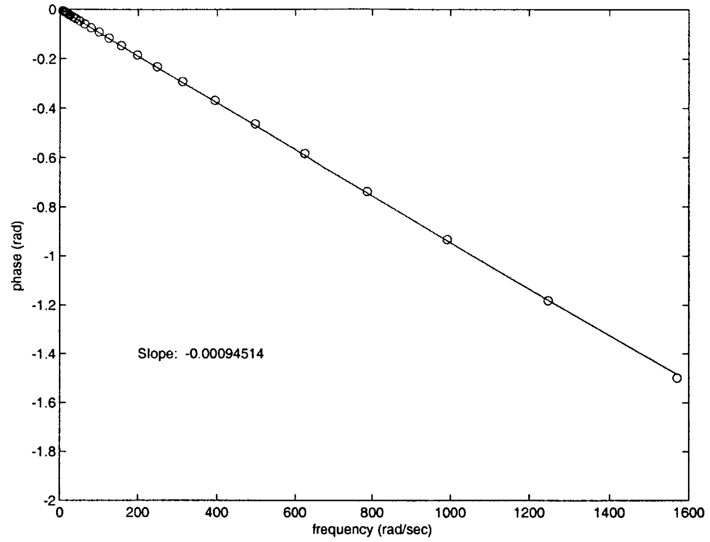

Figure 4-6: Phase lag of discrete-time frequency response test plotted on a linear scale. Magnitude of the slope of the linear fit corresponds to time delay.

is only keeping track of sample times, however, both read and write are approximated as having occurred at the same time, namely the nominal sample time. The result is that a delay of one sample period is incorporated into the output data. The magnitude response remains unchanged. But the phase response becomes linearly dependent on the frequency, governed by the following equation:

$$\phi = T\omega \tag{4.1}$$

where ϕ is the phase lag, T is the sample period, and ω is the frequency.

Looking at the phase lag from this test on a linear scale (see Figure 4-6), the phase data is indeed linearly dependent on the frequency. The slope of the linear fit is also very close to the sample period, 0.001 seconds.

The model created from the continuous-time test was converted to a discrete-time model. The simulated response was plotted over the experimental data and, as Figure 4-7 shows, its accuracy verifies that the effect of sampling has been taken into account by the discrete-time model.

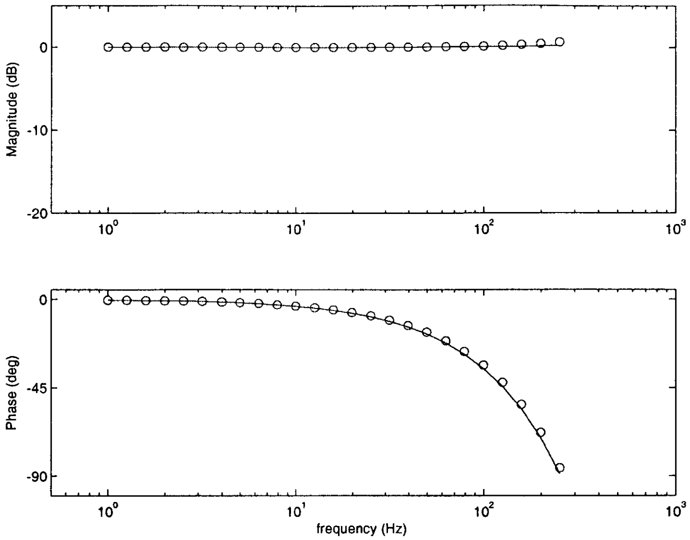

Figure 4-7: Current sensor phase A frequency response from discrete-time test with a fitted model.

The responses from phases B and C in every test were almost identical in every case and their figures be found in Appendix A.

4.3 Servo-amplifier

The Kollmorgen Servostar CD model CE06 was the servo-amplifier chosen to drive each motor. As the system diagram in Figure 4-1 shows, the servo-amp receives the voltage command from the computer and position information from the encoder. It then outputs three phases of current, the magnitudes of which are dependent on the electrical position of the motor. The overall current magnitude is proportional to the voltage input and can be computed through phasor analysis of the line currents.

4.3.1 Static response

The constant of proportionality from voltage to current within the servo-amp is configurable through software. Because the current at peak torque for the motor exceeded that of the servo-amp, this constant was set to its maximum, 2.55 $\frac{\text{Amps}}{\text{Volt}}$. To ensure

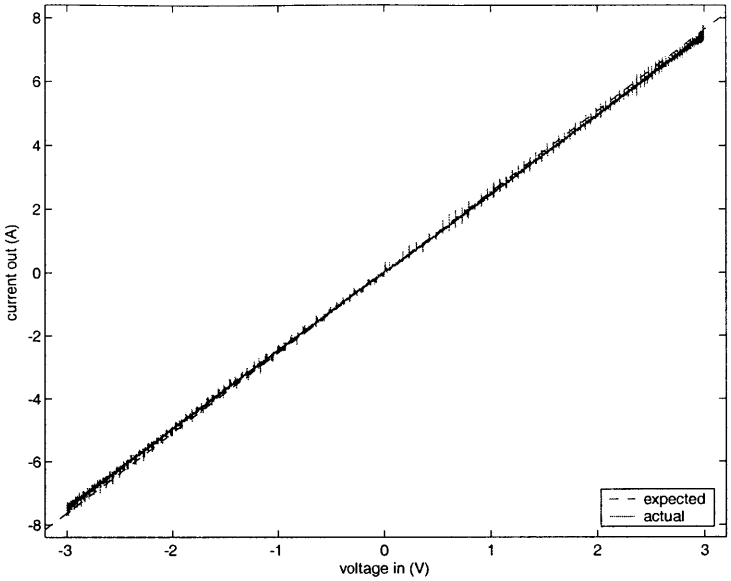

Figure 4-8: Kollmorgen CE06 servo-amplifier static response. Expected and actual current out versus voltage in.

that the servo-amp behaved as expected, a quasi-static test was performed.

After locking the rotor, the amp was given a very slow sine wave (period of 20 sec) voltage input by one channel of the D/A. The magnitude was specified to just below the continuous current limit of the motor. Three A/D channels measured the output from the current sensor. The current magnitude was computed off-line and compared to its expected value. As Figure 4-8 shows, the relationship between output current to input voltage is quite linear. The slope was only slightly lower than expected, differing by less than 2.5%.

4.3.2 Frequency response

A frequency response test of the servo-amp was conducted similarly to that of the current sensor. As in the static response test, the test was performed with a locked rotor. The function generator was used to input voltage sine waves to the amp, and the oscilloscope was used to measure the output from the current sensor. Magnitude and phase data were recorded and then plotted against frequency. As Figure 4-9 shows, the performance of the amp starts to degrade around 100 Hz.

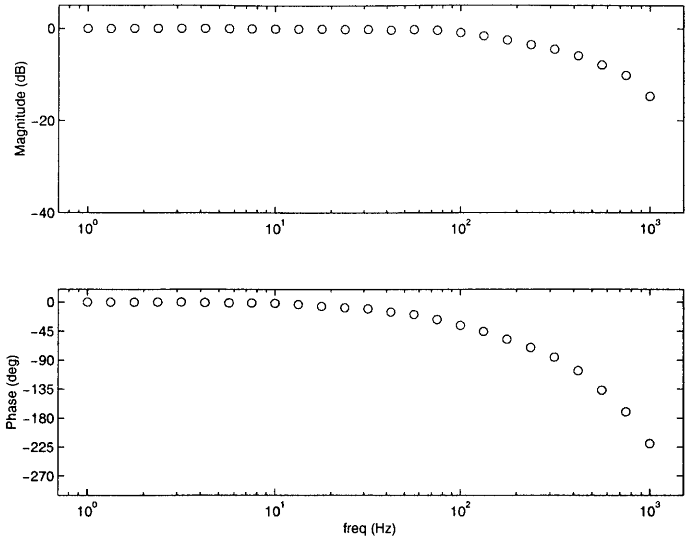

Figure 4-9: Frequency response of the servo-amplifier in the continuous-time domain. Magnitude and phase versus frequency, current out/voltage in.

To characterize this behavior, a model of the amp was created to fit the data. A first-order roll off with a break frequency of 250 Hz was included. This was probably due to the motor dynamics rather than the amp itself. A simple electrical model of a motor is a linear inductor and resistor in series. With L representing the inductance in henries and R the resistance in ohms, the time constant is simply [12]:

$$\tau = \frac{L}{R} \tag{4.2}$$

and the break point occurs at [10]:

$$\omega_c = \frac{1}{\tau} = \frac{R}{L} \tag{4.3}$$

Using the published inductance and resistance of the motor, 0.47 mH and 0.733Ω, and converting units from radians/sec to hertz, the theoretical break frequency is thus 248.2 Hz.

A pure delay of 100 μsec was also added to the model to get a better fit in the phase data. It was assumed that this was due to processing time in the amp.

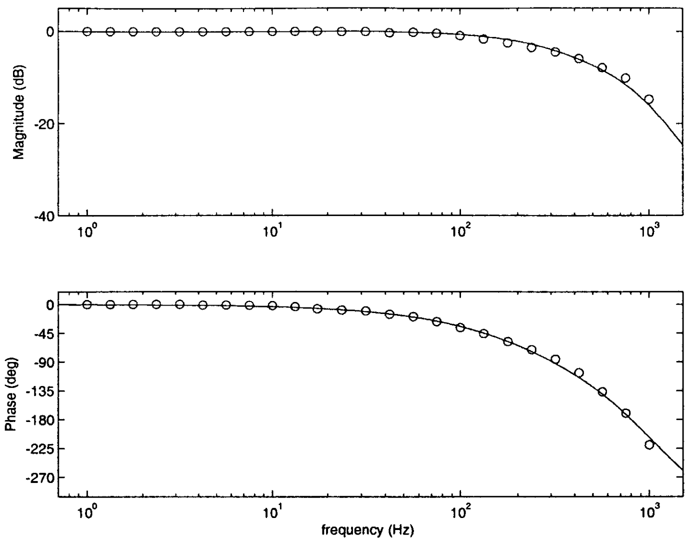

Figure 4-10: Frequency response of the servo-amplifier in the continuous-time domain with a fitted model. Magnitude and phase versus frequency, current out/voltage in.

The model for the servo-amp was then added to the model of the current sensor dynamics and the response was plotted on top of the data, shown in Figure 4-10. Normally, a servo-amp is designed to compensate for its motor dynamics. The close fit between the model and data, however, suggests that this particular series of servo-amps does not.

To confirm the accuracy of the model, the frequency response test was performed again, using the D/A and A/D of the computer. The magnitude and phase data were determined similar to the discrete-time frequency response test of the current sensor. The model incorporating the current sensor (low-pass filter) and the amp (first-order roll off and pure delay) was converted from the continuous-time domain to discrete-time and its response was compared to the data. Figure 4-11 shows that the model response, although not a perfect fit, follows the trends in the data closely. The model was thus deemed sufficient for this subsystem.

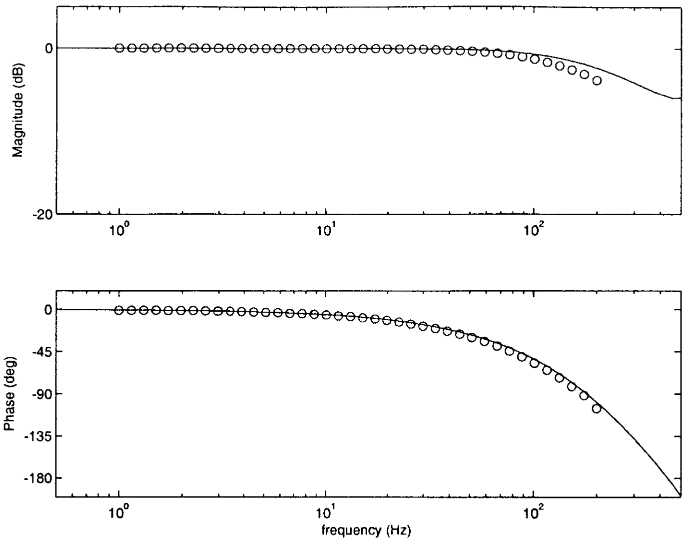

Figure 4-11: Frequency response of the servo-amplifier in the discrete-time domain with a fitted model. Magnitude and phase versus frequency, current out/voltage in.

4.4 Actuator

The Kollmorgen RBE-01213-A02 motor was the motor model chosen for all eight actuators of the system. An ideal motor has a linear relationship between current in and torque out, related by its torque constant. The locked-rotor tests described in this section determined the torque constant for the FPIP motor and its frequency response.

4.4.1 Test setup

The apparatus used to transmit the torque from the motor to the force transducer was custom-designed and machined. At the end of a bar of aluminum, a circumferential clamp was made in order to grasp the motor shaft (see Figure 4-12). The other end of the bar was anchored to a plate attached to the force transducer, which was in turn grounded to the motor box (see Figure 4-13). From the given geometry, the motor torque could be determined from readings of five of the six axes on the force transducer. A more detailed analysis of the torque composition can be found in

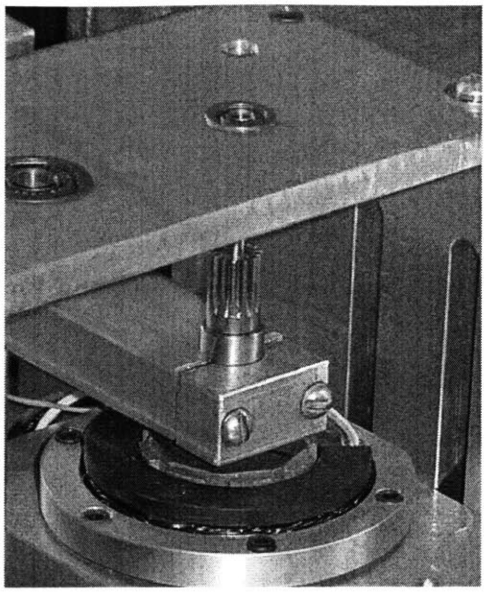

Figure 4-12: Torque-sensing apparatus: circumferential clamp used to grasp the motor shaft.

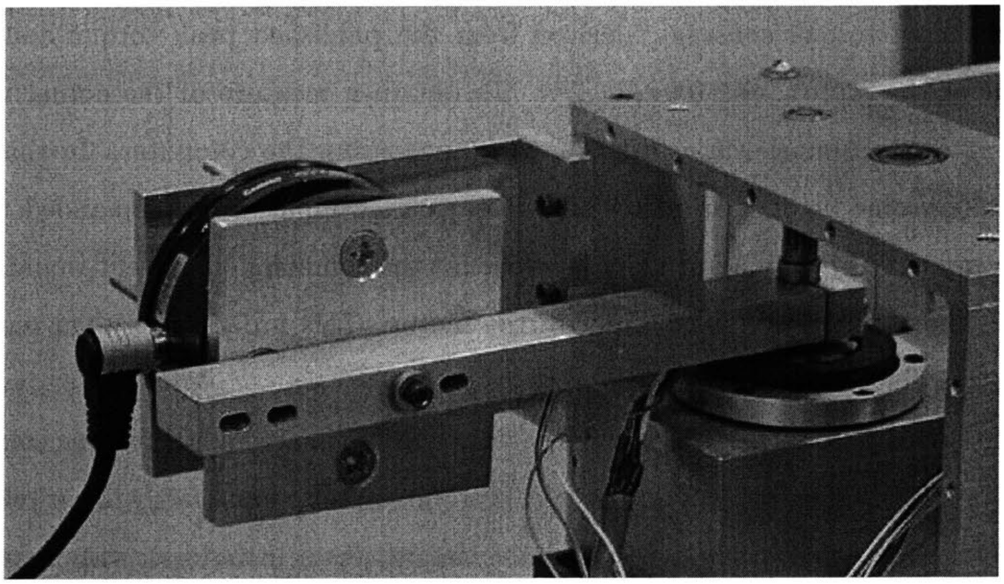

Figure 4-13: Apparatus and setup used in tests to measure torque from the FPIP motor.

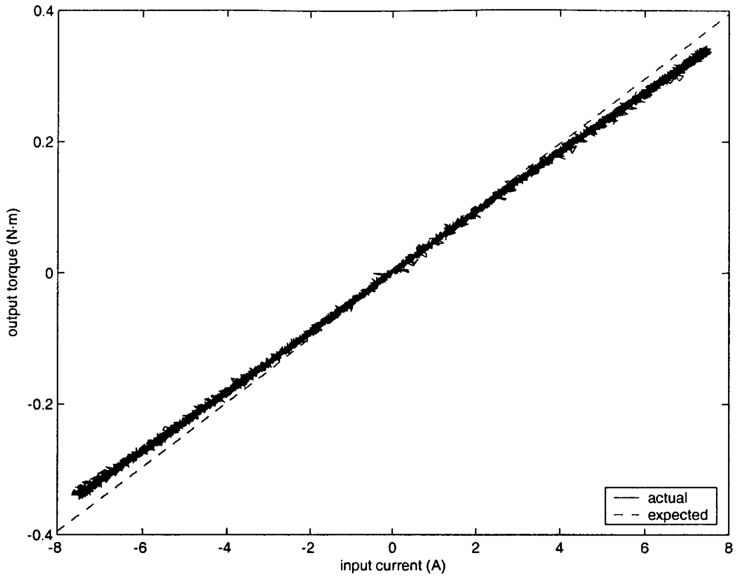

Figure 4-14: Expected and actual output motor torque versus measured input current magnitude.

Appendix C.

4.4.2 Static response

The expected torque constant, derived from the published peak torque and peak current of the motor, was 0.0493 $\frac{\mathrm{N{\cdot}m}}{\mathrm{A}}$. To obtain a measure of the actual torque constant (K_t), a quasi-static test was performed using the computer. In this test, a very slow sine wave (period of 20 sec) of voltage input was commanded to the servo-amp. The given magnitude was such that the commanded current would never surpass the continuous current limit of the motor. This process was then repeated for several different positions of the rotor.

The slope of the linear fit through the data was designated as the torque constant. As Figure 4-14 shows, although the typical torque response has a fairly linear relationship to the measured current, the torque constant was a little lower than expected. The loss in efficiency may be due in part to the poor design of the motor housing.

The torque constant itself was observed to change with rotor position. From Figure 4-15, one can see that there are well-defined, periodic peaks at about every 45° of

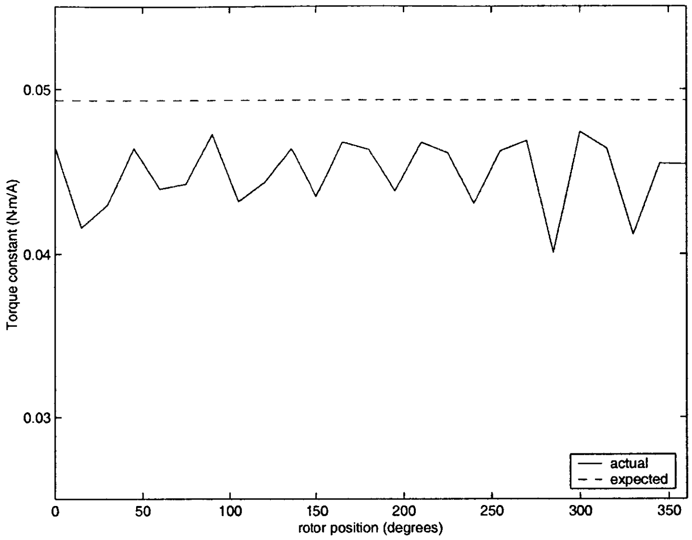

Figure 4-15: Torque ripple effect observed in the motor.

mechanical rotation. This periodic torque variation is known as torque ripple. One contributing factor to this effect is cogging, a term used to describe a phenomenon where the permanent magnets on the rotor seek a preferred orientation with the windings in the stator. This results in a non-uniform attraction dependent on the angular position of the motor. The data is consistent with cogging as the source of the torque ripple shown here since the peaks in torque constant appear at the same spacing as the motor poles. However, other factors may be involved as well. To simplify future analysis, the torque constant of the motor was estimated as the mean of all these trials for a K_t of 0.0449 $\frac{\mathrm{N{\cdot}m}}{\mathrm{A}}$, which is 9% less than expected.

Angle advance feature

Kollmorgen motors and servo-amps are equipped with a patented feature called angle advance. It supposedly increases the maximum potential velocity of the motor by commutating ahead or behind in the commutation table by a user-specified number of electrical degrees. The test described above was performed with this feature turned off. To investigate the effect of angle advance, a similar series of tests were performed

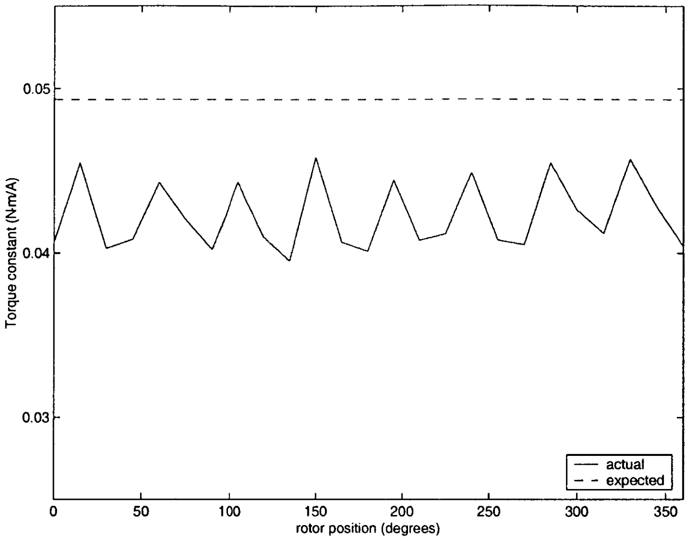

Figure 4-16: Torque ripple in the motor with angle advance parameters set to default values.

with the relevant parameters set to their default values.

The results of these tests, as seen in Figure 4-16, show that the torque ripple is similar in magnitude and period. However, the mean K_t is 0.04225 $\frac{\text{N·m}}{\text{A}}$, which is 14% less than the expected value. This seems reasonable considering it was utilizing a less efficient commutation scheme. To maximize the motor's efficiency, the angle advance feature was left off for the work described here.

4.4.3 Frequency response

A frequency response of the motor was conducted to complete the characterization of the motor. Only a discrete-time test was possible since the force transducer signal could only be read by the computer.

Because of the long moment arm in the mounting plate of the force transducer, a structural resonance was introduced and some of the results from the initial tests were corrupted. To attenuate the effect from this resonance, the motor box and mounting plate were clamped to the table as shown in Figure 4-17. This reduced the moment arm, stiffening the spring-like behavior of the mounting plate, and increased

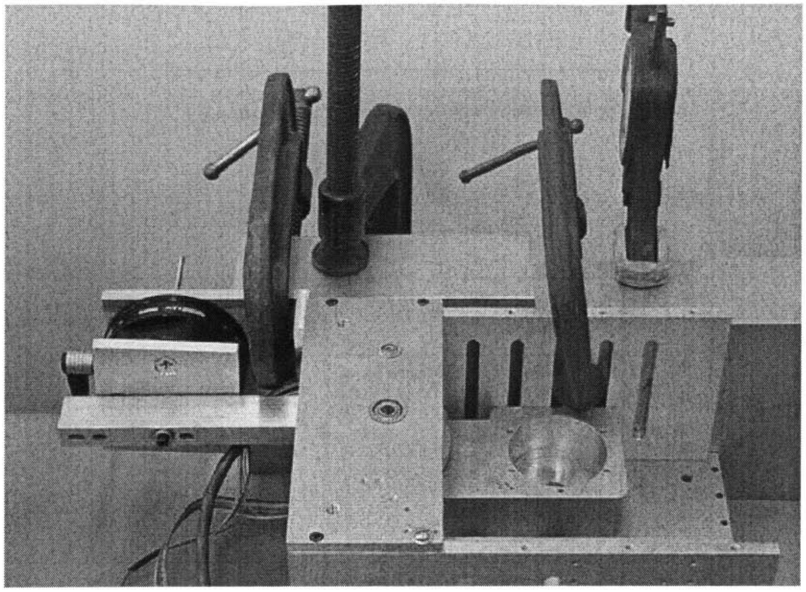

Figure 4-17: Test setup used in the frequency response test of the motor.

the resonant frequency of the apparatus.

Voltage sine waves of varying frequencies were again input to the servo-amp through a D/A channel. The torque from the motor was computed off-line from the force transducer data. As in the discrete-time frequency response tests of the current sensor and servo-amp, magnitude and phase were determined from fitted sinusoids of the torque response and plotted against frequency (see Figure 4-18).

A model was then developed to characterize the dynamics of the motor. The model incorporated the continuous-time model of the servo-amp as well as a first-order roll off with a break frequency of 235 Hz. This was done to account for the low-pass filter built in to the force transducer. The model was converted to the discrete-time domain and compared with the actual data. From Figure 4-19, there seems to be some discrepancy between the model and the data. One possible cause for this is a lingering structural resonance in the test apparatus. In the worst-case scenario, however, the additional magnitude and phase roll off is due strictly from the dynamics of the motor. If this were true, then the motor could only be trusted up to around 150 Hz. Although not ideal, this is still well beyond the bandwidth of the particular application for this robot.

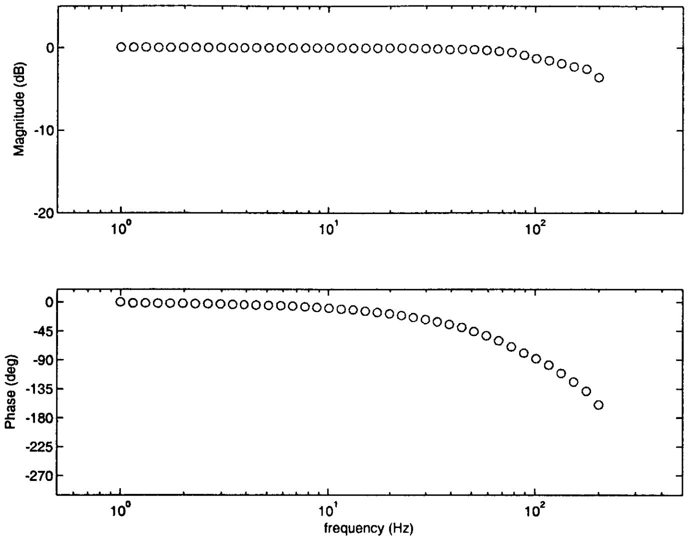

Figure 4-18: Frequency response of the motor in a discrete-time test. Magnitude and phase versus frequency, torque out/current in.

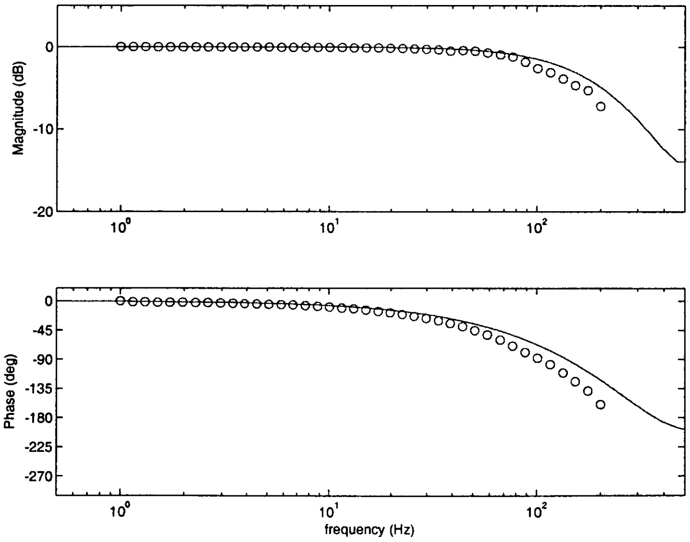

Figure 4-19: Frequency response of the motor in a discrete-time test with fitted model. Magnitude and phase versus frequency, torque out/current in.

4.5 Encoder

The motor has a published peak velocity of 18,000 rpm. However, the discrete nature of the encoder limits the motor from reaching its maximum theoretical speed. Gurley Precision model R119B-01024Q-5L5-A18SY-03MN encoders were chosen for this robot. As a digital device, the encoder can only work in sampled time. The output frequency of this particular model is 300 kHz. Because changes in the encoder signal can only be registered one line at a time, the maximum speed the encoder can record is one line per sample, otherwise the signal will be corrupted. With 5120 lines per revolution after interpolation, this encoder can only measure speeds up to:

$$\omega_{max} = 300,000\frac{\text{lines}}{\text{sec}} \times \frac{1\text{rev}}{5120\text{lines}} \times \frac{60\text{sec}}{1\text{min}} = 3515\text{rpm} \tag{4.4}$$

Although this is much lower than the rated peak velocity of the motor, it is still much higher than the maximum operational velocity of the robot.

4.6 Electrical subsystem conclusions

With the behavior of all the components of the electrical subsystem at least known, if not understood, the limiting factors in the system were revealed. The bandwidth of the motor was limited to around 150 Hz and its peak velocity was found to be slightly greater than 3500 rpm. These performance characteristics are lower than expected but are still well beyond the operational range of the robot.

The next step was to then examine components in the physical system, most importantly components related to the design features of the robot. The transmission design was the main focus of investigation in the work for this thesis and will be the subject of the next chapter.

Chapter 5

Mechanical Subsystem Characterization

This chapter discusses the characterization of the mechanical subsystem of the finger robot. A significant portion of this effort was devoted to investigating the effect of friction in the cable drive. The intent was to determine if the presence of this friction severely compromised the efficiency of the transmission system. The overall goal of the characterization was to parameterize a model for the mechanical dynamics of the robot.

5.1 Subsystem overview

The term mechanical subsystem is used here to refer to the physical components and characteristics of just the robot. It is the recipient of the electrical subsystem output and can be viewed as being part of the "Physical Environment" block in Figure 4-1. To present a clearer picture of the mechanical subsystem, a simple sketch of a finger joint is provided in Figure 5-1.

The pinion gear on the motor drives a larger gear. This tensions one of the two cables which are anchored inside a pulley fastened to the gear. The cables are routed through one or multiple holes (depending on the joint being actuated) and anchored to a block connected to the flexure. The fingers are connected to this block by velcro

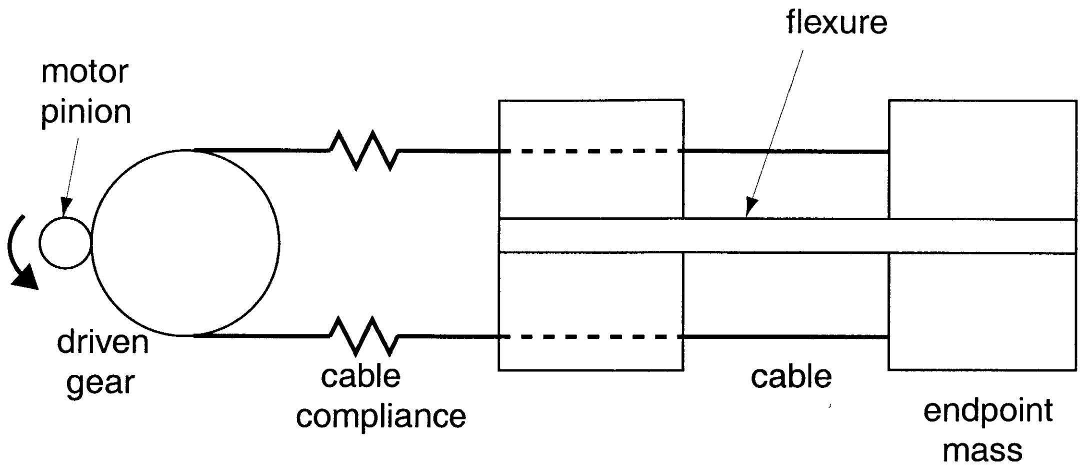

Figure 5-1: Mechanical subsystem diagram. Not to scale.

straps and, in theory, create the kinematic structure that defines the bending path of the flexure. Because cables can only transmit forces in tension, each joint requires a pair of cables for the ability to both push and pull on the finger.

Again for simplicity, the sketch and subsequent models are for one joint only. Like the tests conducted for the electrical subsystem characterization, the tests described in this chapter were performed using the FPIP motor.

5.2 Cable stiffness

The cable used for this robot was series 1050SN manufactured by Sava Industries. It is a 7x19 construction of braided stainless steel wire covered with a nylon coating. To estimate its stiffness, a simple tension test was performed, measuring deflection (or stretch) due to a given load. The test was based on the principles of elementary solid mechanics. The elongation of a uniform bar of length L and cross-sectional area A axially loaded along its centerline is given by the following equation [11]:

$$\delta = \frac{PL}{AE} \tag{5.1}$$

Load (N)	**δ (cm)**	**AE (kN)**
rest	0.0	N/A
44.5	0.3	42.7
89.0	0.6	42.7
133.5	0.85	45.2
178.0	1.05	48.8
222.5	1.3	49.3
rest	0.0	N/A

Table 5.1: Measured elongation of the cable from various axial loads and the calculations for AE from Equation 5.1. Measurements at rest before and after loading are included to show that there was no noticeable plastic strain.

where P is the load and E is its modulus of elasticity (Young's modulus). Stiffness can then be defined simply as:

$$k = \frac{P}{\delta} = \frac{AE}{L} \tag{5.2}$$

meaning that the only factors affecting stiffness are geometry and material properties. The objective of this test, then, was to estimate the value for AE, so that one could calculate the stiffness for any length of cable.

A long, uncut length of cable was tensioned with various known loads and the deflections of a reference line were recorded. Using Equation 5.1, the values for AE were calculated from these measurements. From Table 5.1, one can conclude that the AE of the cable is somewhere around 45 kN.

5.3 Flexure stiffness

The ideal flexure for this robot is one that is pliable in bending but stiff in torsion and buckling. The test described here was intended to estimate the stiffness of the flexure in bending only.

The FPIP actuator was used as the effort source in this experiment. To simplify the experiment and analysis, only one cable was used and, instead of being connected to the intended joint, was anchored to the closest one (FMCP). An open-loop, slow ramp command was issued by the computer. Knowing the gains in the servo-amp

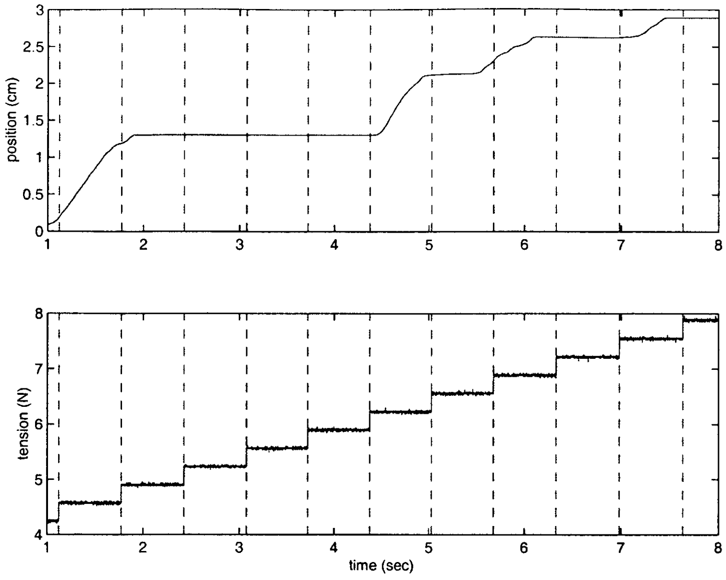

Figure 5-2: Typical data set from a flexure stiffness test. Position of the flexure was calculated from motor angle. Tension force in the cable was calculated from the servo-amp and motor gains. Vertical dashed lines represent changes in command.

and motor and the mechanical ratios of the gear and pulley, the tension in the cable at each sample was known. Similarly, the position of the flexure was determined from the position of the motor. The linear movement of the cable resulted in rotation of the flexure, but linear units were used in the analysis for simplicity.

Figure 5-2 shows a typical data set from one test. There are occasions where the position seems steady over an extended period of time even though the command is changing. This was most likely due to position dependent friction, which will be discussed in more detail later in this chapter.

Tension force was then plotted versus position. However, the samples considered were only those for which the condition for static equilibrium was met (i.e. when velocity was zero), removing transient effects from the data. The stiffness was then estimated as the slope of the best linear fit of this data (see Figure 5-3). 15 trials were performed and the average of all the stiffness values was calculated to be 1.45 $\frac{\mathrm{N}}{\mathrm{cm}}$. The range of all 15 trials was found to be within $\pm 10\%$ of this value, so it was deemed a reasonable estimate.

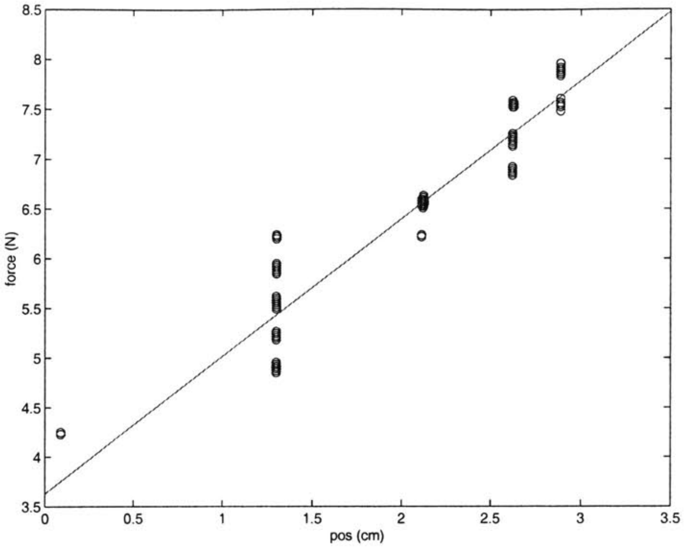

Figure 5-3: Tension force in cable versus position of flexure. Data shown only for when system was in static equilibrium. Slope of the linear fit used as the stiffness measure for each trial.

The method used here is admittedly very coarse. The compliance properties of the flexure may quite possibly be non-linear, but were assumed to be linear for this analysis. In operation, the flexure will bend in a different location depending on the patient's finger length. So a thorough investigation should examine stiffness at various points along the length of the flexure. Although the result from this test may not be entirely accurate, it will be sufficient since an estimate was all that was needed.

Stiffness in torsion was not explicitly tested by experiment. However, the flexures qualitatively seem very weak in that regard. Because of the coaxial joint design, a long moment arm is created in the connection to the fingers. In practice, this may amount to the flexure just twisting about itself and not bending the patient's finger at all. The next design iteration of this robot must include a flexure which is much sturdier in torsion.

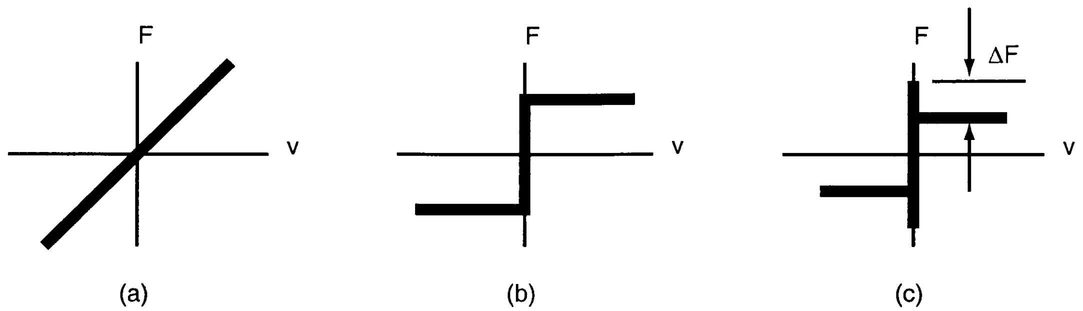

Figure 5-4: **(a)** Viscous friction, normally modelled as linear. **(b)** Coulomb friction. **(c)** Static friction, where $\Delta F > 0$.

5.4 Friction overview

Friction is a force that arises from the relative motion of two bodies in contact. In some cases, its presence can be useful. Braking in a car or any other vehicle, for instance, would not be possible without friction. In other cases, its presence can be detrimental, wearing down parts to the point of catastrophic failure.

But even after decades of focused study, the nature of friction still remains somewhat of a mystery. Models of friction for all types of surfaces, materials, and conditions range from fundamentally simple to grossly complex. The following offers just a brief review of some friction models and studies relevant to the scope and magnitude of this investigation.

5.4.1 Background

In solid-solid contact, friction generally falls under one or more of the following three categories: viscous friction, Coulomb (or sliding) friction, and static friction (or stiction). Figure 5-4 shows the idealized models for these types of friction. Viscous friction is proportional to the relative velocity between the two bodies in contact and is often modelled as linear. Coulomb friction is independent of the magnitude of velocity. Static friction is the force (torque) necessary to initiate motion from rest and is greater than the friction at low velocities. It is believed to be responsible for limit-cycle stick-slip behavior [5, 25].

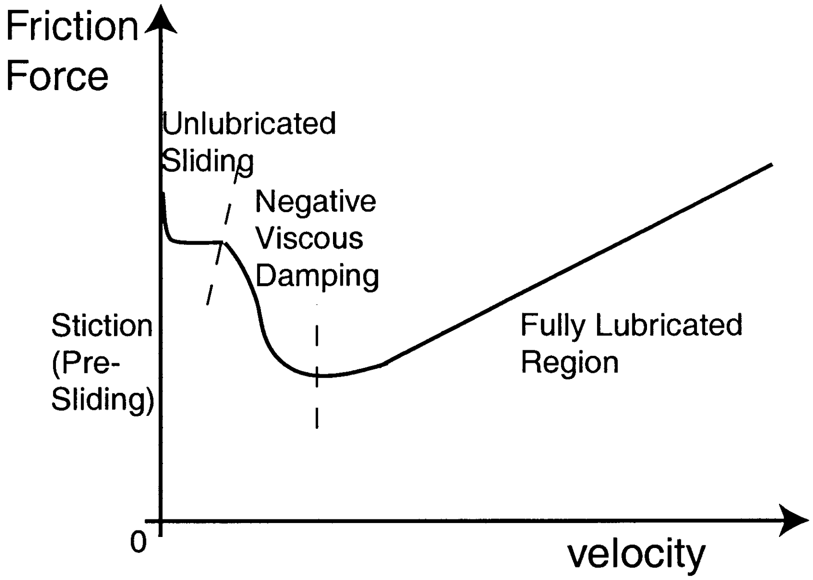

Figure 5-5: Friction force versus relative velocity for two solids in lubricated contact. [8]

Another type of important friction behavior is called the Stribeck effect and can be observed at low velocities. It is a region characterized by negative viscous damping due to partial fluid lubrication [6] (see Figure 5-5). In essence, it is the region that joins the discontinuity between static friction and low-velocity dynamic friction.

Friction also can behave dynamically. It has been observed to vary when there are different normal loads [20], different dwell times [5], and even different velocity histories [13].

With all the parameters and conditions affecting friction, known and unknown, it can be quite a daunting task to model the friction in any system. Intricate experiments and sensitive equipment is necessary to capture its behavior fully. Sometimes, however, a rough model is all that is needed and coarse methods become adequate.

5.4.2 Motivation

To keep frictional losses to a minimum, typical cable drives will employ a system of pulleys and rollers to support the cables so that they are in constant rolling contact. Ideally, only the friction in the bearings would be present. A pulley-based tendon system was chosen for the design of the Utah/MIT Dextrous Hand over other lubricated tendon structures simply because of its low-friction properties [15]. In reality, slipping still occurs in the cable-pulley interaction and may cause Coulomb-like friction [6, 25]. But it is likely to still be orders of magnitude less than that in a pure sliding interaction.

The design for this robot departs from convention in that the cables are supported only by the holes through which they are routed. Friction from the sliding interaction between the cable and the holes undoubtedly results and is expected to vary as the cable comes out at different angles. The purpose of this study was to measure friction as a function of the exit angle of the cable and to determine the feasibility of hole supports as a design feature. Given that the motor box eventually would be redesigned, a meticulous study was not warranted. Just capturing the general trend in friction was all that was necessary.

5.4.3 Test setup

To measure the amount of friction in the transmission, a test bed was custom-designed and machined (see Figure 5-6). A rigid platform was made on which the finger motor box could sit so that the cable was perpendicular to the ground. The back plate of the platform, which fastened to a block clamped to a table, had slotted holes for the bolts. This allowed the platform to rotate between 0° and 45° relative to the ground.

One cable was connected to the pulley of the FPIP motor in an open-circuit configuration, that is, the cable was under tension only when the drive transmitted a load between input and output. It was routed through one hole in the side of the motor box and a weight of known mass was hung from its end. Rotating the motor box on the test platform thus changed the exit angle of the cable since the force of gravity always pointed the weight in the same direction, vertically downward. To demonstrate this concept, Figure 5-7 shows the platform at a zero and non-zero angle.

The estimate of friction was calculated by an equation derived from the free-body diagram of the weight, shown in Figure 5-8:

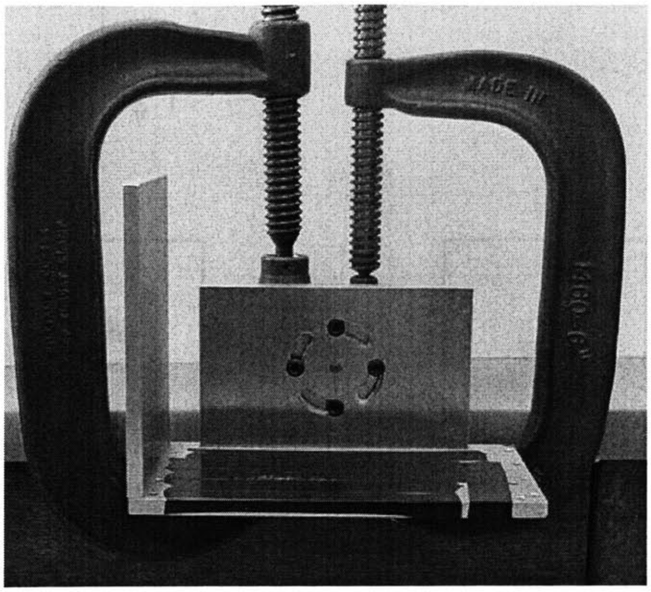

Figure 5-6: Custom-built test platform used for friction tests.

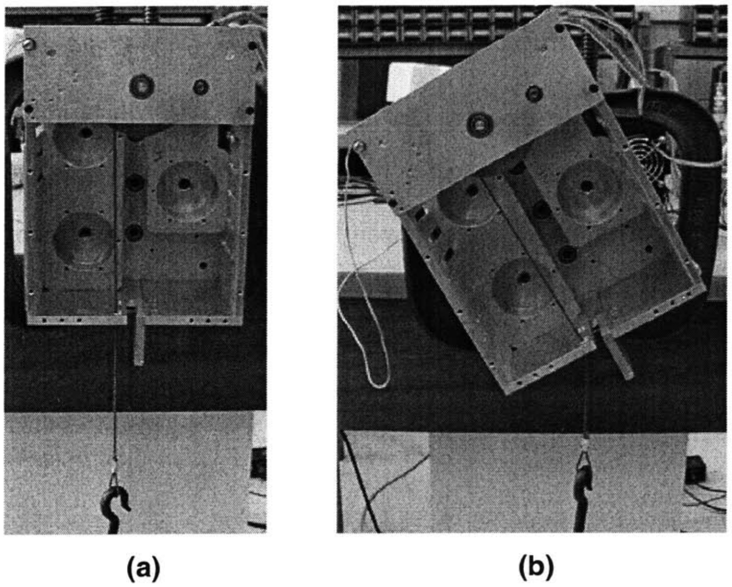

(a) **(b)**

Figure 5-7: **(a)** Friction test setup with platform at 0°. **(b)** Friction test setup with platform tilted at a positive angle.

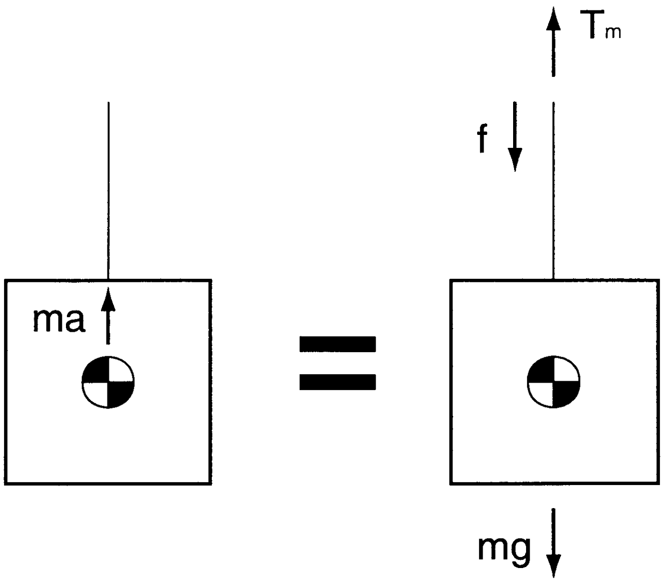

Figure 5-8: The free-body diagram of the weight used in the friction test. Tests were done at rest or constant velocity ($a = 0$), so the friction force was calculated simply as $f = T_m - mg$.

$$ma = T_m - f - mg \tag{5.3}$$

where positive motion is defined as against gravity.

The tension in the cable due to the motor, T_m, was derived from the gains in the system, similar to what was done for the flexure stiffness tests. The force due to gravity was constant and known from weighing the mass on a simple kitchen scale ($mg = 6.4$ N). During the tests, the weight was at a state of zero acceleration, either at rest or at constant velocity. Setting $ma = 0$ and simply rearranging Equation 5.3, the friction force could be derived as:

$$f = T_m - mg \tag{5.4}$$

Tests were performed with the motor box on the test platform tilted at 0°, 15°, 30°, and 45°. Separate tests were also conducted to measure the friction in the motor and its bearings, as well as friction in the gear train.

5.5 Static friction

Static friction is also referred to as the breakaway torque (or force), as it is the effort required to break the bonds formed when bodies contact each other at rest. It is expected and has been demonstrated to be a position-dependent phenomenon [5]. The tests described here were designed to obtain a "ballpark" figure for static friction so did not thoroughly investigate its position dependence, although it was observed.

5.5.1 Method

The motor box was set on the platform at the specified angle of the test. To measure static friction in the positive direction, a slow ramp of torque with a positive slope was commanded to the motor by a D/A channel on the computer. The weight was released and moved vertically downward until the motor command was enough to counter the force of gravity. The weight remained at rest while the command continued to increase to overcome static friction. Once static friction was broken, the weight began to travel upward until the end of the test.

The measure of static friction in the negative direction was done in a similar manner. An initial positive command was given and was ramped slowly with a negative slope. Once released, the weight moved upward until the command balanced the force of gravity. It then remained at rest until static friction was broken and then moved downward until the end of the test.

The last sample of zero velocity was chosen as the time when static friction was broken. T_m was recorded at this sample and the static friction was calculated using Equation 5.4. A test for static friction in the gear was also performed. The setup was similar to the 0° test except that the side plate was removed from the motor box to eliminate the cable-hole interaction. To avoid cutting the cable to remove the plate from the assembly entirely, it was simply slid down to the bottom of the cable and added to the mass of the weight.

For the static friction test of the motor, the gear was removed from the assembly and the motor was considered to be unloaded. Positive and negative ramps were

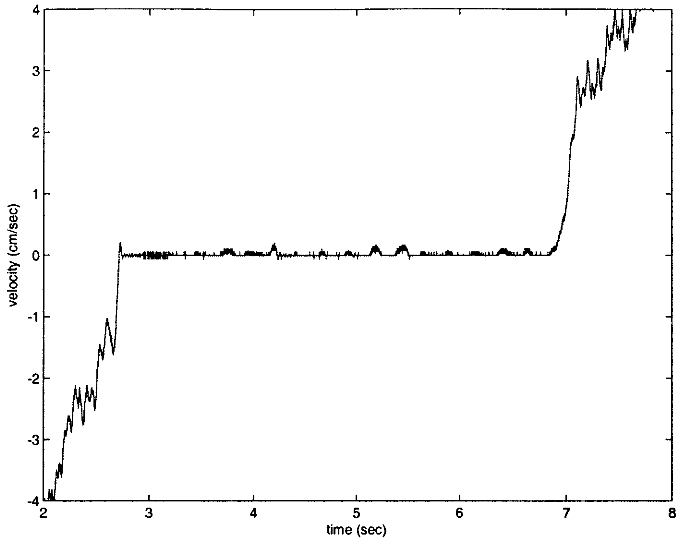

Figure 5-9: Typical velocity profile from a static friction test for the positive direction.

commanded and the same criterion was used for breakaway (last sample at zero velocity). The torques required to break static friction were converted to equivalent tension in the cable for easier comparison.

20 trials were performed under each condition in both positive and negative directions. The resolution of the 12-bit D/A made it only possible to command tension in the cable in increments of 0.332 N.

5.5.2 Analysis and discussion

Stick-slip behavior

During the time when the forces on the weight were balanced and before static friction was broken, the weight was not always at rest. A plot of the velocity profile of a typical trial shows that there are many occasions when velocity is non-zero (see Figure 5-9). So the weight during these tests was not fully at a resting condition but was moving in stick-slip fashion. The cause of stick-slip behavior is believed to be compliance in the bonds formed during solid-solid contact [5]. A separate test of this system showed that there was indeed compliance somewhere upstream of the cable-hole interaction.

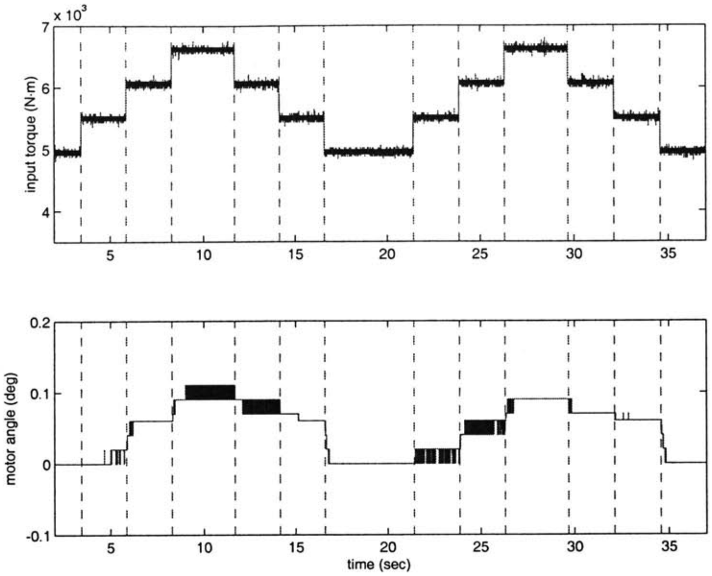

Figure 5-10: Typical position response of motor-gear assembly while in the static friction regime. The dotted vertical lines represent changes in input command.

The motor box was set up in the gear test configuration (0° with the side plate removed). The command to the motor was a low frequency triangle wave with a mean value and amplitude such that the system was always in the static friction regime. This test was performed several times and the position response for each trial was similar. As Figure 5-10 shows, the position response follows the command in a spring-like manner, reaching equilibrium after some initial transient. The source of this behavior may be from compliance in the motor shaft, in the gear shaft, or in the actual gear teeth. The origin of the compliance is not important for this investigation, but establishing its presence accounts for the stick-slip behavior in these tests.

Effect due to exit angle

The static friction measure from each trial was plotted in a histogram for that particular test. The bins of the histogram were centered on consecutive increments of force due to the resolution of the D/A channel. Figures 5-11 and 5-12 show the distributions of the data.

The mean static friction for each condition was then calculated. Table 5.2 shows

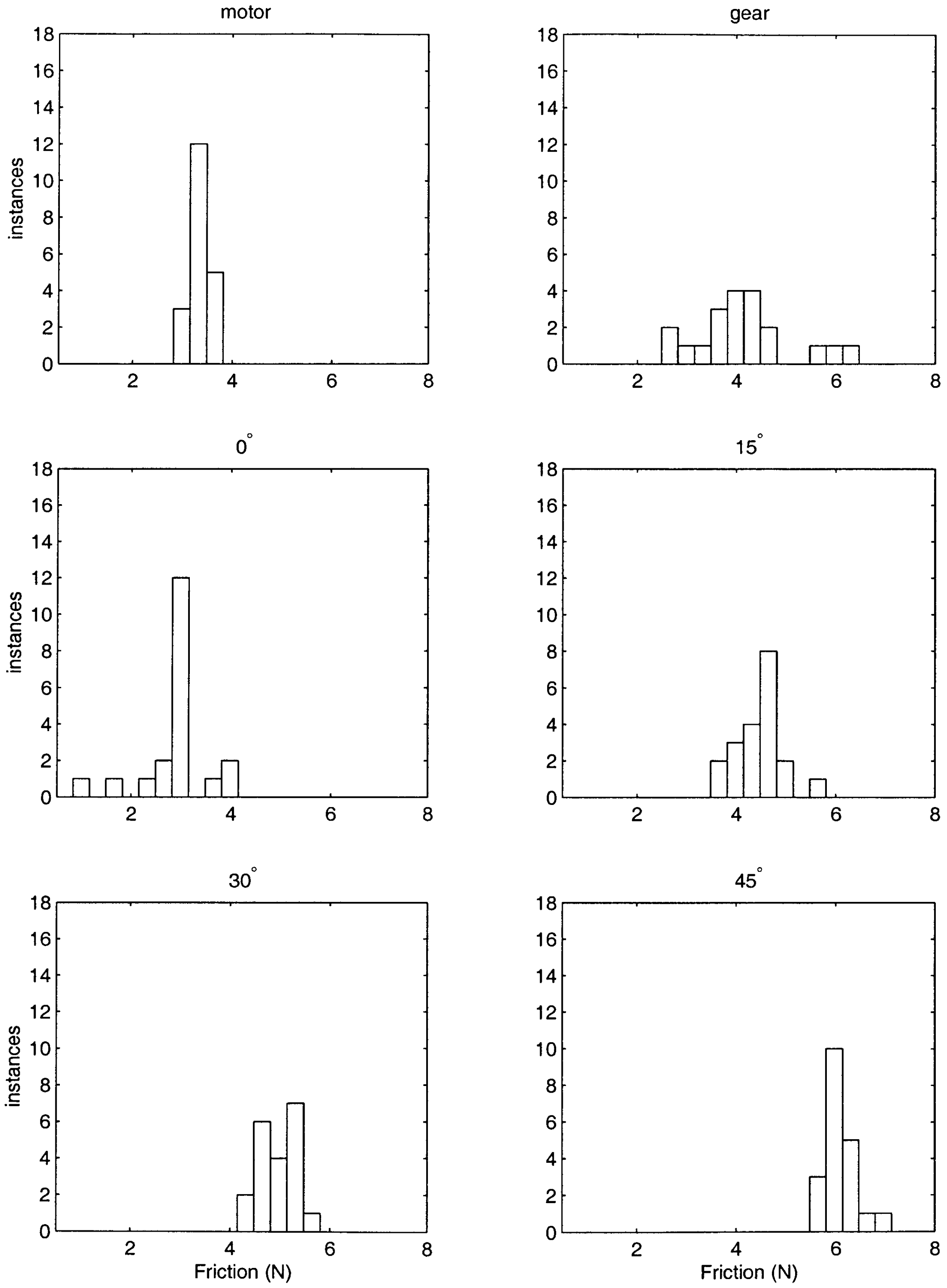

Figure 5-11: Distribution of static friction in the positive direction for each test condition.

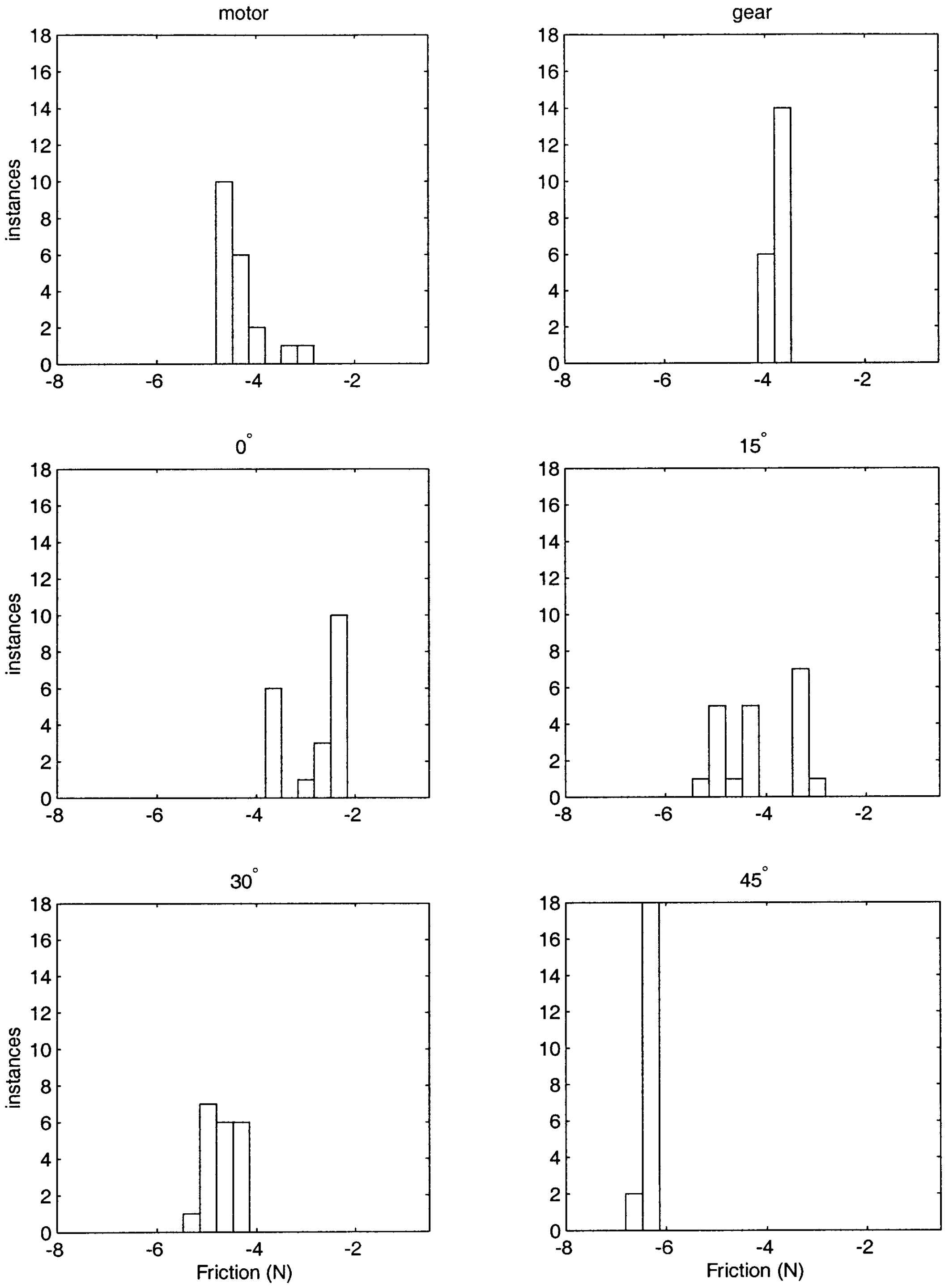

Figure 5-12: Equivalent of Figure 5-11 for negative direction.

test condition	Δf_s **positive**	Δf_s **negative**
motor	3.29	-4.40
gear	0.97	**0.76**
0°	**-1.50**	**0.71**
15°	1.56	-1.33
30°	0.51	-0.53
45°	1.16	-1.66

Table 5.2: Contribution to static friction in each direction from each test condition. Observations with unexpected signs are bold-faced. All values given in Newtons.

the contribution to friction from each test condition. This was determined by taking the mean friction of the particular test and subtracting the mean friction from the previous condition. As expected, static friction, f_s, seems to increase in magnitude as exit angle increases. However, for three observations (shown in bold), the addition of a new source of friction seems to reduce the friction force. This is most likely not a real phenomenon and is just an artifact of inaccurate measures of the different loads encountered in the motor and gear tests. What is most important is the trend due to varying exit angles. The motor and gear tests are merely meant to demonstrate order of magnitude.

Position dependence

In some histograms, a bimodal distribution can be clearly observed, for instance in the 0° exit angle test in the negative direction. Looking at the position data for this test, the six trials with higher static friction values all enter the static friction regime at around the same position. The same is true for the other 14 trials, shown in Figure 5-13.

The difference in these positions is close to the separation between teeth on the pinion gear (25.7°). So, it is likely that, in the course of the 20 trials, the motor settled in only two different gear teeth and the bi-modal nature of the static friction data is due to position dependence.

Figure 5-13 also shows that the position profiles are remarkably repeatable, espe-

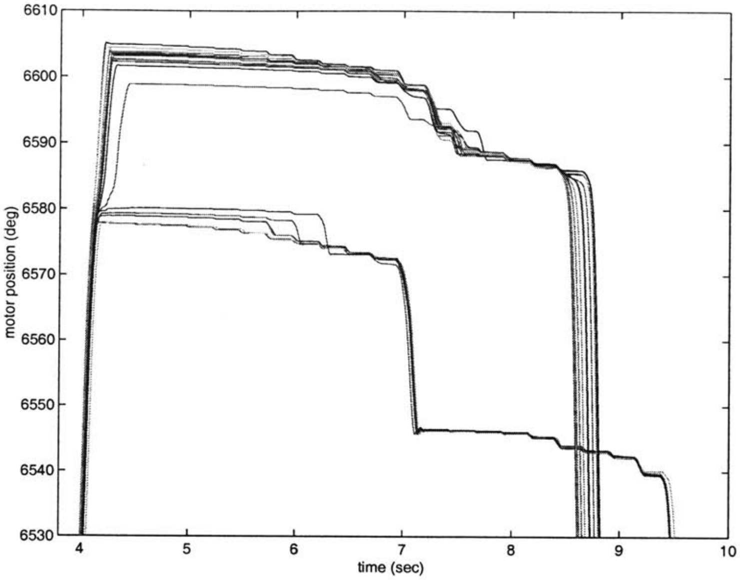

Figure 5-13: Position profiles of all the trials performed for the 0°, negative direction test. Separation between the two positions of initial rest is close to the angle between gear teeth.

cially as the weight is about to break static friction. This suggests position dependency in friction as well.

Another source of position dependency was revealed in a separate test. With the gear removed from the assembly and the motor unloaded, a sine wave command was issued to the motor. The mean and amplitude of the wave were chosen such that the motor would come to rest and then break static friction every period, as shown in Figure 5-14.

After the absolute position data was converted to relative angle within the motor, the average position when the velocity was zero in each period was calculated. A histogram of these angles reveals that they are distributed into distinct and separate locations. Figure 5-15 shows that these regions are each separated by about 45°, the separation between motor poles. This suggests that cogging plays a role in the position dependency of static friction.

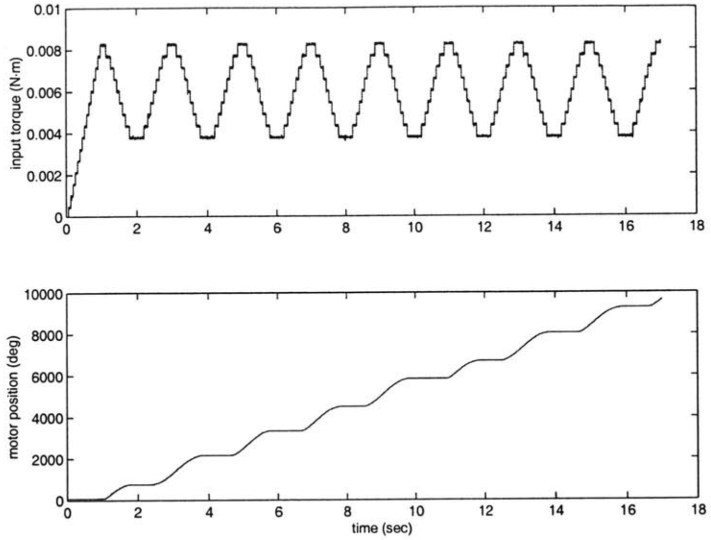

Figure 5-14: Typical command profile to periodically break static friction in the motor and the resulting motor position.

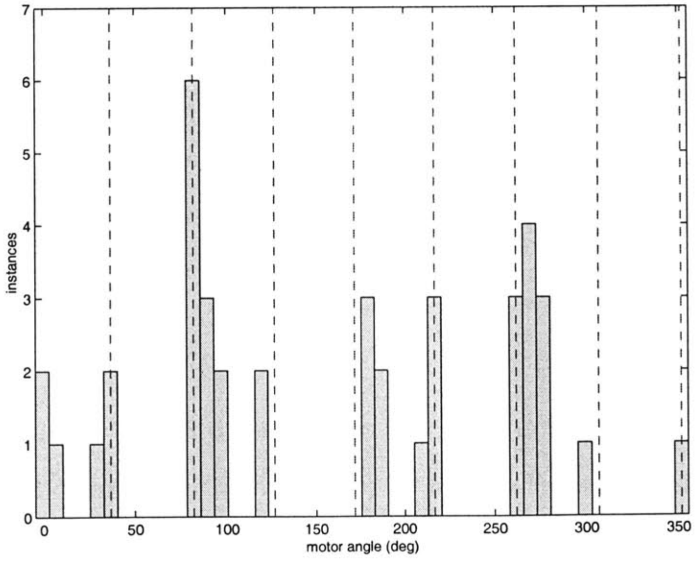

Figure 5-15: Histogram of average motor positions at breakaway. The dotted vertical lines are spaced 45° apart.

5.6 Dynamic friction

Dynamic friction refers to friction at non-zero velocity. Often times its effects are weakened by introducing a dry or wet lubricant into the interaction. The tests described here did not include any lubricants, nor were any specified in the design. This may, however, be an idea employed in future iterations to increase transmission efficiency.

5.6.1 Method

To estimate friction using Equation 5.4, the sum of the forces on the weight must be zero. So for these non-zero velocity tests, the velocity was simply held constant within each trial. To accomplish this, a closed-loop PD controller was implemented. The desired velocity was ramped to the appropriate trial velocity and then held constant. The desired position was simply the integral of the desired velocity. Again, for consistency, all units were converted into the linear domain of travel for the cable. A proportional gain (K) of 115 $\frac{\mathrm{N}}{\mathrm{cm}}$ and a derivative gain (B) of 11.5 $\frac{\mathrm{N{\cdot}s}}{\mathrm{cm}}$ were used for all the trials.

The gear and motor tests were conducted in the same manner and under the same load conditions as their static friction tests.

Because of the position dependency of friction, only the data from within a particular position window was analyzed. Exceptions to this rule came at low velocities, where the weight did not travel through the entire position window.

5.6.2 Analysis and discussion

Frequency content

The velocity and command profiles held a fair degree of noise, as shown in Figure 5-16. The velocity data typically ranged within about eight bits of resolution so it was said to be near constant, allowing the use of Equation 5.4.

FFT analysis provided a better picture of the frequency content in the data. Six

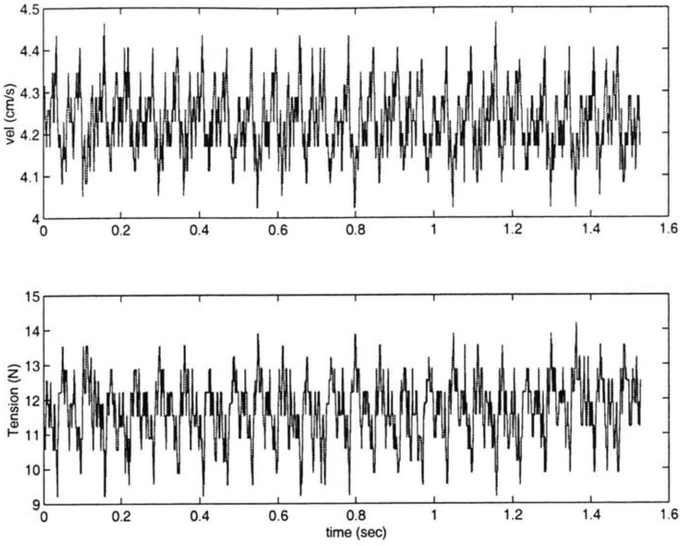

Figure 5-16: Typical velocity and command profiles for the dynamic friction tests.

noticeable frequency spikes appeared in the velocity and command data of every trial. These frequencies were also directly proportional to the speed of the motor, as shown in Figure 5-17. The spikes appeared at x, $4x$, $8x$, $16x$, $24x$, and $27x$ hertz, where x is the speed of the motor in revolutions per second.

The x hertz spike was most likely due to the eccentric spin of the motor shaft. The $4x$ and $8x$ hertz spikes were probably due to torque ripple (4 and 8 being the number of pole pairs and motor poles respectively). The $16x$ and $24x$ hertz spikes could simply be from the harmonics of the $8x$ spikes. No explanation has been proposed for the $27x$ spike, but is probably only of academic interest and would not be a reason to discount the data. It should be noted that the $8x$ spike was always the most prominent, indicating that torque ripple in the motor affected its performance.

Effect due to exit angle

The mean of the friction data for each trial was plotted against the nominal velocity. A $\pm 1.68\sigma$ error bar was included as an indication of variance. Data from the static friction tests were also included. Figure 5-18 shows the friction plots for each test

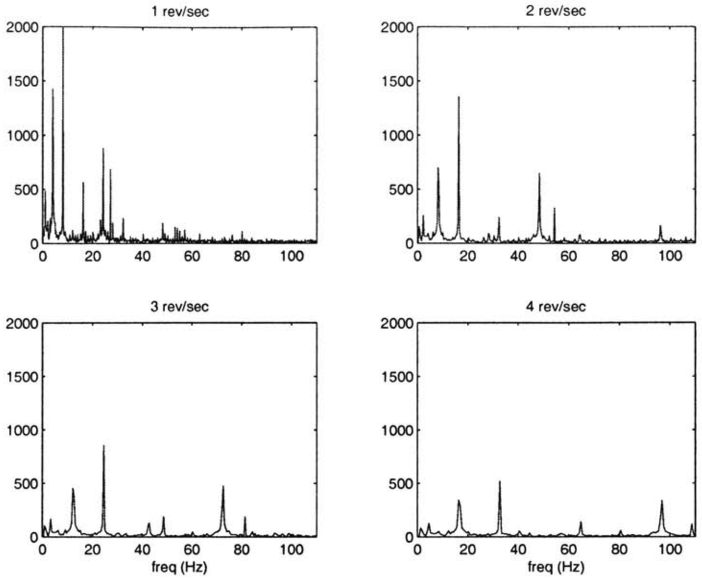

Figure 5-17: Typical FFT of velocity and command data from the dynamic friction tests. Spikes in frequency are proportional to speed of the motor. Power reading tends to lower as speed increases because data contains fewer samples.

condition overlaid. For clarity, the error bars were omitted. The individual plots are given in Appendix D.

The curves in the positive velocity half seem quite well behaved. Looking closely, one can detect a negative slope at low velocity. Except for the motor and 30° test, all the other tests showed a progressive decrease in mean friction from trial 1 (the slowest velocity) to trial 3. Knowing the means and standard deviations and assuming that all the measurements were distributed normally within each trial, the probability that a friction measure from trial 1 was greater than the mean of trial 3 ranged between 55% and 62% for these tests. This presents strong evidence for the presence of the Stribeck effect. With a more exact method, the evidence may become even more convincing.

Although there are clear trends, the negative velocity half of the plot does not seem quite as well behaved as its counterpart. A consistent nonlinearity appears between -5 and -10 $\frac{\text{cm}}{\text{sec}}$. It was first proposed that this may be an effect of adding the gear. However, a test was performed with the cable detached from the pulley and

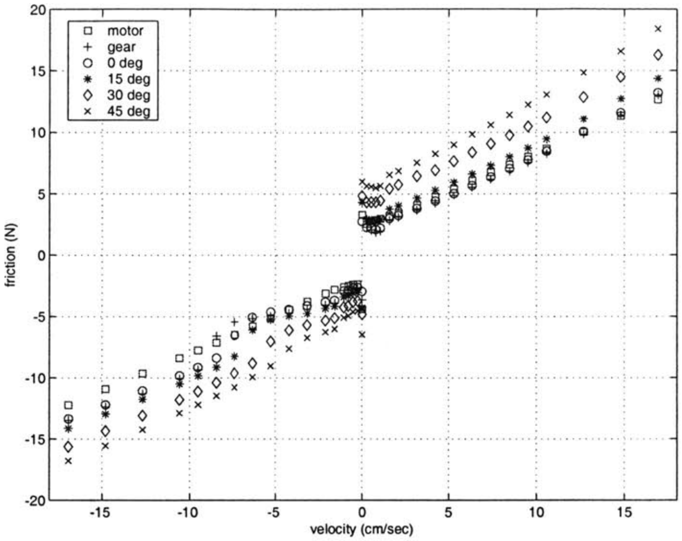

Figure 5-18: Friction data for all cable exit angles, means only.

the gear unloaded and the curve was as smooth as that for the motor. It was also suspected that the anomaly may be a result of the weight entering free fall. However, the acceleration of the weight to reach its test speed never reached that of free fall. Whatever the reason, it is rather peculiar that this effect is only seen in the negative velocity region, with no trace of it in the positive. It is also interesting to note that the effect seems to disappear as the exit angle is increased. Because this study was meant to examine general trends, further investigation has been postponed and the effect was essentially ignored.

Friction model

A simple model of the friction in the system was then developed. The model consisted of only Coulomb and linear viscous friction elements. The means in the exit angle tests were subtracted by those from the gear test to isolate the friction in the cable-hole interaction, as shown in Figure 5-19. The effect of the presence of the gear was determined by subtracting the contribution from the motor. For each test condition, the means from the positive velocity tests were joined with a linear fit. The intercept

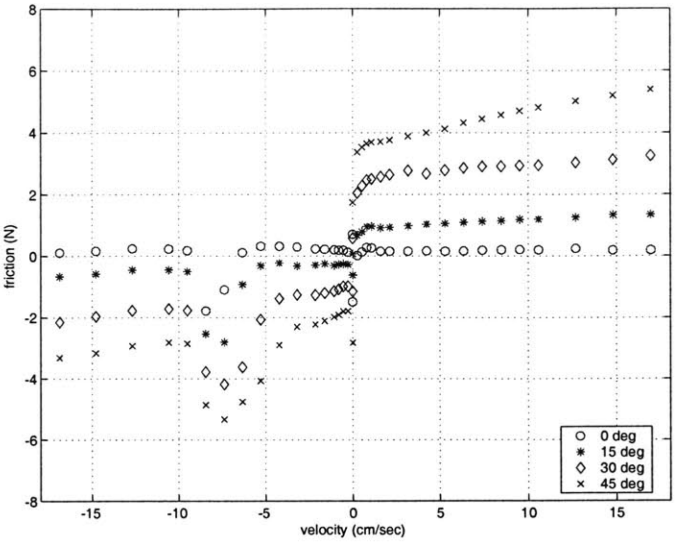

Figure 5-19: Calculated friction from just the cable-hole interaction.

was used as the Coulomb friction term (f_{c+}) and the slope was used as the viscous friction term (f_{v+}). The same was done for the negative velocity tests, except that four points in the nonlinear region were omitted from the fitting. The Coulomb and viscous friction terms in this region are denoted as f_{c-} and f_{v-} respectively. The following piecewise equation was then used as the friction model:

$$f(\dot{x}) = \begin{cases} f_{c+} + f_{v+}\dot{x} & \text{for } v > 0 \\ f_{c-} + f_{v-}\dot{x} & \text{for } v < 0 \end{cases} \tag{5.5}$$

test condition	f_{c+} [N]	f_{v+} [$\frac{\text{N·s}}{\text{cm}}$]	f_{c-} [N]	f_{v-} [$\frac{\text{N·s}}{\text{cm}}$]
motor	2.30	0.60	-1.97	0.61
gear	**-0.74**	0.05	-0.54	0.07
0°	0.16	0.003	**0.22**	0.002
15°	0.86	0.03	-0.24	0.02
30°	2.42	0.05	-1.05	0.06
45°	3.51	0.12	-1.97	0.08

Table 5.3: Contribution to Coulomb and viscous friction at each test condition, derived from linear fits to the data. Observations with unexpected signs are bold-faced.

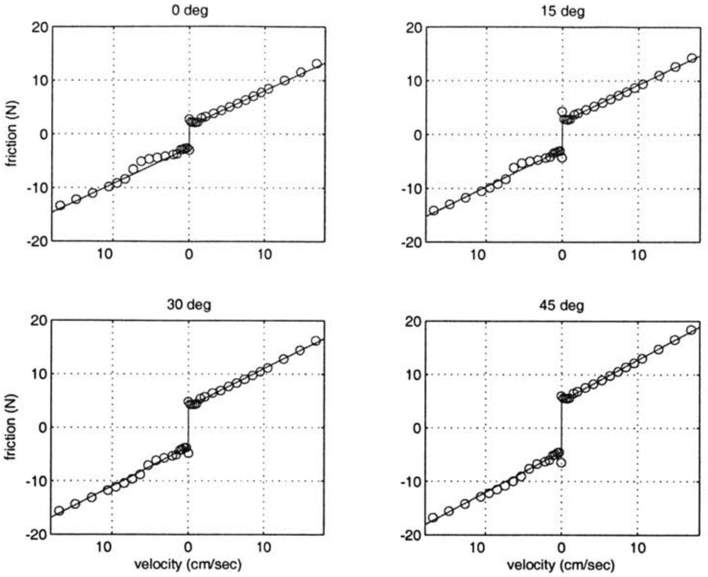

Figure 5-20: Friction model at various exit angles overlaid with data from experiments.

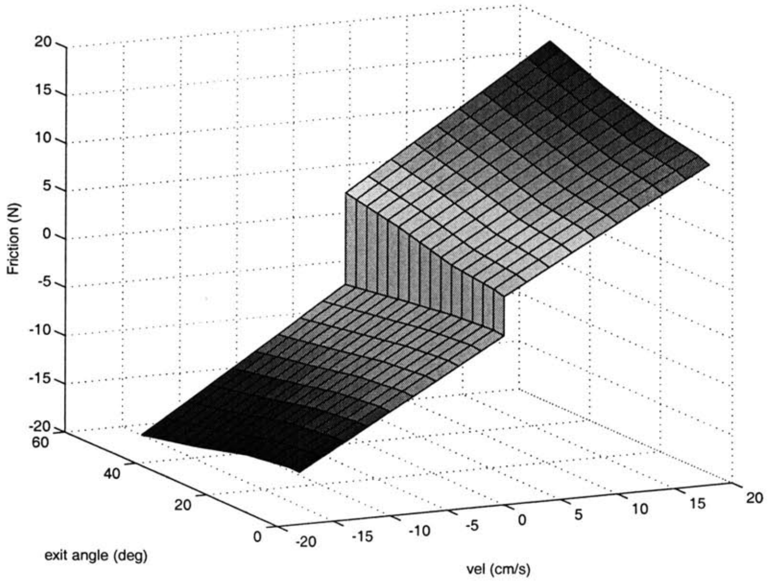

Figure 5-21: Friction model as a function of velocity and exit angle.

Table 5.3 shows the values of the friction parameters derived from these fits and shows how they vary with exit angle. The unexpected signs for two observations in bold, again, are most likely due to error in the coarse method used rather than to real, physical behavior. However, there is a clear trend showing steady increases in magnitude in Coulomb friction with increasing exit angle. Viscous friction also increases but not as significantly. The model of gear friction was composed of Coulomb and viscous friction elements and was determined with linear fits as well.

The model of the gear friction was then added to that of the cable friction for each exit angle. These models were then compared with the data and, as seen in Figure 5-20, were found to be quite close. The parameters were then linearly interpolated between exit angles and the full model of friction was complete, seen in Figure 5-21.

5.7 Mechanical subsystem conclusions

The tests used to determine friction forces were rather imprecise compared to those used in most mainstream friction studies. However, the goal of these tests was simply to determine reasonable estimates and general trends of the friction in the transmission system of this robot.

The results have shown that friction is position dependent and quite repeatable. Static and Coulomb friction both increase significantly with exit angle while viscous friction increases only slightly. However, the magnitude of friction due to the cable-hole interaction is at worst comparable to that in the rest of the transmission. The maximum friction force measured was found to be around 18 N with about 13 N coming from the motor, bearings, and gear interactions. The maximum force desired for any one joint is 50 N [16]. With the rated continuous torque of the motor able to transmit 230 N of tension in the cable, there is more than enough power to overcome frictional forces in the transmission, even with multiple cable-hole interactions.

The trouble then becomes compensating for the friction with an efficient control algorithm.

Chapter 6

Controls Study

With key components of the robot characterized, a preliminary controls study could be performed. This chapter begins by presenting the model used for the experiments and analysis. It then examines several control algorithms, adjusting the model along the way. All the experiments described here were performed in the uncoupled state, without human interaction.

6.1 System model

To keep conditions similar to those in the mechanical subsystem characterization tests, the FPIP motor was connected to the bottom half of the FMCP joint. Again, the transmission employed an open-circuit configuration rather than the intended closed-circuit, meaning that only one cable connected the joint to the motor. The endpoint of the cable was assumed to travel in linear units, as was done in the analysis for the flexure stiffness test.

Knowing the magnitude of forces to be used in the experiments, the stretch in the cable was calculated from Equation 5.1. It was found that any elongation of the cable in these tests would be undetectable by the encoders, so cable stiffness was not included in the model. The transmission is thus approximated as rigid.

A simple model was constructed with all components modeled in the linear domain, as shown in Figure 6-1. The input effort to the system (u) is tension in the

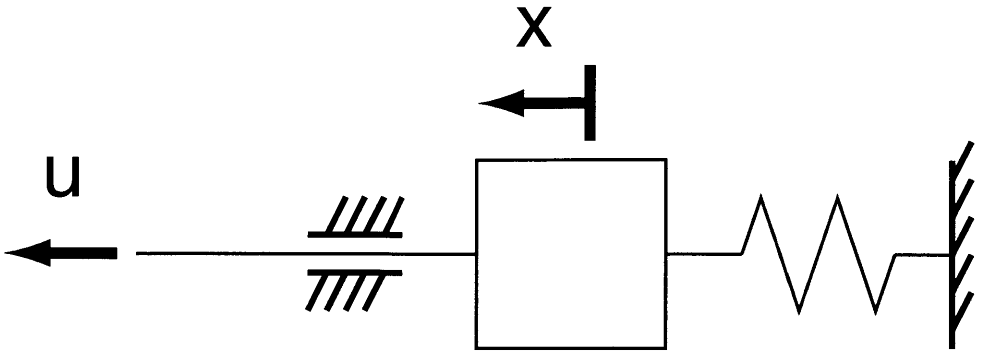

Figure 6-1: Mechanical model of FMCP joint.

cable created by the motor. Some power is subsequently lost from the grounded friction element. The cable then moves a mass, m, which is connected to a grounded linear spring, with stiffness k. Using elementary Newtonian analysis, the following equation of motion results:

$$m\ddot{x} = u - f(\dot{x}) - kx \tag{6.1}$$

where x is the absolute position of the mass (positive defined in the direction of cable pull) and $f(\dot{x})$ is the friction force, modeled by the Coulomb and viscous friction model derived in Chapter 5. The estimate for flexure stiffness found in Chapter 5 was used as the linear stiffness value k.

It was observed that significant displacement of the joint via tension in the cable did not cause a significant change in exit angle of the cable. So, in a further simplification, the friction term was constrained to the 0° friction curve. This was just a fortunate coincidence, however, because the cables joined to the FPIP joint and the top half of the FMCP joint will indeed change in exit angle as their respective joints move under tension.

parameter	initial	adjusted	Δ	units
k	1.45	1.70	+0.25	$\frac{\text{N}}{\text{cm}}$
f_{c+}	1.716	2.81	+1.094	N
f_{c-}	-2.284	-3.37	-1.086	N
f_{v+}	0.656	0.67	+0.014	$\frac{\text{N}\cdot\text{s}}{\text{cm}}$
f_{v-}	0.676	0.69	+0.014	$\frac{\text{N}\cdot\text{s}}{\text{cm}}$

Table 6.1: Initial and adjusted model parameters for the open-loop response test.

6.2 Open-loop response

6.2.1 Validating parameters

To test the accuracy of the parameters used in the model, an open-loop experiment was conducted. In separate tests, the motor was given a positive step command and a sine wave command. The sine wave was offset such that the motor was always given a non-negative command, that is, so that the cable would never have to push. Figures 6-2 and 6-3 show the results from the tests compared with simulated model responses. It is evident that these models did not predict the behavior entirely accurately.

The model was then adjusted to better fit the data and the results are shown in Figures 6-4 and 6-5. The results from three experiments are overlaid to demonstrate repeatability. Table 6.1 shows the model parameters before and after the adjustment. The large changes in Coulomb and viscous friction are possibly due to damping in the flexure itself. In the mechanical model of Figure 6-1, this is equivalent to a damper inserted in parallel with the spring.

Although not the best fits (especially for the sine wave response), the model response is better than before and is adequate for the purposes of this investigation. It is also about as close as can be expected with such a gross model of the system.

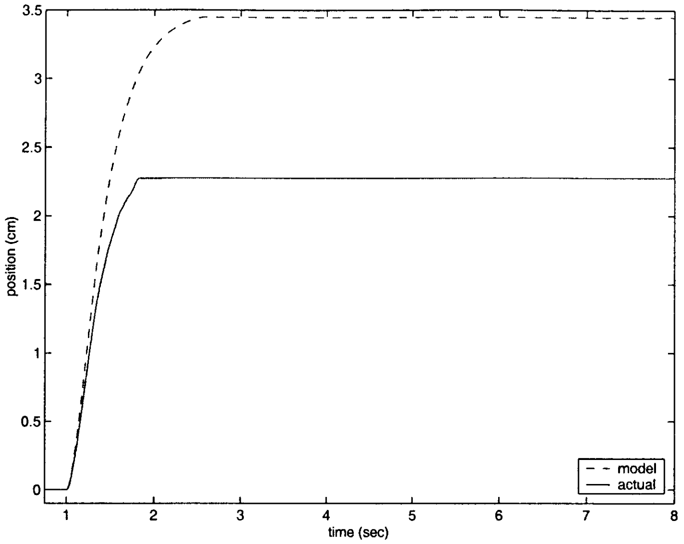

Figure 6-2: Position response to open-loop step command plotted with simulated model response.

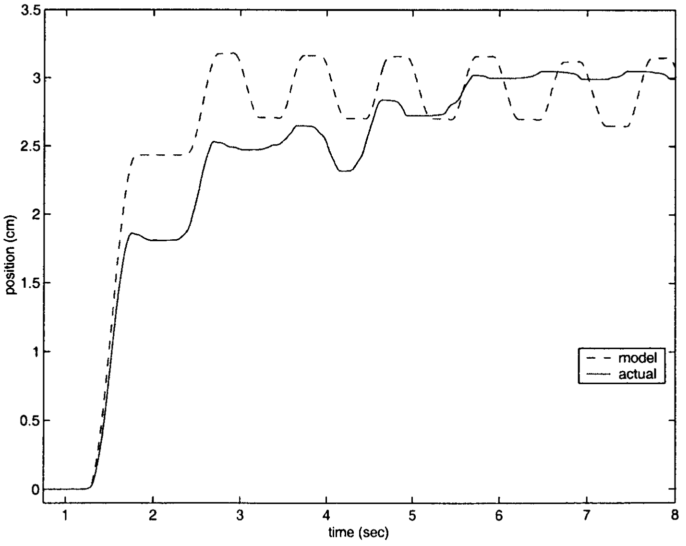

Figure 6-3: Position response to open-loop sine-wave command plotted with simulated model response.

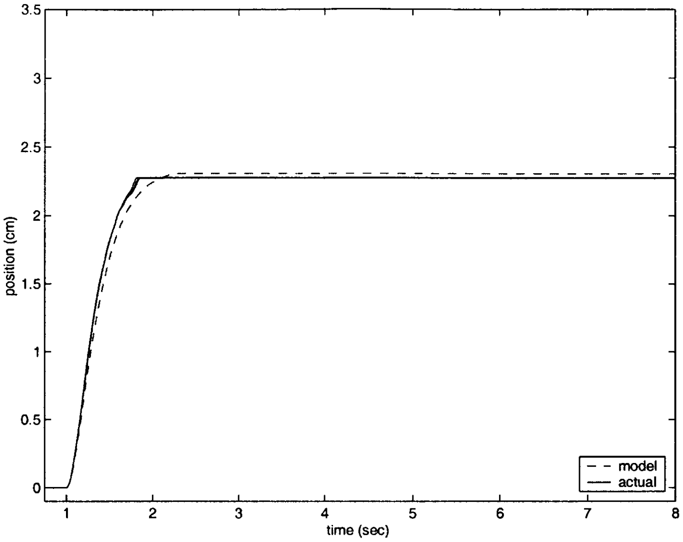

Figure 6-4: Position response to open-loop step command plotted with simulated response of adjusted model.

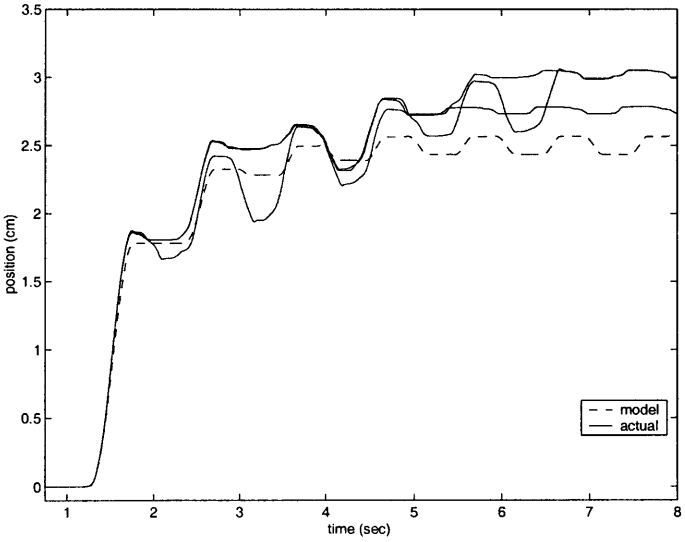

Figure 6-5: Position response to open-loop sine-wave command plotted with simulated response of adjusted model.

parameter	initial	adjusted	adjusted(2)	units
k	1.45	1.70	1.45	$\frac{\text{N}}{\text{cm}}$
f_{c+}	1.716	2.81	2.62	N
f_{c-}	-2.284	-3.37	-3.45	N
f_{v+}	0.656	0.67	0.66	$\frac{\text{N}\cdot\text{s}}{\text{cm}}$
f_{v-}	0.676	0.69	0.68	$\frac{\text{N}\cdot\text{s}}{\text{cm}}$

Table 6.2: Model parameters used for the open-loop trajectory response test. Part of Table 6.1 is included for comparison.

6.2.2 Trajectory response

The response of the system following a desired trajectory in open-loop was then examined. Knowing the dynamics of the system, the motor was commanded to track a trajectory, $x_d(t)$, under the following control law:

$$u = m\ddot{x}_d + f(\dot{x}_d) + kx_d \tag{6.2}$$

$x_d(t)$ in this experiment was an offset sine wave. m was simply estimated by measuring the weight of the joint (removed from the assembly) on a kitchen scale. Trials were conducted using both the initial and adjusted parameters for f and k.

Figure 6-6 shows the response of the system using the original parameters. Because the model does not account for the damping in the flexure, it is no surprise that the response is poor. Figure 6-7 shows the response using the adjusted friction and stiffness parameters. In this case, it seems that the model has overcompensated.

It is not uncommon in friction experiments to redefine parameters for a specific motion [5]. So, the parameters were adjusted once more and the response is shown in Figure 6-8. As expected, the position tracks better than the previous two. The step-like trends are due to the position dependency of friction. The difference in position is consistent with the spacing between gear teeth and motor poles. Table 6.2 shows the new parameters.

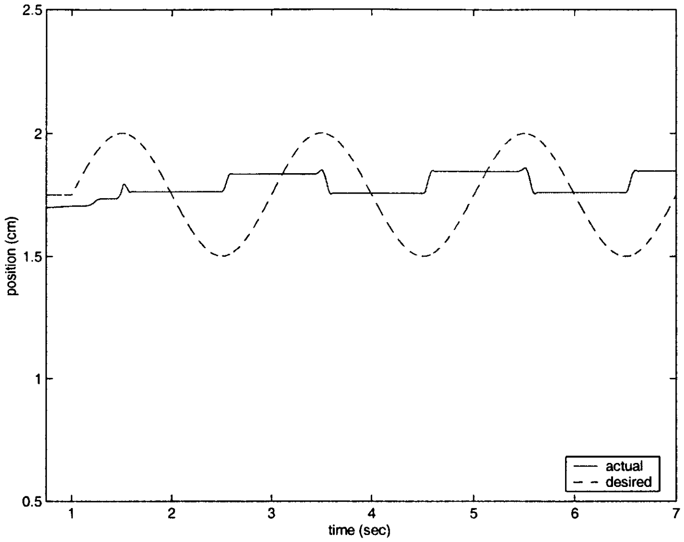

Figure 6-6: Position response to an open-loop trajectory command using initial model.

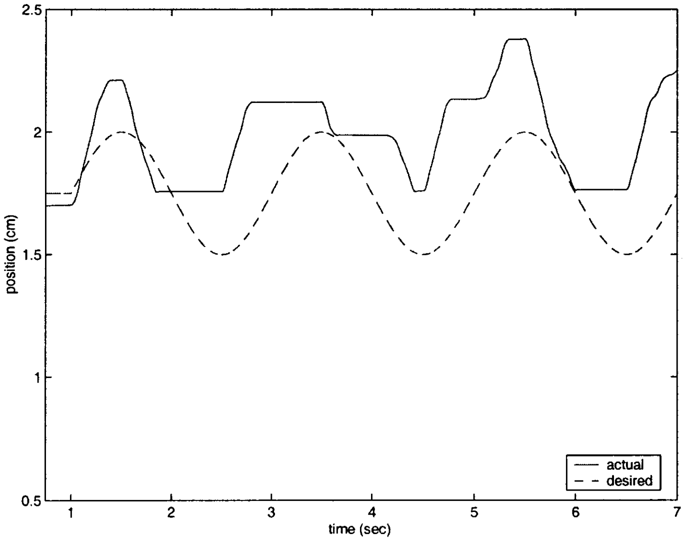

Figure 6-7: Position response to an open-loop trajectory command using adjusted model.

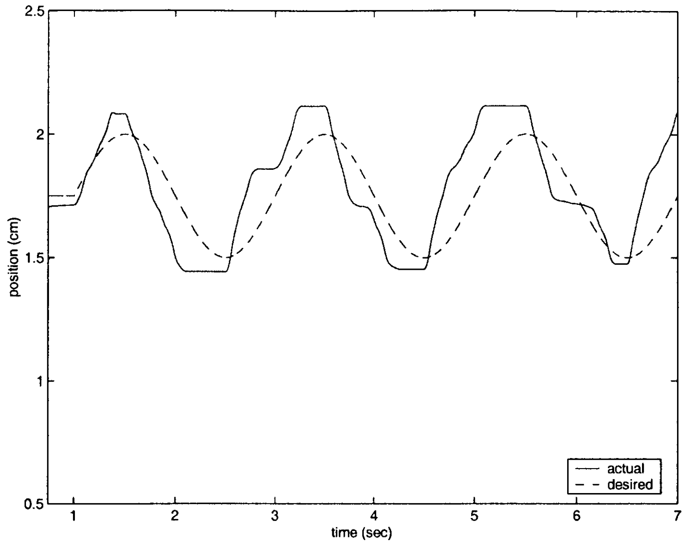

Figure 6-8: Position response to an open-loop trajectory command using second adjusted model.

6.3 Closed-loop response

Figure 6-9 shows the block diagram of the closed-loop PD controllers described in this section. In PD control, the command is proportionally related to position and velocity error. In the tests described below, the tracking position, $x_d(t)$, used was again an offset sine wave with a frequency of 1 Hz. Like the dynamic friction tests, a proportional gain, K, of 115 $\frac{\text{N}}{\text{cm}}$ and a derivative gain, B, of 11.5 $\frac{\text{N·s}}{\text{cm}}$ were used.

6.3.1 PD, no friction compensation

The first PD controller tested did not have a separate term to compensate for friction. The control law used was the basic implementation of PD control:

$$u = -K(x - x_d) - B(\dot{x} - \dot{x}_d) \tag{6.3}$$

Figure 6-10 shows the actual trajectory compared with the desired. By comparing peak-to-peak values of a single period, the magnitude response of the experiment was

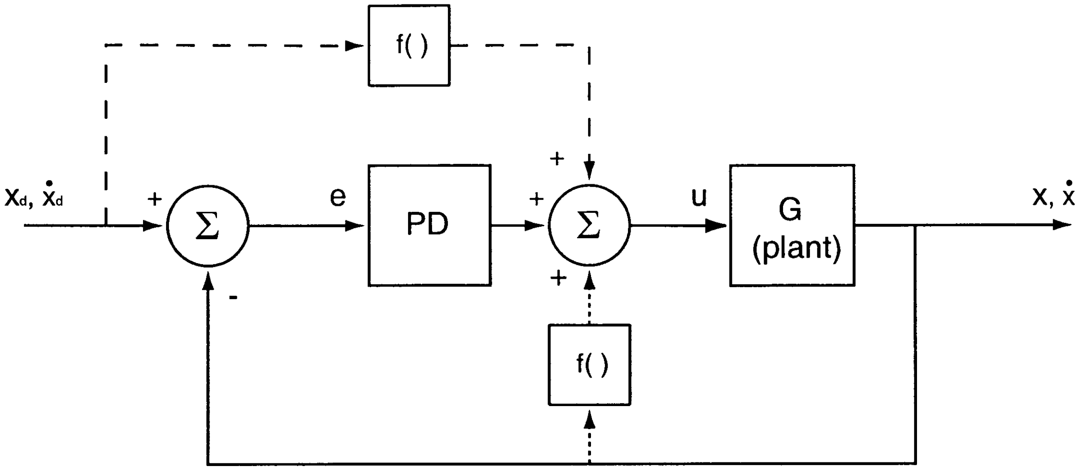

Figure 6-9: Block diagram of the closed-loop controllers implemented and tested. The dotted line represents feedback friction compensation. The dashed line represents feedforward friction compensation.

determined to be -0.57 dB. A phase lag of 12.6° was calculated by finding the time when the waveform crossed its midpoint.

6.3.2 PD, feedback compensation

Using the measured velocity, a feedback friction compensation term was added. In the block diagram of Figure 6-9, adding this extra term is the equivalent of adding the dotted line to the system. The second set of adjusted parameters were used for the model of friction in the compensation block. The control law thus became:

$$u = -K(x - x_d) - B(\dot{x} - \dot{x}_d) + f(\dot{x}) \tag{6.4}$$

Figure 6-11 shows the resulting trajectory under this controller. The friction compensation yielded a magnitude response of -0.09 dB and, interestingly enough, a phase lead of 2.16°.

Looking at the difference in error in Figure 6-12, it seems that the friction compensation evens the error reading out. This seems more evident in the plot of error versus position in Figure 6-13. This plot also reveals that the error is remarkably

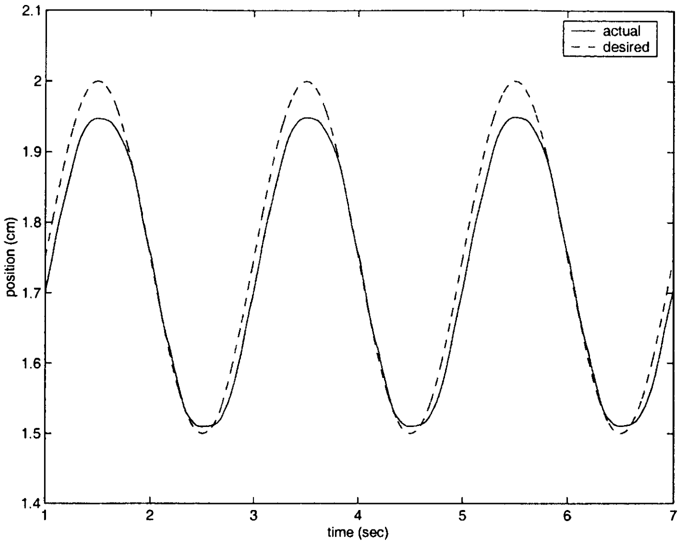

Figure 6-10: Position response of PD controller with no friction compensation.

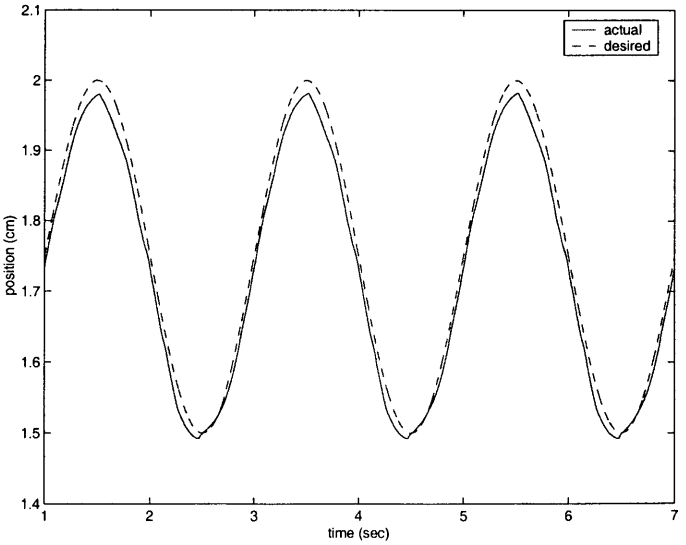

Figure 6-11: Position response of PD controller with feedback friction compensation.

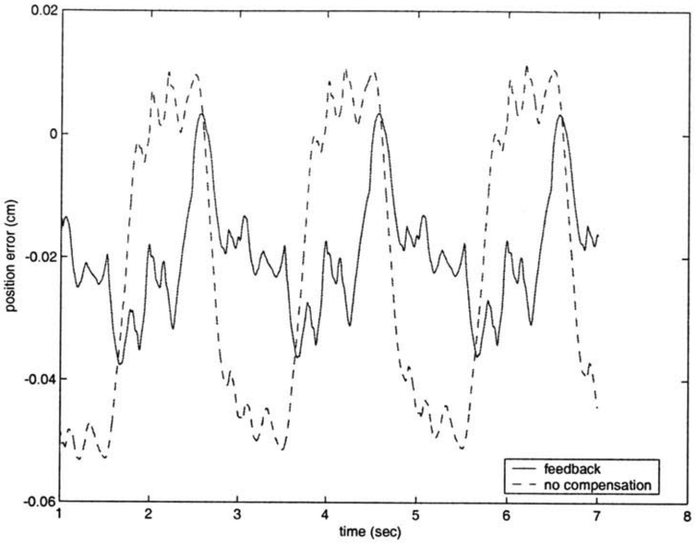

Figure 6-12: Tracking error of PD controllers with and without feedback compensation.

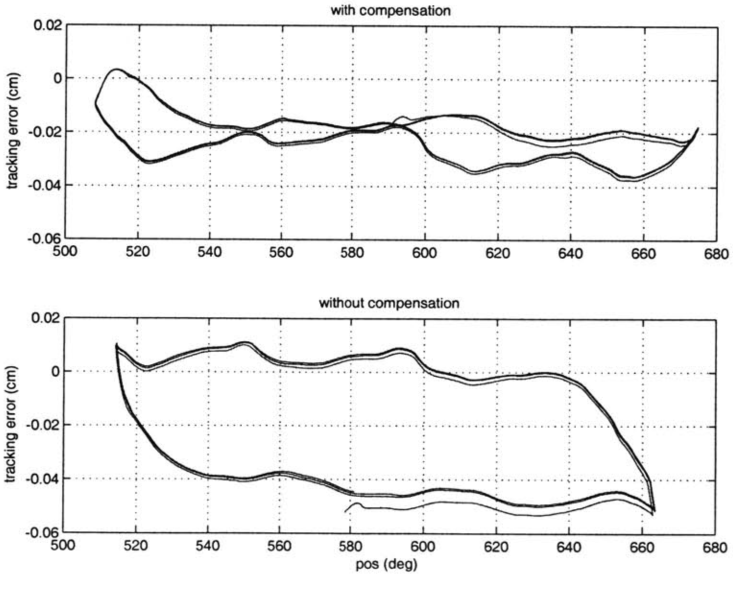

Figure 6-13: Tracking error of PD controllers with and without feedback compensation versus motor position.

repeatable with respect to position. The peaks in each period occur every 45° in motor position. This provides even more convincing evidence that the cogging effect in the motor produces position-dependent friction.

Separate tests were performed for the uncompensated and feedback compensated tests with the gains doubled. No significant effects were observed, however. The errors were halved but retained the same patterns.

6.3.3 PD, feedforward compensation

Using the desired velocity, a feedforward friction compensation term was added to the controller. The block diagram of this system is simply the solid and dashed lines of Figure 6-9. Again, the same friction model was used and the control law became:

$$u = -K(x - x_d) - B(\dot{x} - \dot{x}_d) + f(\dot{x}_d) \tag{6.5}$$

The resulting trajectory is shown in Figure 6-14 and is similar to the response with feedback compensation, yielding a magnitude response of -0.08 dB and phase lead of 2.52°. The error profiles are also almost identical, as shown in Figure 6-15. Thus, feedforward compensation does not stand out as having any more benefit or disadvantage compared with feedback friction compensation. This would likely change, however, if the robot were operated with human interaction.

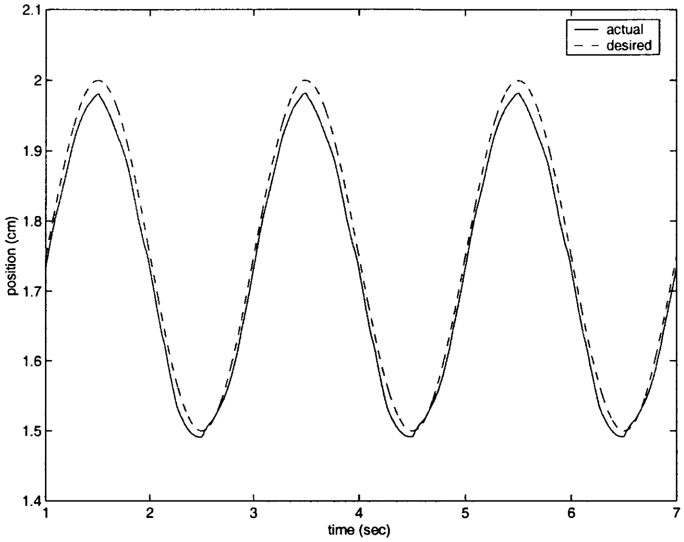

Figure 6-14: Position response of PD controller with feedback friction compensation.

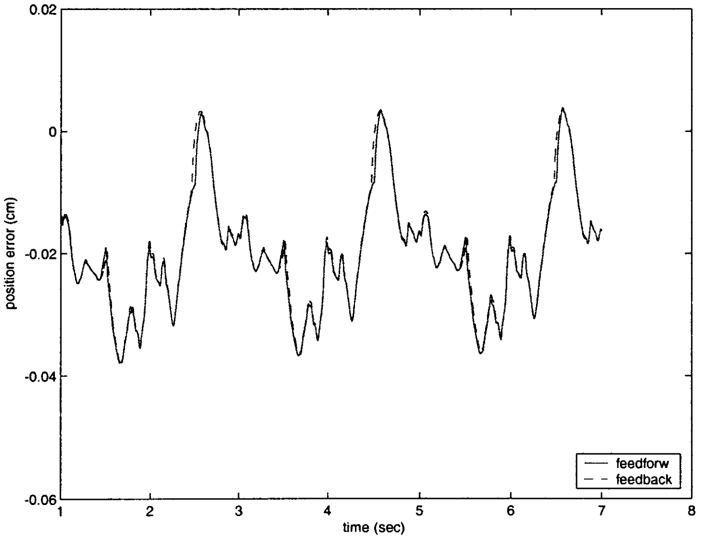

Figure 6-15: Tracking error of PD controllers with feedback and feedforward compensation.

Chapter 7

Conclusion

This thesis describes the characterization of a prototype robot designed for hand rehabilitation. During this process, several design flaws were revealed and some important discoveries were made concerning the design features of the robot. The following conclusions were made during this investigation:

- The initial design to house the frameless motors is inadequate and was detrimental to the performance of some of the actuators.
- The servo-amplifier and motor perform well enough to work for this robot, however, they do not meet the published or expected values for torque output and frequency response. Whether this has to do with the frame design remains to be seen.
- A significant amount of friction was expected in the transmission due to the numerous cable-hole interactions. In the investigation of one of these interactions, however, cable friction accounted for a maximum of less than one-third of the overall friction.
- Changing the exit angle of the cable out of its hole support increases static and Coulomb friction significantly and viscous friction only slightly.
- Cogging in the motor and non-uniformity in the gear teeth are causes of position-dependent friction. Although a thorough study of this position dependence was

not conducted, joint performance seemed to be impaired by this effect.

- Flexure stiffness did not seem to be a limiting factor in the tracking of a 1 hertz frequency trajectory. However, it was observed just through simple handling that the flexure would not be stiff enough in torsion during interactive operation.

- Even with just a rough model of friction, adding a compensation term to a closed-loop PD controller seems to even out the tracking error. No significant differences were observed between feedback and feedforward compensation.

7.1 Future work

Given the above conclusions, a large body of work remains before a working robot can be installed in clinics to treat actual patients.

- New motor boxes need to be designed with tolerance issues taken into account. One possibility is to design separate, identical frames for each motor which then would be connected to the motor box. The design would thus be modular, making it easier to install, replace, and repair the motors.

- It has been suggested that for articulated hand-like devices $2n$ actuators be used to pull opposing tendons for n joints [21]. It was not pursued before because the size of the actuator makes it impractical. But with the advances of technology, this may be an idea worth investigating.

- Efforts should be made to lower the position dependency of friction in the transmission. Although the presence of gears did not seem to add much Coulomb or viscous friction to the system, it did add noticeable position dependency. Without a means to adjust the axis location, gears also will add backlash to the transmission. A speed reduction using cables and pulleys may be worth investigation, as those systems are free of backlash [24, 25] and gear teeth interfaces.

- All of the experiments and analysis in this thesis were performed with the finger joints. So, a similar investigation needs to be performed with the thumb joints. In particular, the one non-flexural joint, the slider for thumb abduction/adduction, needs to be thoroughly examined. With no lubrication in the metal to metal contact, much friction is expected.

- The investigation of cable friction in this thesis left many parameters unstudied. Many of the cables are routed through holes longer than the one tested, which may possibly change the friction parameters. Hole sizes and cable type may also play a role in determining the effective friction. A more exhaustive study may yield more definitive conclusions and perhaps help minimize the power losses in the transmission.

- It is not clear what effect routing the PIP joint cables through the MCP joint has. Studying this cross-coupling effect will be important for the eventual controller scheme.

- A new set of flexures needs to be designed to strengthen the robot joints in torsion.

- After these flexures are designed, a better understanding of the kinematics of each joint is necessary, both in uncoupled and coupled interaction. This will help determine cable exit angles for particular movements, which will allow better actuator compensation for friction.

- At the beginning, crossing the cables through the flexure seemed impractical for this prototype. But with a better understanding of the friction properties of the cable, it may be possible to incorporate this feature in future designs.

- It has been suggested that instead of having the three outer fingers bound, the fingers be bound in pairs — the index with the middle and the ring with the little finger. Delicate grasping with the index finger is replaced with a more functional form of grasping with the index and middle fingers together.

- Measurand model S720 joint sensors were intended to measure each flexure angle. To date, minimal work has been accomplished in characterizing them.

More is necessary if these sensors are to be a useful tool, either for clinical analysis or for control purposes.

- As it currently is designed, it is rather difficult to secure even an unimpaired hand to the robot. A therapist trying to set up a stroke patient would then have extreme difficulty. A different patient-robot interface needs to be designed. One idea proposed is to have a detachable mechanism that the therapist first connects to the patient. Once that is done, the mechanism can then be attached to the robot. This may prove to be a useful safety feature as well, allowing the therapist or the patient to quickly remove his/her hand from the device in the event of some failure.

- Once an acceptable hardware prototype is made, ideas for a software game can be considered. In therapy sessions with MANUS, patients use the robot arm to move a cursor to various targets on a video monitor. A similar game that requires the patient to move specific finger joints to certain angles is needed. One that focuses more on functional exercises would be ideal.

A robot with the ability to rehabilitate the hand and fingers could be invaluable to the recovery of stroke patients. This thesis details just some of the preliminary work in the tremendous undertaking to design such a device. With continued and focused effort, however, an effective and efficient robot can be designed, manufactured, and made fit for operation.

Appendix A

Current Sensor data

A.1 Architecture

The three-phase current sensor described in Chapter 4 was custom-built according to the schematic shown in Figure A-1. Each phase used one Burr-Brown INA117 difference amplifier and two operational amplifiers.

In the first stage, the output of the amplifier was simply the difference in voltage that was measured:

$$V_{out} = V_{motor} - V_{servo} = iR_s \tag{A.1}$$

A high-power linear resistor rated at 0.1Ω (R_s) was placed in the current line being sensed, so the voltage out was proportional to current in.

The signal was then low-pass filtered in the next stage. The circuit was designed as a two-pole Butterworth filter with a transfer function of:

$$\frac{V_{out}}{V_{in}} = \frac{\frac{1}{R_1R_2C_1C_2}}{s^2 + s\frac{(R_1+R_2)C_1}{R_1R_2C_1C_2} + \frac{1}{R_1R_2C_1C_2}} \tag{A.2}$$

and a cutoff frequency of:

$$\omega_c = \sqrt{\frac{1}{R_1R_2C_1C_2}} \tag{A.3}$$

The components used in this sensor were nominally $R_1 = 19.6k\Omega$, $R_2 = 20k\Omega$, $C_1 = .005\mu F$, and $C_2 = .015\mu F$, which yields an ω_c of 928.2 hertz.

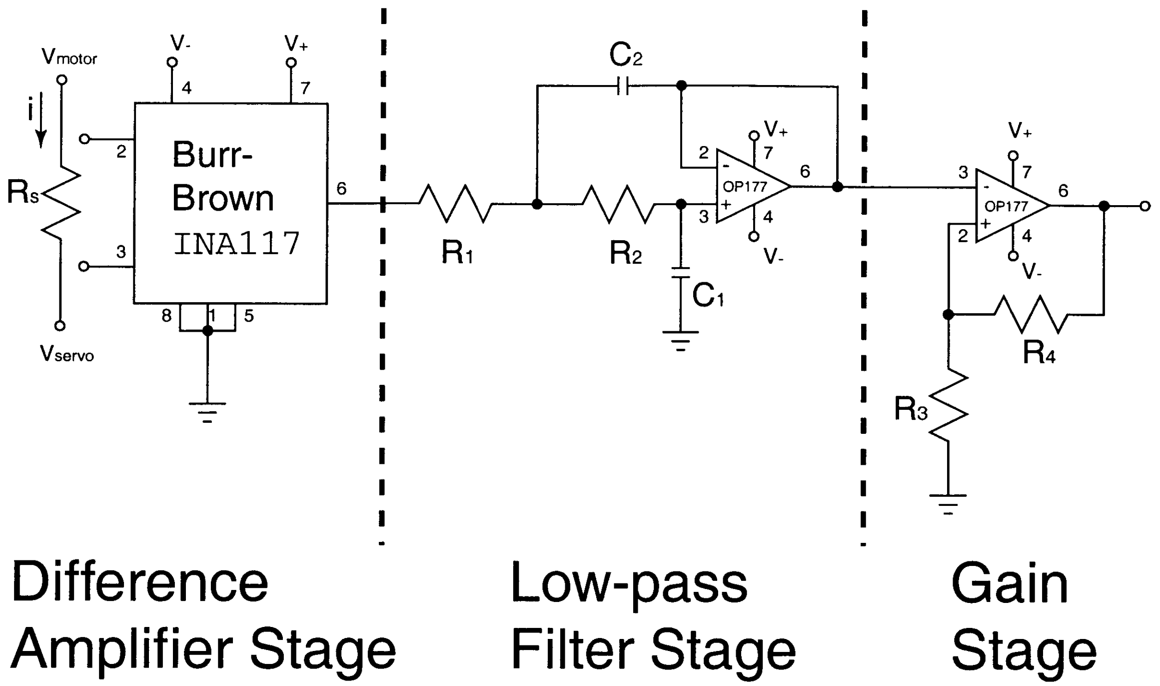

Figure A-1: Electrical schematic of custom-built current sensor

The final stage was a gain stage intended to strengthen the signal to a range of values detectable by the measuring equipment. The equation for gain, G, is simply:

$$G = \frac{V_{out}}{V_{in}} = \left(1 + \frac{R_4}{R_3}\right) \tag{A.4}$$

Resistors of 4.99 kΩ and 15 kΩ were used for R_3 and R_4, respectively, yielding a gain of $G = 4$.

A.2 Additional figures

Figures A-2 through A-10 show the results of the frequency response test for each phase. The figures for phase A are from Section 4.2.2 and are repeated here for comparison.

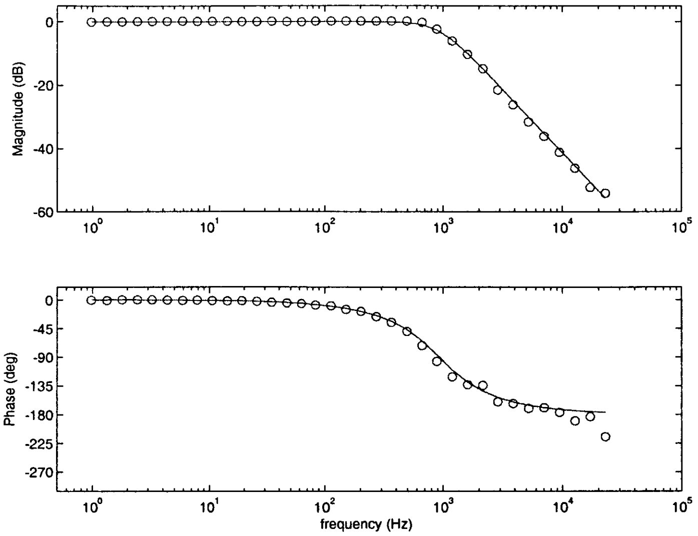

Figure A-2: Phase A frequency response plotted with a fitted model. Voltage output/input. Repeated from Figure 4-4.

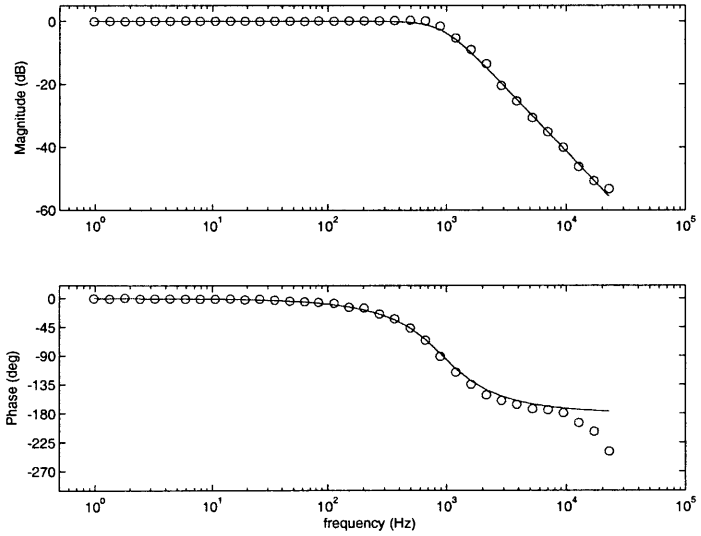

Figure A-3: Phase B frequency response plotted with a fitted model. Voltage output/input.

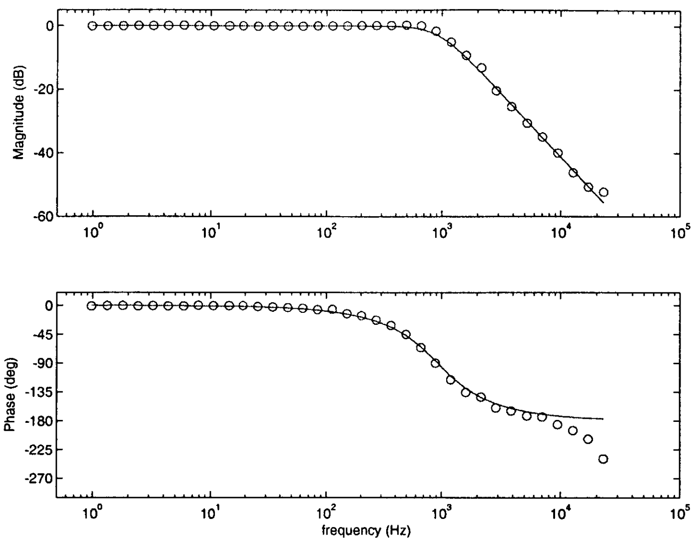

Figure A-4: Phase C frequency response plotted with a fitted model. Voltage output/input.

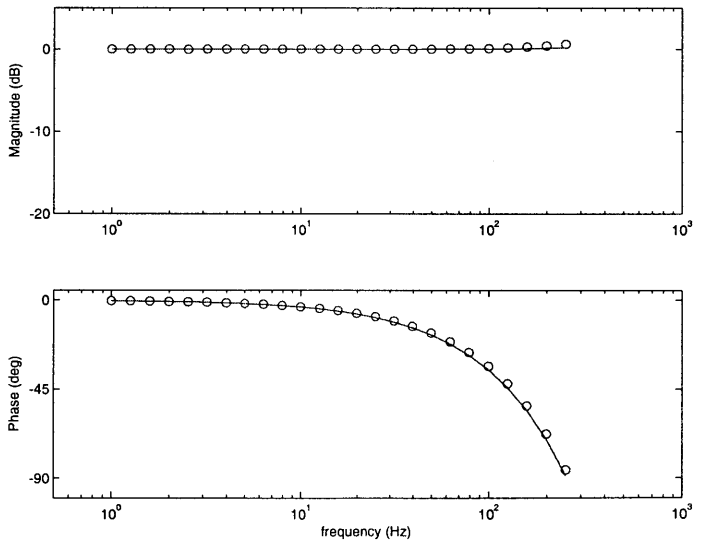

Figure A-5: Phase A frequency response in sampled test with fitted model. Voltage output/input. Repeated from Figure 4-7.

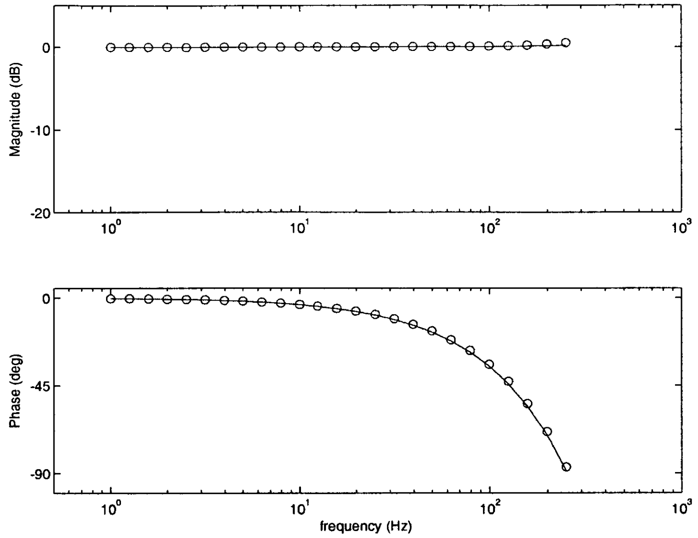

Figure A-6: Phase B frequency response in sampled test with fitted model. Voltage output/input.

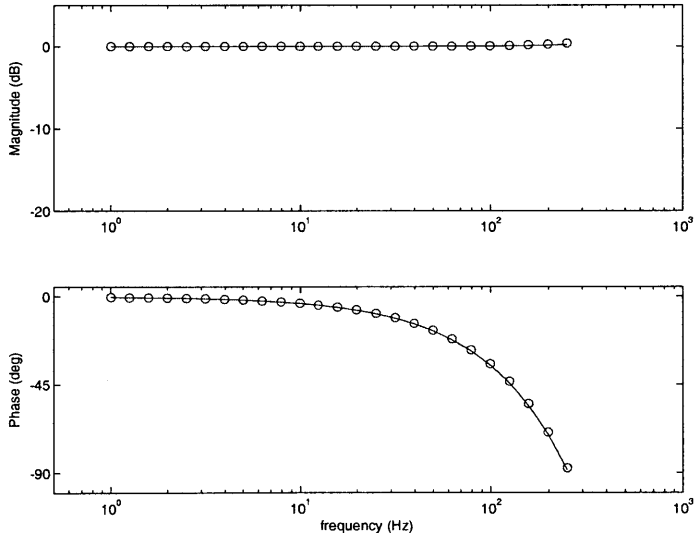

Figure A-7: Phase C frequency response in sampled test with fitted model. Voltage output/input.

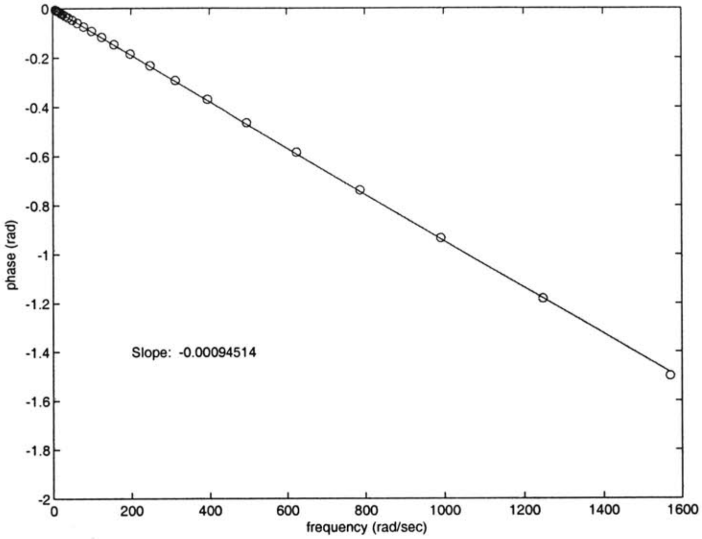

Figure A-8: Phase lag of phase A in sampled test plotted on a linear scale. Magnitude of the slope of the linear fit corresponds to time delay. Repeated from Figure 4-6.

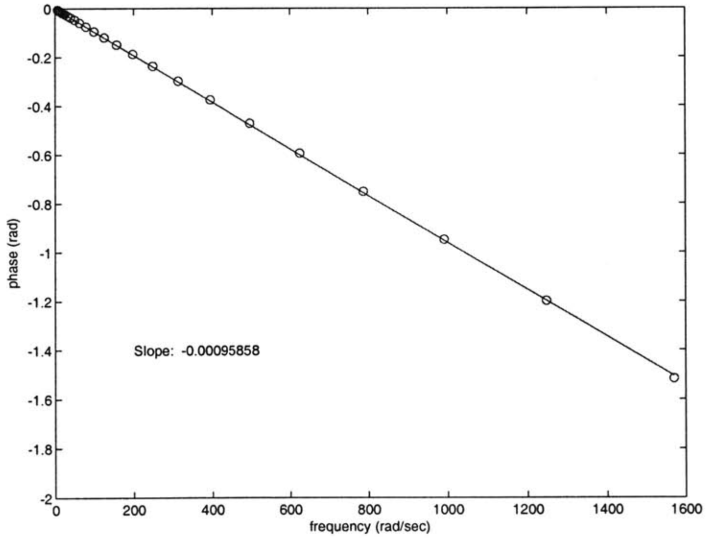

Figure A-9: Phase lag of phase B in sampled test plotted on a linear scale. Magnitude of the slope of the linear fit corresponds to time delay.

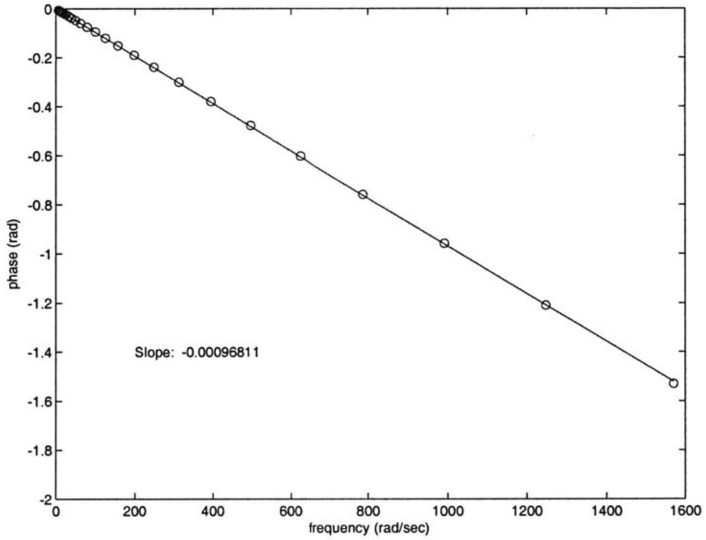

Figure A-10: Phase lag of phase C in sampled test plotted on a linear scale. Magnitude of the slope of the linear fit corresponds to time delay.

Appendix B

Servo-amplifier parameters

The Kollmorgen servo-amplifiers are compatible with several different motors made by the company. However, this feature requires the user to change parameters in the amp through software to define proper limits and feedback loops for the motor-amp pairing. Table B.1 lists some of the important parameters and the values that were used for all the testing done in this thesis. Descriptions are also provided.

Parameter	**Value**	**Units**	**Description**
MIPEAK	225	0.1 amps	peak RMS current of the motor
MICONT	58	0.1 amps	continuous RMS current of the motor
MSPEED	18,000	rpm	maximum velocity of the motor
MJ	15	10^{-6} kg·m^2	rotor inertia
MLMIN	47	10^{-5} H	electrical inductance in the motor
MBEMF	7	$\frac{\text{V}}{\text{krpm}}$	back EMF in the motor
MENCTYPE	0	N/A	motor encoder type: set to two channels (A and B) with index bit and Hall sensors
MENCRES	5120	$\frac{\text{lines}}{\text{rev}}$	motor encoder resolution
MTANGLC	0	electrical deg	angle advance at peak current
MTANGLP	0	electrical deg	angle advance at continuous current
MVANGLH	0	electrical deg	angle advance at half the maximum motor speed
MVANGLF	0	electrical deg	angle advance at maximum motor speed
IMAX	1000	0.1% of drive peak current	maximum allowable system current: it is set at 100% because the peak current from the amp is less than the peak current of the motor
ICONT	322	0.1% of drive peak current	used in the foldback algorithm of the amp, preventing current levels from staying above the continuous current of the motor for too long
ILIM	1000	0.1% of drive peak current	software limit imposed on output current
ISCALE	1000	0.1% of drive peak current per 10 volts	defines RMS current output to DC voltage input ratio
VBUS	160	Volts	DC bus voltage powering the amp
OPMODE	3	N/A	system mode: set to receive analog voltage input

Table B.1: Values of key parameters set in the servo-amp for all testing.

Appendix C

Motor torque composition

Figure C-1 is a sketch of the top view of the test apparatus used to measure torque from the motor. Washers were placed between the bar and the force transducer plate in an attempt to reduce the interaction to point-to-point contact.

Figure C-2a is the free-body diagram of the bar. The bolt was assumed to provide a load only along its center axis, and the washers a shear force and couple. Taking the sum of moments about point O and setting it to zero, we get:

$$\Sigma M_O = \tau_m - \tau_y - F_z d - F_x w = 0 \tag{C.1}$$

The reaction on the rest of the assembly is shown in Figure C-2b, where point A is collocated with the origin of both the ground and force transducer reference frames. Because the z axes are the same in both frames, the measured force in z of the force transducer, F_{ftz} is simply F_z. But because the other axes are at an angle α, the force transducer measures F_x and τ_y as:

$$F_x = F_{fty}\sin(\alpha) - F_{ftx}\cos(\alpha) \tag{C.2}$$

$$\tau_y = \tau_{ftx}\sin(\alpha) + \tau_{fty}\cos(\alpha) - F_x h \tag{C.3}$$

α is dependent on the geometry of the adapter plate on the force transducer and was measured to be 47.95°. Rearranging Equation C.1 and substituting terms with

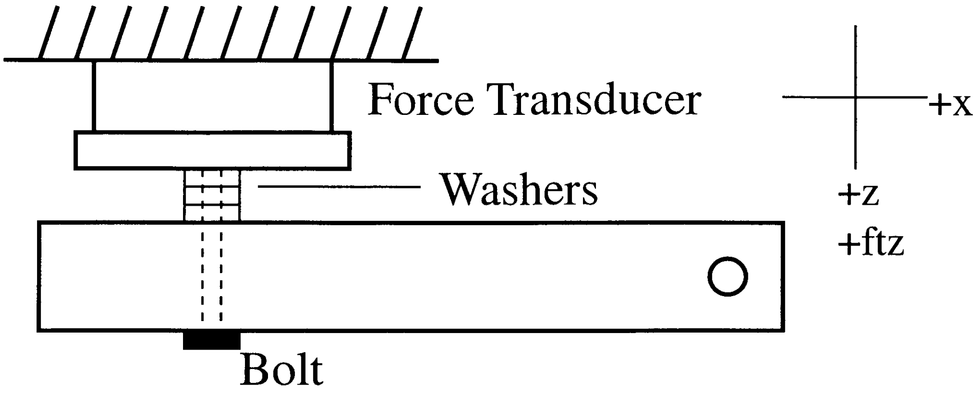

Figure C-1: Top view of the test apparatus used to measure torque from the motor, with reference axes. The ground z and force transducer z axes are coaxial. Sketch not to scale.

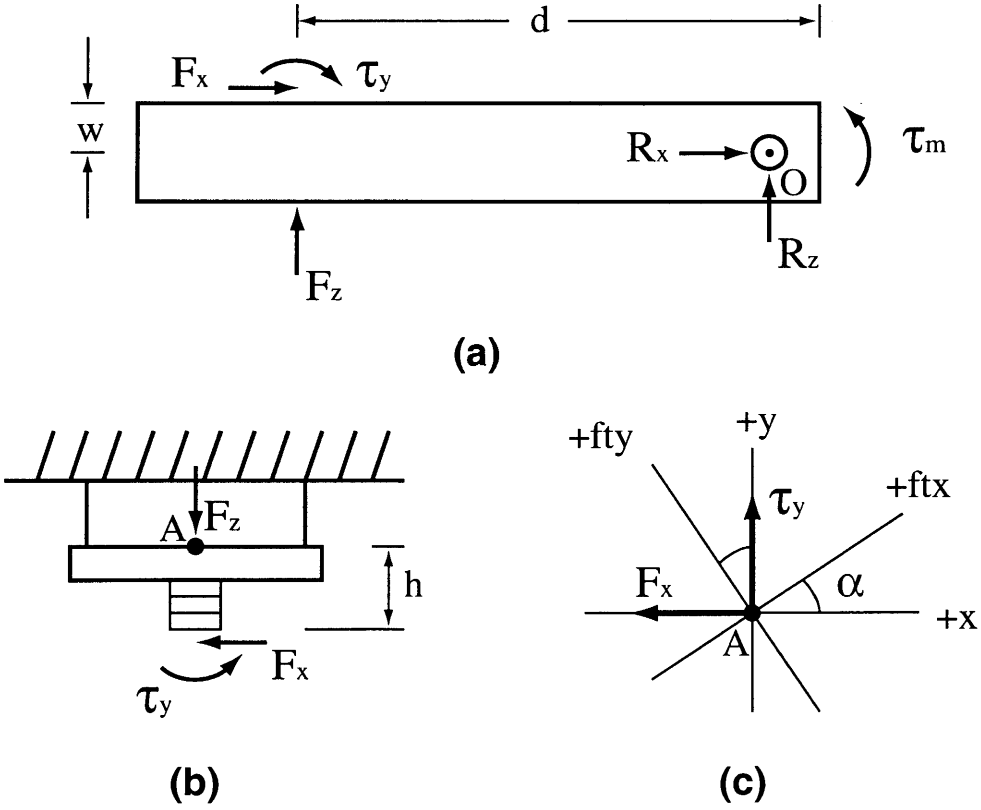

Figure C-2: (a) Free-body diagram of the bar; top view. (b) Free-body diagram of the collective assembly of the force transducer, force transducer plate, and washers; top view. (c) Ground and force transducer reference axes; side view.

Equations C.2 and C.3, the torque of the motor can be composed from the force transducer measurements with the following equation:

$$\tau_m = \tau_{ftx}\sin(\alpha) + \tau_{fty}\cos(\alpha) + F_{ftz}d + [F_{fty}\sin(\alpha) - F_{ftx}\cos(\alpha)](w - h) \tag{C.4}$$

Appendix D

Dynamic Friction Test Data

The following figures show the individual plots of the dynamic friction test data. A detailed description of the test method can be found in Chapter 5. Means of the calculated friction for each trial and error bars of $\pm 1.68\sigma$ are shown.

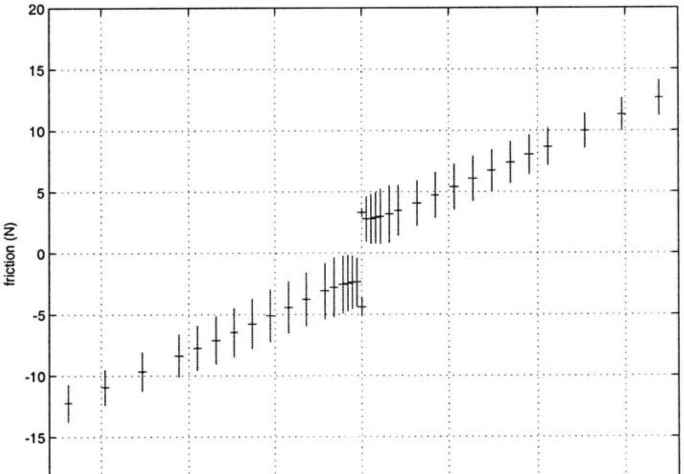

Figure D-1: Dynamic friction data from test of motor alone and unloaded.

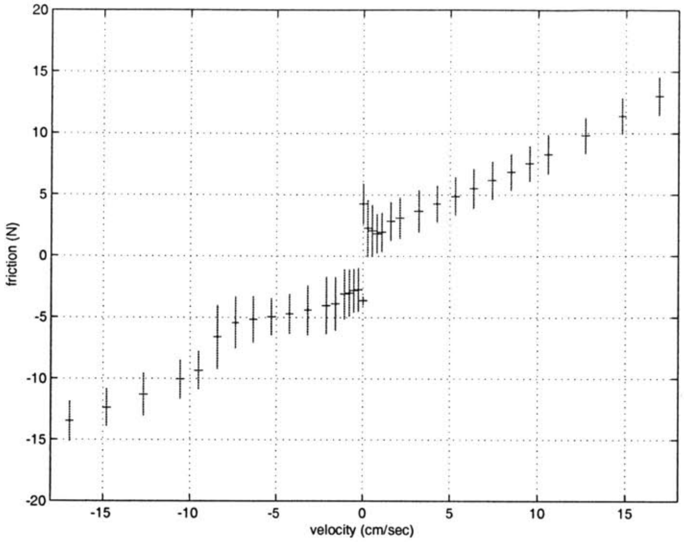

Figure D-2: Dynamic friction data from gear test.

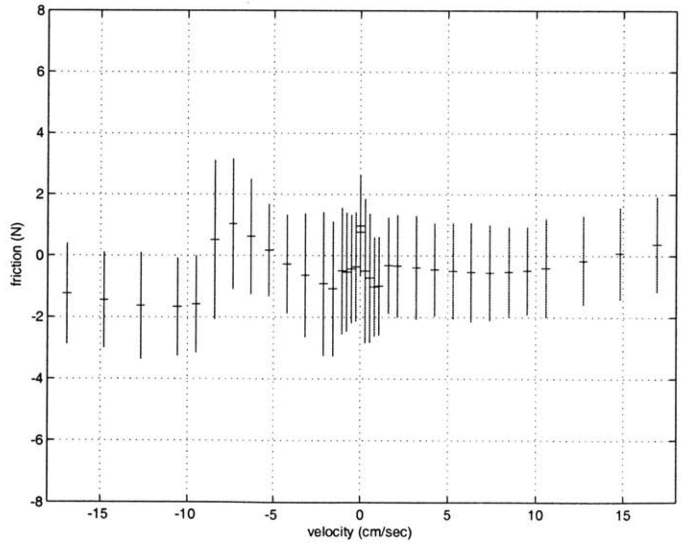

Figure D-3: Contribution to dynamic friction from the gear. Data from gear test minus means from motor test.

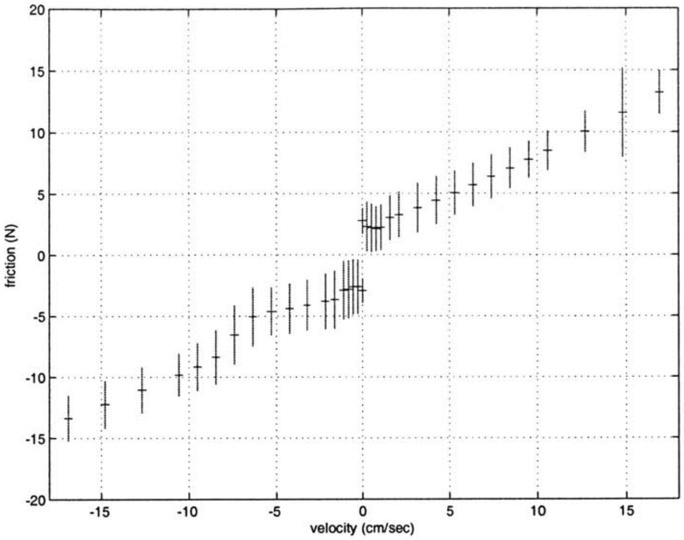

Figure D-4: Dynamic friction data from 0° test.

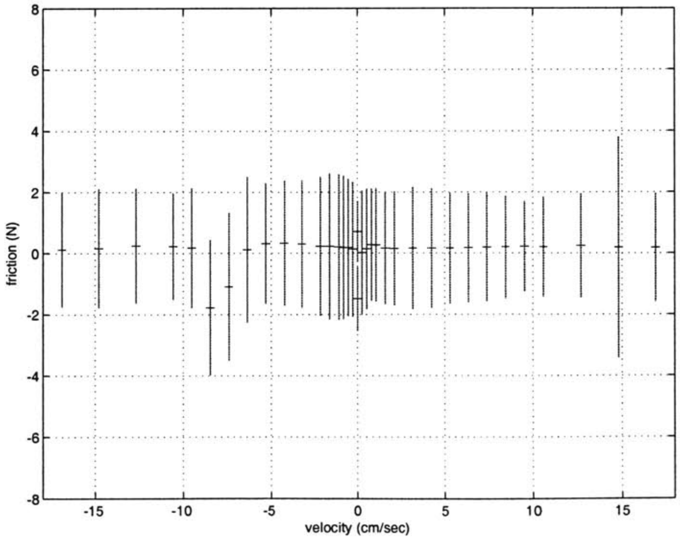

Figure D-5: Contribution to dynamic friction from the cable-hole interface. Data from 0° test minus means from gear test.

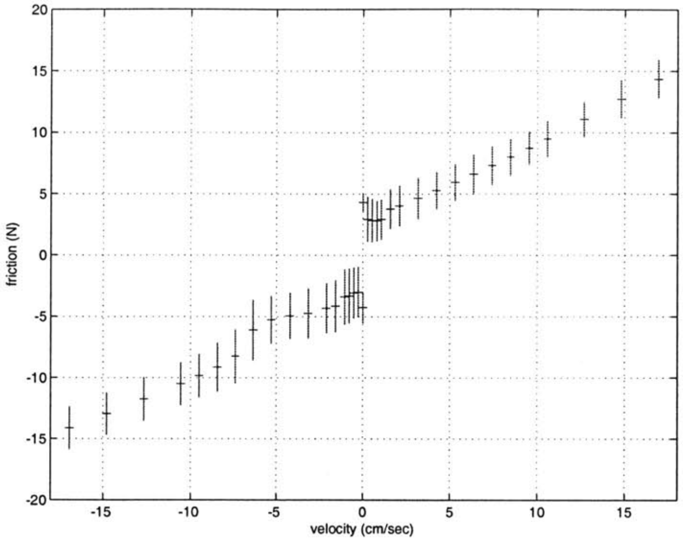

Figure D-6: Dynamic friction data from 15° test.

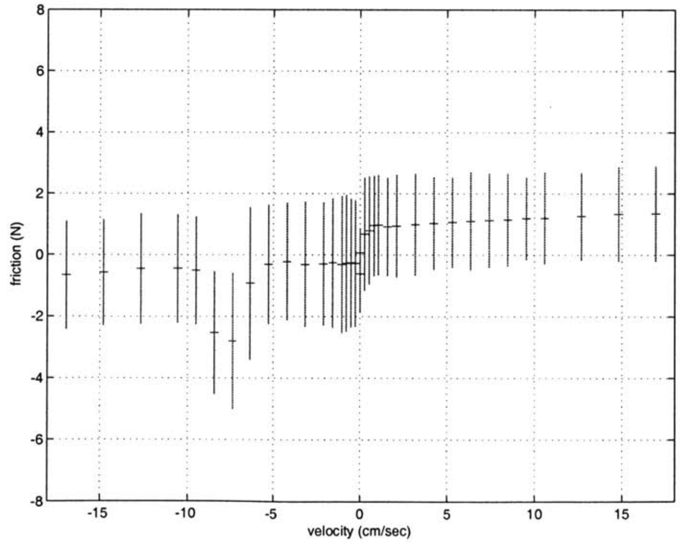

Figure D-7: Contribution to dynamic friction from the cable-hole interface. Data from 15° test minus means from gear test.

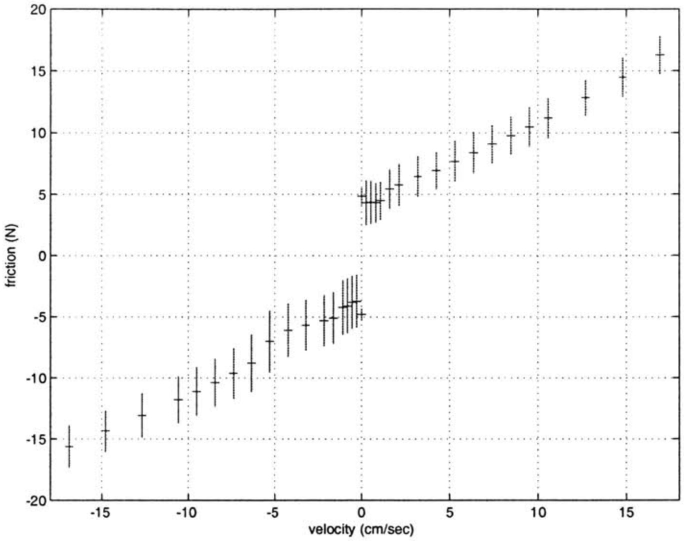

Figure D-8: Dynamic friction data from 30° test.

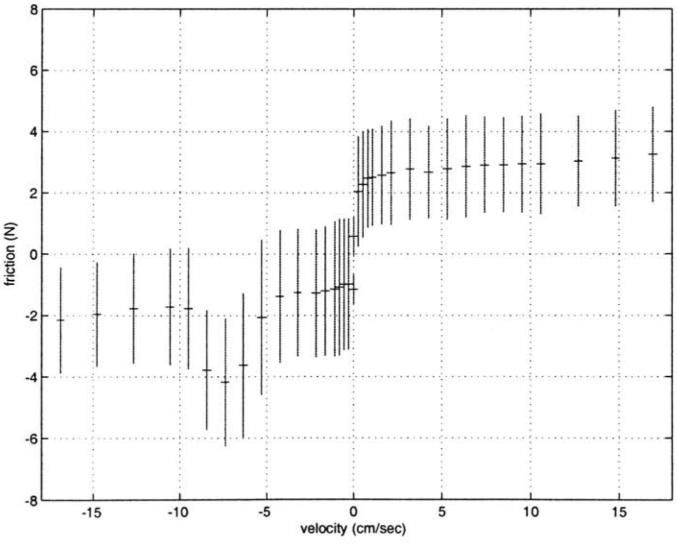

Figure D-9: Contribution to dynamic friction from the cable-hole interface. Data from 30° test minus means from gear test.

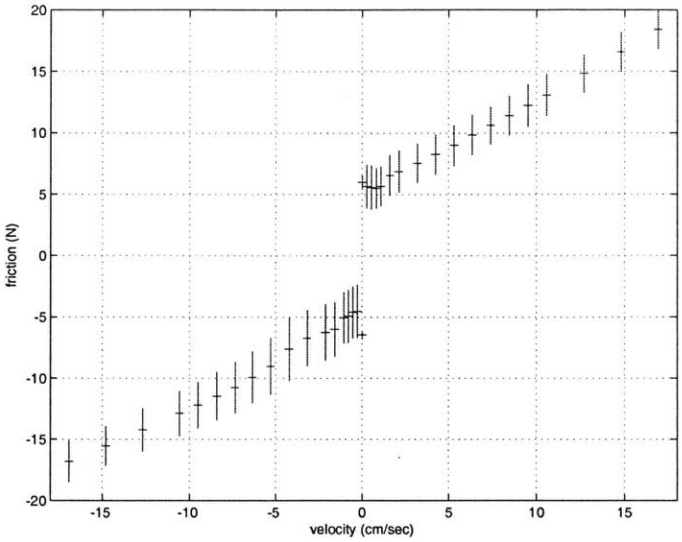

Figure D-10: Dynamic friction data from 45° test.

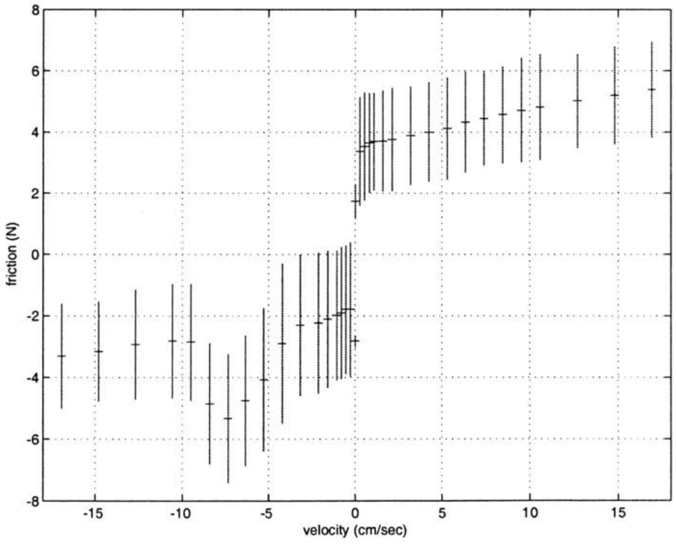

Figure D-11: Contribution to dynamic friction from the cable-hole interface. Data from 45° test minus means from gear test.

Appendix E

Linear Model Analysis

The following is an internal report written in May 2001. It describes an analytical model of the finger robot system using elements having only linear constitutive laws. A physical model of one one-degree-of-freedom flexural joint was created and a bond graph was used to determine its equations of motion. Relevant parameters needed for simulation were then measured, calculated, or estimated. The open-loop frequency response of the endpoint position given an input motor torque was used to determine the effect of varying the parameters.

E.1 Physical model

First, a physical, mechanical model was created for the flexural joint (Figure E-1). It is a rather simplified way of viewing the system, but it still takes into account the factors that are most important to the behavior of the system. The gears and pulley are modelled simply as rotational inertias. The compliance throughout the transmission cable was lumped together and modelled as a spring. The flexure compliance was also modelled as a spring, but in the rotational domain. The mass at the endpoint includes that of the robot components attached to the flexure as well as that of the patient's finger. It is modelled as a rotational inertia.

One important assumption made in this physical model was that each joint acts independently — that is, the motion of one joint is not affected by that of any other.

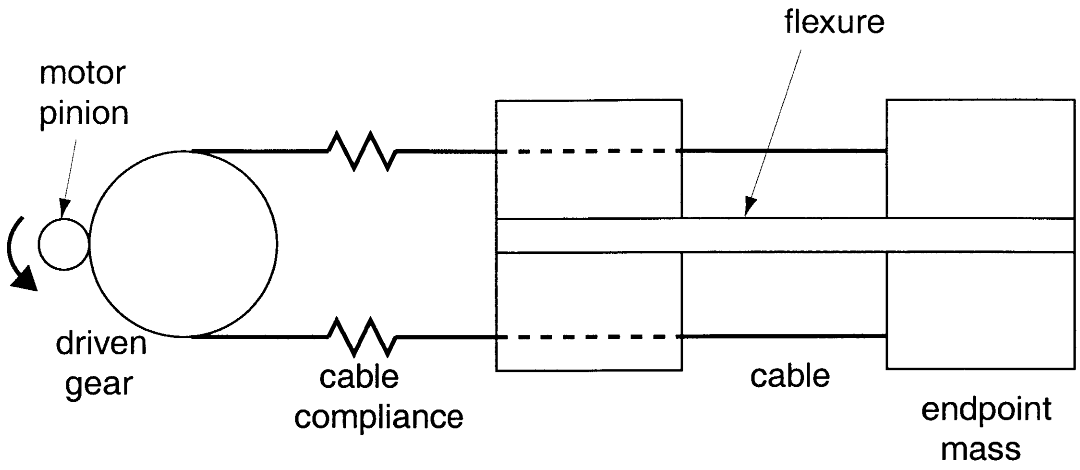

Figure E-1: Mechanical model of flexural joint, repeated from Figure 5-1.

Although this may not be entirely true (as evident from moving the hardware itself), it simplifies the analysis greatly. Another assumption made was that each element of the system behaves linearly. It is highly probable that this is not the case, but it allows the use of many methods and tools that, again, greatly simplify the analysis.

So although this model may not be exact, it is still useful because its analysis can at least clarify the relationship between the parameters and the system behavior. This will help one to predict the effect of any modifications made to the robot.

E.2 Bond graph

The physical model was then translated into a bond graph (Figure E-2). The following is a list of what each element corresponds to (note: the bond graph drawn below and the following discussion follow conventional bond graph techniques and terms):

SE	Torque input from the motor
I_1	Moment of inertia of the motor shaft and drive gear
I_2	Moment of inertia of the driven gear and pulley
I_3	Moment of inertia of endpoint mass

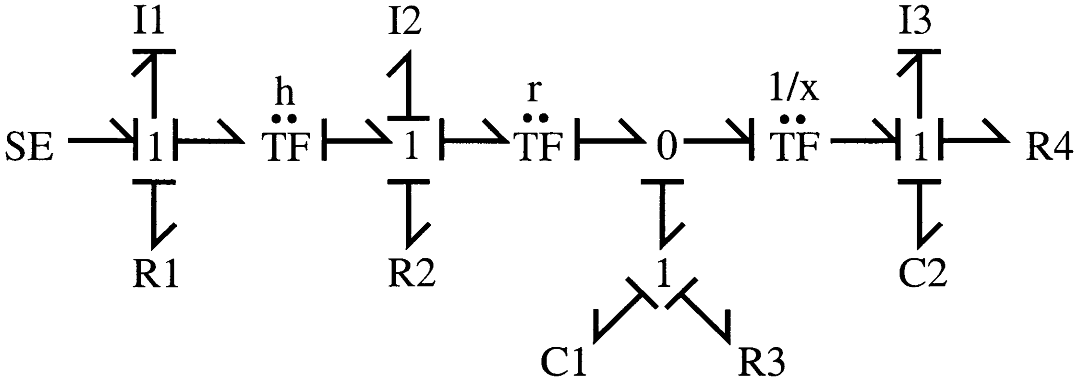

Figure E-2: Bond graph of physical model.

R_1	Friction in the motor bearings
R_2	Friction in the bearings for the driven shaft and friction on the cable in the through holes
R_3	Internal damping in the cable
R_4	Internal damping in the flexure
C_1	Compliance due to cable stiffness
C_2	Compliance due to the flexure stiffness
h	Gear ratio
r	Moment arm from pulley (pulley radius)
x	Moment arm from cable (distance from centerline of flexure to cable attachment)

One may notice that the inertial element from the driven gear and pulley is in derivative causality. This is not surprising, however, since its motion is directly coupled to the motion of the drive gear and motor. It is possible to lump I_1 and I_2 to create one effective inertia element (as well as R_1 and R_2 into an effective damping element), but, for clarity in the analysis and discussion, the bond graph will be left unchanged.

This bond graph is applicable to all the flexural joints of the robot. This paper examines the system that drives the proximal interphalangeal (PIP) joints of the three outer fingers specifically. The model in the following discussion assumes this. But a model of any of the other flexural joints can be made by estimating the parameters in that particular system.

E.3 Equations of motion

As mentioned before, each element was estimated to behave linearly — effort on an inertia is proportional to its acceleration, effort on a damping element is proportional to its flow, and the flow of a compliance is proportional to the derivative of its effort. The constants that satisfy these relationships were the parameters needed to estimate the behavior of the system. Many of them were simply rough estimates (moments of inertia of the motor and the endpoint mass and all damping coefficients). Some were measured (transformer ratios). Other values, however, were estimated based on theoretical calculations.

The driven gear and pulley were lumped together as one mass and assumed to be symmetric about their common axis of rotation. Thus, the mass moment of inertia could be estimated using the following equation [7]:

$$I = \frac{1}{2}mr^2 \tag{E.1}$$

where m is the mass of the body and r is its radius. The value for m used in the model was taken from a measurement of the mass of the gear, pulley, and shaft. And since the gear seemed to account for the majority of the mass, its radius was used as an estimated value for r.

The stiffness of the cable was estimated using the standard axial stiffness equation for a beam:

$$K_{cable} = \frac{AE}{l} \tag{E.2}$$

where A is the cross-sectional area, E is the Young's modulus of the material, and l is the length. The compliance of the cable (C_1) is simply the reciprocal of the stiffness.

The flexure stiffness was estimated using a number of steps. It is important to note first, though, that the real flexure is slotted twice, creating effectively three identical flexure slivers. The whole flexure stiffness was calculated by first analyzing these slivers. First, each sliver was assumed to act as a cantilever beam. Its stiffness was calculated using the following equation for a clamped flexure [23]:

$$K_y = \frac{2EI_{zz}}{l^2(\frac{2l}{3} + \frac{L}{2}) + \frac{2lw^2(1+\nu)}{5}} \tag{E.3}$$

where l is the length of thin section, L is the length of the thick section, w is the width, ν is Poisson's ratio, and $I_{zz} = \frac{1}{12}wt^3$ (t being the thickness of the thin section). This value for stiffness is given in force per distance deflected (1062 N/m). However, the rotational stiffness is desired for the equations of motion.

To calculate the rotational stiffness, the force needed to deflect the sliver one millimeter was determined (~1 N). The moment created by this force was determined by simply multiplying the force by the moment arm (length of the entire sliver — 35 mm). The angular displacement was then estimated from the linear displacement. The rotational stiffness was then calculated (moment applied divided by resulting angular displacement), yielding a value of approximately 1 $\frac{\text{N}\cdot\text{m}}{\text{rad}}$.

To obtain the stiffness of the whole flexure (not just one sliver), this value was then multiplied by three, as if one were computing the stiffness of three springs in parallel. The compliance (C_2), again, is just the reciprocal of this stiffness.

Although the methods used to determine the compliance of the flexure are not entirely precise, they still at least yield a decent estimate of its value.

Defining the state variables as ω_1 (angular velocity of the motor), F (force on the cable), ω_3 (angular velocity of the endpoint), and τ (torque from the flexure) and using the parameters described above, the following equations of motion were derived:

$$\dot{\omega}_1 = \frac{\tau_{in} - (b_1 + h^2 b_2 + h^2 r^2 b_3)\omega_1 - hrF + hrxb_3\omega_3}{I_1 + h^2 I_2} \tag{E.4}$$

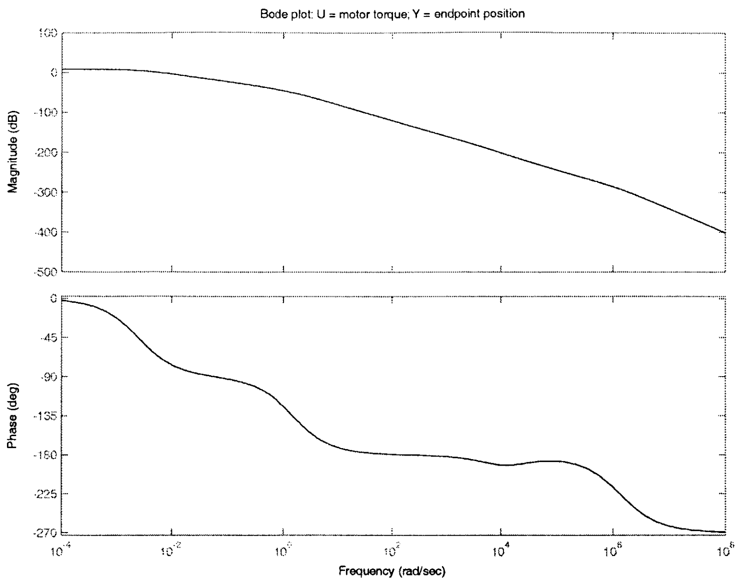

Figure E-3: Open-loop frequency response of the system with given parameters.

$$\dot{F} = \frac{hr\omega_1 - x\omega_3}{C_1} \tag{E.5}$$

$$\dot{\omega}_3 = \frac{hrxb_3\omega_1 + xF - (x^2b_3 + b_4)\omega_3 - \tau}{I_3} \tag{E.6}$$

$$\dot{\tau} = \frac{\omega_3}{C_2} \tag{E.7}$$

where τ_{in} is the input torque from the motor and b_i is the coefficient of the i-th damping element.

E.4 Analysis

Using these state equations, the open-loop frequency response was plotted in Matlab using τ_{in} (N·m) as the input and the endpoint position (radians) as the output (Figure E-3). Some of the parameters were varied in order to gain a better understanding of how they affected the response of the system.

The model shows that by increasing the flexure stiffness, the magnitude response degrades at lower frequencies but the phase response does not lag as much (Figure E-4). It also shows that, within a certain range of frequencies, increasing cable stiffness

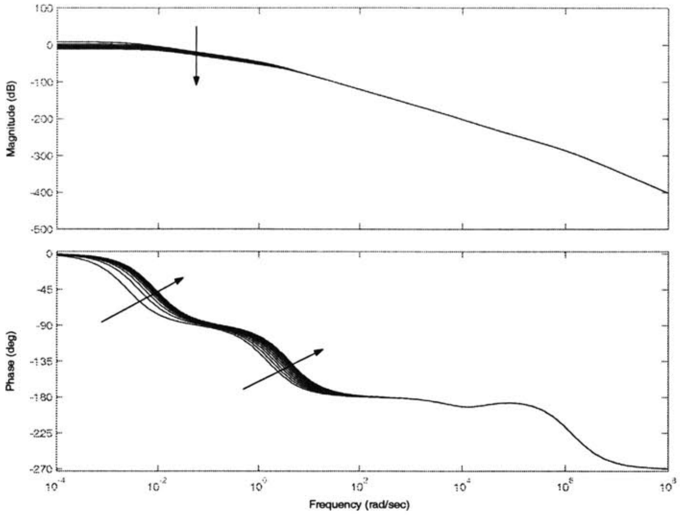

Figure E-4: Response of the system due to increasing flexure stiffness.

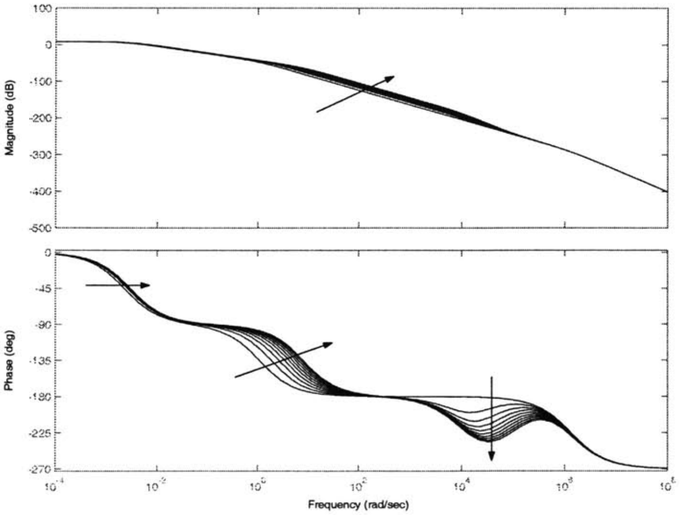

Figure E-5: Response of the system due to increasing cable stiffness.

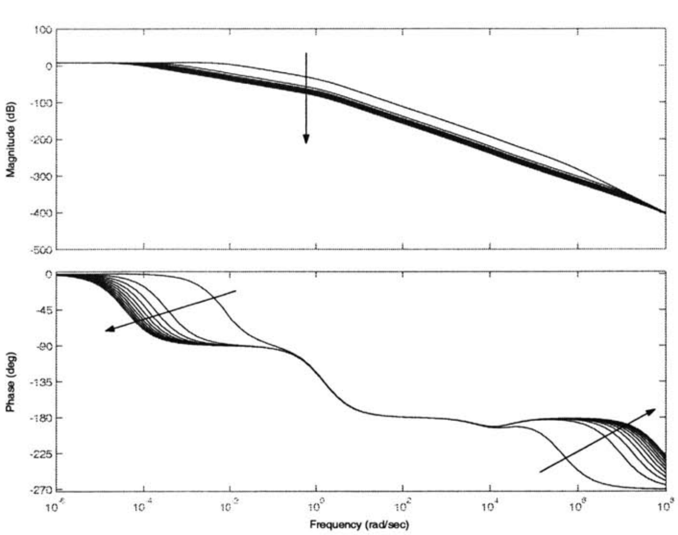

Figure E-6: Response of the system due to increasing friction in motor bearings.

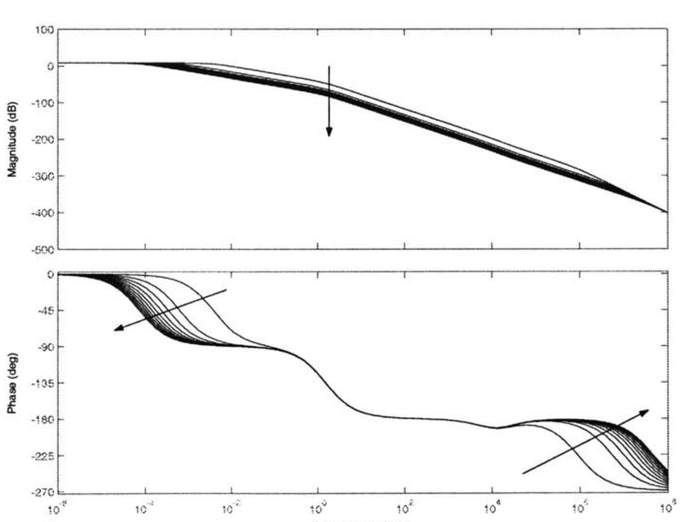

Figure E-7: Response of the system due to increasing friction in driven shaft bearings and friction on the transmission cable.

benefits the magnitude response, as expected (Figure E-5). Increasing the friction in the bearings and on the cable seems to have essentially the same effect — degrading the magnitude response and causing the phase response to lag at lower frequencies (Figure E-6 and E-7). This is also the expected result.

E.5 Conclusion

As mentioned before, several rather bold assumptions were made to create this model. Even from preliminary interaction with the hardware, it is rather clear that actuation of particular joints will affect others and that some components of the system have highly nonlinear effects (such as the static friction at the interaction points between the transmission cables and the holes that it runs through). However, this linear model still reveals some insight concerning the effects that some parameters have on the behavior of the system. Future work may include adding nonlinearities to the constitutive laws of the bond graph elements to better simulate the dynamics of the system.

Currently, the robot is being prepared for experiments and testing. It will be interesting to see how the actual response of the system compares to the simulations presented here.

Bibliography

[1] Aisen, M. L., H. I. Krebs, N. Hogan, F. McDowell, and B. T. Volpe. 1997. The Effect of Robot-Assisted Therapy and Rehabilitative Training on Motor Recovery Following Stroke. *Archives of Neurology* 54:443-446.

[2] Aisen, M. L., H. I. Krebs, N. Hogan, and B. T. Volpe. 1998. Robot-aided neurorehabilitation. *IEEE Transactions on Rehabilitation Engineering* 6:75-87.

[3] American Heart Association. 2001. *2002 Heart and Stroke Statistical Update.* Dallas, TX: American Heart Association.

[4] Anderson, James E. 1983. *Grant's atlas of anatomy.* Baltimore, MD: Williams and Wilkins.

[5] Armstrong-Helouvry, Brian. 1991. *Control of machines with friction.* Boston, MA: Kluwer Academic Publishers.

[6] Armstrong-Helouvry, Brian, P. DuPont, and C. Canudas de Wit. 1994. A Survey of Models, Analysis Tools, and Compensation Methods for the Control of Machines with Friction. *Automatica* 30:1083-1138.

[7] Beer, Ferdinand P. and E. Russell Johnston, Jr. 1988. *Vector mechanics for engineers: Statics and dynamics.* 5th ed. New York, NY: McGraw-Hill.

[8] Buerger, Stephen P. 2001. *Characterization and control of an interactive robot.* MSME Thesis, Massachusetts Institute of Technolog, February.

[9] Foster, Lowell W. 1994. *Geo-Metrics III.* Reading, MA: Addison-Wesley.

[10] Franklin, Gene F., J. D. Powell, and A. Emami-Naeini. 1994. *Feedback control of dynamic systems.* 3rd ed. Reading, MA: Addison-Wesley.

[11] Gere, James M. and S. P. Timoshenko. 1984. *Mechanics of Materials.* 2nd ed. Boston, MA: PWS-Kent.

[12] Hayt, William H. Jr. and J. E. Kemmerly. 1993. *Engineering circuit analysis.* 5th ed. New York, NY: McGraw-Hill.

[13] Hess, D.P., and A. Soom. 1990. Friction at a Lubricated Line Contact Operating at Oscillating Sliding Velocities. *ASME Journal of Tribology* 112:147-152.

[14] Hogan, Neville. 1985. Impedance Control: An Approach to Manipulation: Part 1 - Theory, Part 2 - Implementation, Part 3 - Applications. *Journal of Dynamic Systems, Measurement, and Control* 107:1-23.

[15] Jacobsen, S. C., E. K. Iversen, D. F. Knutti, R. T. Johnson, and K. B. Biggers. 1986. Design of the Utah/M.I.T. Dextrous Hand. In *Proceedings of the 1986 IEEE international conference on robotics and automation*, 1520-1532. Washington, D.C.: IEEE Computer Society Press.

[16] Jugenheimer, Kristin A. 2001. *A robot for hand rehabilitation.* MS Thesis, Massachusetts Institute of Technology, February.

[17] Krebs, H. I., B. T. Volpe, M. L. Aisen, and N. Hogan. 2000. Increasing productivity and quality of care: Robot-aided neuro-rehabiltation. *Journal of Rehabiltation Research and Development* 37:639-652.

[18] National Stroke Association. 2002. *http://www.stroke.org.*

[19] Palastanga, Nigel, D. Field, and R. Soames. 1994. *Anatomy and human movement.* 2nd ed. Boston, MA: Butterworth-Heinemann.

[20] Rabinowicz, Ernest. 1992. Friction fluctuations. In *Fundamentals of friction: Macroscopic and microscopic processes*, ed. I. L. Singer and H. M. Pollock, 25-34. Norwell, MA: Kluwer Academic Publishers.

[21] Salisbury, J. K. Jr. 1984. Design and control of an articulated hand. In *International symposium on design and synthesis*, 459-466. Tokyo, Japan: The Japan Society of Precision Engineering.

[22] Shigley, Joseph E. and C. R. Mischke. 1989. *Mechanical Engineering Design.* 5th ed. New York, NY: McGraw-Hill.

[23] Slocum, Alexander H. 1992. *Precision machine design.* Dearborn, MI: Society of Manufacturing Engineers.

[24] Snow, Edward R. 1993. *The load/deflection behavior of pretensioned cable/pulley transmission mechanisms.* MSME Thesis, Massachusetts Institute of Technology. December.

[25] Townsend, William T. 1988. *The effect of transmission design on force-controlled manipulator performance.* PhD Thesis, Massachusetts Institute of Technology. April.

[26] United States Census Bureau. 2000. *http://www.census.gov/cgi-bin/ipc/-idbsum?cty=US.* May 10.

[27] Volpe, B. T., H. I. Krebs, N. Hogan, L. Edelstein, C. Diels, and M. Aisen. 2000. A novel approach to stroke rehabilitation: Robot-aided sensorimotor stimulation. *Neurology* 54:1938-1944.